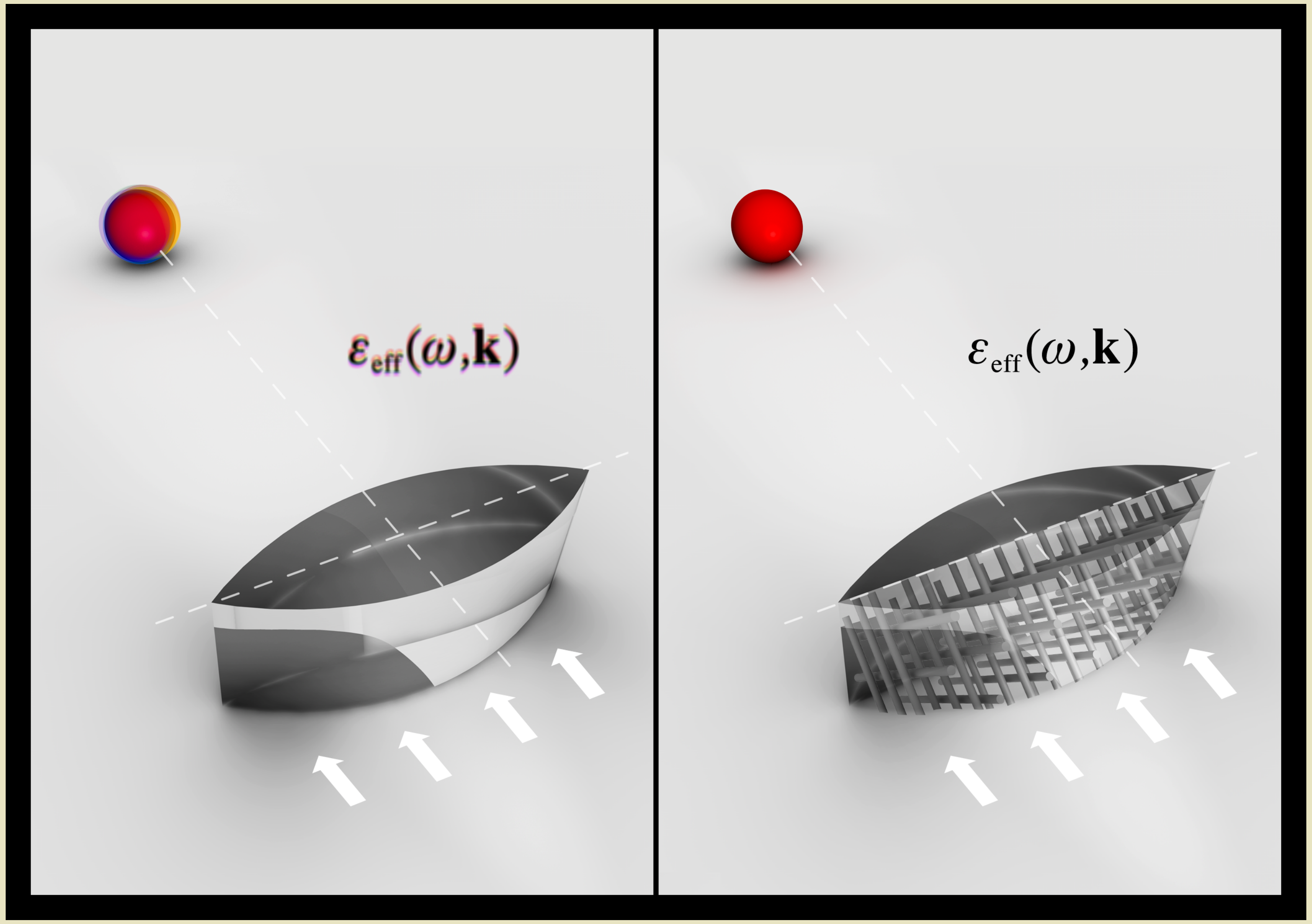

João Tiago de Figueiredo e Costa

Nonlocal Effective Medium Approach to Wave Propagation in Metamaterials

Dissertation to obtain the PhD Degree in Electrical and Computer Engineering, specialization in Telecommunications.
Supervisor: Professor Mário Gonçalo Mestre Veríssimo Silveirinha.

September 2012

· U C ·

UNIVERSIDADE DE COIMBRA

João Tiago de Figueiredo e Costa
Nonlocal Effective Medium Approach to Wave Propagation in Metamaterials
UNIVERSIDADE DE COIMBRA

To João Carlos Henriques dos Reis e Costa, my father.

“And we should consider every day lost on which we have not danced at least once.
And we should call every truth false which was not accompanied by at least one laugh.”
(Friedrich Nietzsche , 1844-1900)

Abstract

In the last couple of decades the scientific community has given a great attention to a striking class of modern artificial materials, the so-called metamaterials. This class of artificial materials is characterized by extraordinary and unusual electromagnetic properties, and it has naturally attracted researchers worldwide. It has been shown that these materials have exciting applications in the emerging fields of nanophotonics and plasmonics. The characterization of the electromagnetic behavior of metamaterials is therefore increasingly important.

This thesis is devoted to the study of numerical methods based on effective medium theory to characterize the electromagnetic response of nonlocal metamaterials.

A new numerical formalism is developed to extract the effective parameters of metamaterials formed by periodic arrangements of arbitrarily shaped dielectric/metallic inclusions embedded in dielectric/metallic hosts.

Some fundamental topics such as negative refraction, the Poynting vector and other energy relations are discussed and illustrated with numerical examples.

A novel metamaterial configuration that permits achieving a broadband DNG response as well as superlensing is proposed.

A new numerical formalism is proposed to solve the Maxwell's equations in scenarios wherein electromagnetic waves interact with arbitrary shaped spatially dispersive wire media bodies. Using this numerical formalism, some exciting applications are proposed for a class of wire media known as double wire medium. The possibility of enhancing the magnetic field at the tip of tapered double wire medium waveguide is discussed. Finally, rooted in the anomalous properties of the double wire medium, an exciting solution to suppress the chromatic aberrations inherent to single-material glass lenses is proposed.

Keywords

Metamaterials, Nonlocal Homogenization, FDFD, Broadband DNG Response, Superlensing, Poynting Vector, Heating Rate, Stored Energy, Wire Media, Spatial Dispersion , Waveguide Tapering, Chromatic Aberrations, Achromatic Lenses.

Resumo

No último par de décadas, a comunidade científica tem dado grande atenção a uma notável classe de materiais artificiais modernos, os chamados metamateriais. Esta classe de materiais artificiais é caraterizada por propriedades eletromagnéticas extraordinárias e pouco usuais, e tem naturalmente atraído investigadores em todo o mundo. Demonstrou-se que estes materiais têm aplicações interessantes em áreas emergentes como a nanofotónica e a plasmónica. A caraterização do comportamento electromagnético em metamateriais é, portanto, cada vez mais importante.

Esta tese é dedicada ao estudo de métodos numéricos baseados em teoria de meio efetivo para caraterizar a resposta eletromagnética de metamateriais não-locais.

Um novo formalismo numérico é desenvolvido para extrair os parâmetros efetivos de metamateriais formados por arranjos periódicos de inclusões dielétricas/metálicas com forma arbitrária, inseridas em meios dielétricos/metálicos.

Alguns tópicos fundamentais tais como índice de refração negativo, o vetor de Poynting e relações de energia, são discutidos e ilustrados com exemplos numéricos.

Uma nova configuração metamaterial é proposta para atingir uma resposta DNG de banda larga, bem como superlensing.

Um novo formalismo numérico é desenvolvido para resolver as equações de Maxwell em cenários em que as ondas eletromagnéticas interagem com formas arbitrárias de meios espacialmente dispersivos formados por arranjos de fios metálicos. Usando este formalismo numérico, são discutidas algumas aplicações interessantes para uma classe de fios conhecida como *double wire medium*. A possibilidade de concentrar o campo magnético na extremidade de um guia de ondas afunilado formado pelo *double wire* medium, é discutida. Finalmente, baseada nas propriedades anómalas do *double* *wire medium*, é proposta uma interessante solução para suprimir as aberrações cromáticas inerentes às lentes compostas por um único vidro.

Palavras Chave

Metamateriais, Homogeneização Não-local, FDFD, Resposta DNG Com Banda Larga, Superlensing, Vetor de Poynting, Taxa de Aquecimento, Energia Armazenada, Wire Media, Dispersão Espacial, Guia de Ondas Afunilado, Aberrações Cromáticas, Lentes Acromáticas.

Preface

This dissertation is the result of a work carried out under the supervision of Prof. Mário Silveirinha, at Instituto de Telecomunicações – Coimbra and Department of Electrical and Computer Engineering of the Faculty of Sciences and Technology of the University of Coimbra between October 2007 and March 2012. The originality of this thesis is sustained in a series of journal and conference papers that have been published while I was doing my PhD research. Except where explicit reference is made to the work of others, the work contained in this dissertation is my own.

Acknowledgements

Finishing this thesis is one of the most fulfilling moments I have ever experienced. It feels like finally reaching the end of a long road which I many times felt wouldn't have an end. But, and like everything in life, this accomplishment would be meaningless without having the people I care about by my side.

My first words go to Prof. Mário Silveirinha, my PhD supervisor. I am forever thankful for all his guidance, patience and for all the exciting scientific ideas he humbly shared with me. He is undoubtedly one of the most extraordinary human beings with whom I had the privilege and honor to share a period of my existence. Thank you.

I can't forget my mother, my greatest heroine. Thank you for fighting by my side this big war called life. For being my strength when I had none left. For all the love. For being a mother, a father, a sister and a friend. Thank you.

To my grandparents, Jorge, Nisete, Alice and Costa, thank you for the endless love. For making me feel I am the luckiest grandson in the world. For being proud of me no matter what.

To the best aunt ever and to her amazing husband and wonderful children, I am eternally grateful for all the joy and happiness they bring to my life.

I am also thankful to all my colleagues and friends at the Microwave Laboratory.

Morgado. A crazy mixture of tears and laughs invade me as I look back and remember every wonderful experience we have lived so far. The most pure and genuine friend I could ever have. If he started his PhD because of me, I was surely able to finish mine because of him. “Always friends”, my brother.

To João, for fixing my car every time I destroy it.

I also want to express my deepest gratitude to Dr. Stanislav Maslovski for all the wise thoughts connected both with science and life that he kindly shared with me. Thank you for teaching me so much.

I want to deeply express my gratitude to David, for having joined my shortlist of good friends and also for being so available whenever I have sought for his help.

I also want to thank to my marvelous friends Pedro, Guilherme, Ricardo and Bruno for staying nearby all this time.

To Tininha, my girlfriend, thank you for the endless love and patience. Thank you for giving me the greatest lesson ever: what to genuinely love someone is. I hope we will grow old together.

I would like to fully acknowledge the technical and financial support of *Instituto de Telecomunicações – Pólo de Coimbra* in the person of its coordinator Prof. Henrique Silva, as well as the financial support during these four years of research provided by *Fundação para a Ciência e Tecnologia* under the fellowship SFRH/BD/36976/2007.

My final words go to my father. He is the biggest reason behind this thesis. Now you can smile, for I have finished what life didn’t let you. This thesis is for you.

Contents

Symbol List

$\mathbf{a}_1, \mathbf{a}_2$	Primitive vectors
a	Lattice constant
A_{cell}	Unit cell area
$\mathbf{b}$	Microscopic induction field
β_p	Plasma wave number
$\mathbf{B}_{\text{av}}$	Macroscopic induction field
c	Speed of light in free-space
δ	Skin depth
δf	Chromatic aberration
Δi	Grid spacing in the x_i-direction
$\mathbf{e}$	Microscopic electric field
ε_0	Free-space permittivity
$\overline{\overline{\varepsilon}}_{\text{eff}}$	Effective permittivity dyadic
$\varepsilon_{\text{eff},ii}$	Effective permittivity in the x_i-direction
ε_h	Relative permittivity of the host
$\overline{\overline{\varepsilon}}_r$	Local permittivity dyadic
η	Wave impedance
$\mathbf{E}_{\text{av}}$	Macroscopic electric field
f	Frequency
f_v	Volume fraction
γ_0	Free-space propagation constant
Γ	Collision frequency
$\mathbf{h}$	Microscopic magnetic field
i	$\sqrt{-1}$
$\overline{\overline{\mathbf{I}}}$	Identity dyadic
$\mathbf{j}_d$	Induced microscopic current density
$\mathbf{j}_e$	External electric current density
J_l	Bessel function of 1st kind and order l

$\mathbf{k}$	Wave vector
k_0	Wave number in free-space
λ_0	Wavelength in free-space
λ_g	Guided wavelength
L_w	Wire effective inductance
L_i	Slab thickness in the x_i-direction
μ_0	Free-space permeability
$\overline{\overline{\mu}}_{\text{eff}}$	Effective permeability dyadic
$\overline{\overline{\mu}}_r$	Local permeability dyadic
n_{eff}	Effective index of refraction
ω	Angular frequency
ω_p	Plasma frequency
Ω	Unit cell
$\mathbf{P}_e$	External polarization vector
$\mathbf{P}_g$	Generalized polarization vector
q_{av}	Spatially averaged heating rate
$\mathbf{r}$	Position vector
r_w	Wire radius
R	Radius of cylinders/spheres/surfaces
ρ	Reflection coefficient
$\mathbf{s}$	Microscopic Poynting vector
$\mathbf{S}$	Spatially averaged Poynting vector
θ_i	Incident angle
θ_t	Transmission angle
τ	Transmission coefficient
$\hat{\mathbf{u}}_i$	Unit vector in the x_i-direction
v_g	Group velocity
W_{av}	Spatially averaged stored energy density
$\overline{\overline{\xi}}, \overline{\overline{\zeta}}$	Magneto-electric coupling tensors
Ψ	Optical path length
Z_w	Wire self-impedance

I. Introduction

I.1. Overview

This thesis is dedicated to the study of the interaction between electromagnetic waves and metamaterials using effective medium methods. In addition, based on the developed numerical methods some exciting applications for wire media metamaterials are proposed and discussed.

The history of modern metamaterials can be traced back to 1968, when Veselago suggested that a medium having electric permittivity ε and magnetic permeability μ simultaneously negative is characterized by left-handed propagation, rather than by right-handed propagation as in usual materials [1]. Nevertheless, the scientific boom related with metamaterials only appeared three decades later when in 2000, building on Veselago's work, Pendry showed that a lossless slab with negative refraction $n=-1$ makes a perfect lens that beats the diffraction limit [2].

Metamaterials typically consist of periodic arrangements of metallic/dielectric inclusions embedded in a given host medium. The key characteristic of this type of microstructured materials is that they are characterized by exotic electromagnetic responses which are usually radically different from those of its constituents.

Perhaps one of the most fascinating aspects of metamaterials is that they may permit an unparalleled control of wave propagation (e.g., “Transformation Optics” [4, 5]), which in turn may open new avenues to a broad range of potential applications. Naturally, in order to implement a given metamaterial-based device, first it is imperative to deeply understand how electromagnetic radiation interacts with this modern class of artificial media, and how a desired response can be realized in practice. This is where the homogenization procedure comes in. It provides efficient tools to describe the electromagnetic response of any given material and, in this specific case, in metamaterials. In fact, after properly homogenized, a metamaterial for instance formed by a periodic arrangement of dielectric/metallic inclusions in a dielectric host can be regarded as a continuous medium whose electromagnetic properties are accurately described by some effective parameters. This tremendously simplifies the prediction of the interaction between electromagnetic waves and metamaterials.

Nevertheless, not everything is a bed of roses, and homogenizing an arbitrary metamaterial msy be a tremendous challenge! In fact, in order to achieve the most interesting electromagnetic responses (e.g, artificial magnetism), metamaterials are typically composed by inclusions with characteristic sizes only one order of magnitude inferior to the wavelength of radiation λ. Such a property may impose some restrictions on the traditional homogenization methods mainly due to the emergence of spatially dispersive effects [3, 6-9]. Indeed, the most common homogenization techniques used to model the effective response of metamaterials are limited by the fact that they do not take into account the effect of spatial dispersion [10, 11], or simply by the fact that they are grounded in not entirely valid assumptions [12-15]. This work seeks to contribute to overcome these limitations.

Based on a previously developed theory [16], a spatially dispersive numerical formalism that accurately characterizes the electromagnetic response of periodic metamaterials is proposed. The developed method is applied to determine the electromagnetic behavior of a metamaterial configuration formed by arrays of dielectric particles embedded in a plasmonic host. It is shown that such metamaterial may be an interesting option to achieve a broadband left-handed regime as well as superlensing. In addition, the physical connection between the macroscopic and microscopic Poynting vector, stored energy and heating rate in metamaterials is clarified.

Special attention is given to an important class of strongly spatially dispersive metamaterials known as "double wire medium". A novel efficient formalism is developed here to properly model the spatially dispersive nature of this metamaterial structure. Based on this numerical formalism, some exciting applications are proposed for the double wire medium, such as subwavelength field concentration or suppression of chromatic aberrations.

Throughout this work the time dependence $e^{-i\omega t}$ is assumed.

I.2. Organization of the Thesis

The thesis is organized in 6 chapters, being the first one this introductory chapter.

In Chapter II, some homogenization techniques commonly used to characterize the electromagnetic response of metamaterials are reviewed, and their respective limitations are briefly described. In Sec. II.2.2, a completely general finite differences frequency domain (FDFD) method based on a previously developed nonlocal homogenization theory [16] is derived to extract the effective parameters of microstructured materials. The proposed numerical formalism permits computing a nonlocal dielectric function $\overline{\overline{\varepsilon_{\text{eff}}}}(\omega,\mathbf{k})$ that takes into account the hypothetical spatially dispersive nature of a metamaterial. In Sec. II.3.1, the effective parameters are extracted for several metamaterial configurations formed by periodic arrangements of dielectric/plasmonic cylinders embedded in plasmonic/dielectric hosts. The local parameters such as the relative permittivity ε_r or magnetic permeability μ_r are calculated for these metamaterials, from the computed nonlocal dielectric function. In Sec. II.3.2, the effective response of a metamaterial composed by horseshoe shaped inclusions [17] is analyzed. Due to the asymmetric geometry of the inclusions, the bianisotropic effects play a relevant role in the electromagnetic characterization of the material, and therefore they are also computed. Most of the results obtained in this chapter with the FDFD formalism are compared with other homogenization techniques [10, 18].

In Chapter III, relying on the fact that the effective permittivity ε_{eff} and effective permeability μ_{eff} of a zero-index metamaterial (Sec. II.3.1.3) may be simultaneously negative in a certain frequency window, several topics are investigated. First, supported by the theory reported in [19], the macroscopic Poynting vector, stored energy and heating rate are computed (Sec. III.2.) using the FDFD homogenization formalism derived in Chapter II, and the respective connection with their microscopic counterparts is highlighted. Each of these three quantities is calculated from microscopic and macroscopic models.

Still in the third chapter, the possibility of using the zero-index metamaterial to achieve a broadband regime where both ε_{eff} and μ_{eff} are simultaneously negative and well-matched to free-space is analyzed. Additionally, the possibility of using such a material to mimic the Veselago-Pendry's superlens is also discussed. The results obtained with the FDFD formalism are compared against those predicted by elementary mixing formulas [18] and full-wave simulations [20].

Chapter IV is dedicated to the topic of spatial dispersion in wire media [7, 9]. In Sec. IV.2, a straightforward approach based on the inverse Fourier transform of the constitutive relation $\mathbf{D} = \overline{\overline{\varepsilon}}(\omega, \mathbf{k}) \cdot \mathbf{E}$ is discussed. Based on this solution, two FDFD implementations are proposed to model the spatially dispersive response of complex shaped bodies of microstructured materials formed by arrays of nonconnected crossed metallic wires. In Sec. IV.3, a different spatially dispersive FDFD solution rooted in a quasi-static homogenization model [21] that takes into account the microstructure of the metamaterial is proposed. It is proven that the way how the electric field **E** and electric displacement **D** are linked at the boundary of the metamaterial and a dielectric/metallic region is of crucial importance. This is illustrated in Sec. IV.4, where some scattering problems are solved using the three studied implementations. The obtained results are compared with analytical data based on mode matching and also with a full-wave simulator [20].

In the fifth chapter, some novel applications for the double wire medium are put forward. In Sec. V.3, the possibility of concentrating the electromagnetic field in a narrow spot by tapering a metamaterial waveguide is discussed. In Sec. V.4, a novel and exciting solution to minimize the effects of chromatic aberrations inherent to single-material glass lenses is proposed.

In Chapter VI, the main conclusions of this work are outlined, as well as some future work.

I.3. Main Contributions

The key contributions of this thesis are:

- Development of an efficient, straightforward and accurate FDFD numerical formalism to extract the effective parameters of nonlocal metamaterials.
- Clarification of fundamental physical concepts (e.g., negative refraction, Poynting vector) in the context of negative-index metamaterials and effective medium theory.
- Proposal of a novel metamaterial to achieve a broadband matched DNG response and superlensing based on high-index materials embedded in a plasmonic host.

- Development of a novel FDFD-SD numerical formalism based on a quasi-static model to properly model the spatially dispersive nature of complex shaped wire media topologies.
- Analytical study and numerical demonstration of electromagnetic field concentration using a tapered waveguide formed by a spatially dispersive nanowire-based material.
- Proposal of a novel and exciting solution to suppress the chromatic aberrations inherent to single-material glass lenses.

In the body of this thesis each of the above topics is expanded and the new contributions are compared with the open literature.

I.4. List of Author Publications

I.4.1. Articles in Journal

[J.1] **J. T. Costa** and M. G. Silveirinha, “Macroscopic electromagnetic response of arbitrarily shaped spatially dispersive bodies formed by metallic wires,” *Phys. Rev. B*, **86**, 075129, 2012.

[J.2] **J. T. Costa** and M. G. Silveirinha, “Achromatic lens based on a nanowire material with anomalous dispersion”, *Opt. Express* **20**, 13915, 2012.

[J.3] **J. T. Costa** and M. G. Silveirinha, “Mimicking the Veselago-Pendry’s lens with broadband and matched double negative metamaterials,” *Phys. Rev. B* **84**, 155131, 2011.

[J.4] **J. T. Costa**, M. G. Silveirinha, and Andrea Alù, “Poynting vector in negative-index metamaterials,” *Phys. Rev. B* **83**, 165120, 2011.

[J.5] **J. T. Costa**, M. G. Silveirinha, and S. I. Maslovski, “Finite-difference frequency-domain method for the extraction of effective parameters of metamaterials,” *Phys. Rev. B* **80**, 235124, 2009.

I.4.2. Articles in Conference Proceedings

[C.1] **J. T. Costa** and M. G. Silveirinha, “Suppression of the chromatic aberrations using a nanowire metamaterial,” in *Proc. Metamorphose International Congress on Advanced Electromagnetic Materials in Microwaves and Optics – Metamaterials 2012*, St. Petersburg, Russia, September 2012 [**this paper was awarded with the second place in the student paper competition**].

[C.2] **J. T. Costa** and M. G. Silveirinha, “Suppression of chromatic aberrations based on a metamaterial with anomalous dispersion,” in *Proc. IEEE AP-S/URSI International Symposium on Antennas and Propagation*, Chicago, United States, July, 2012.

[C.3] **J. T. Costa** and M. G. Silveirinha, “Numerical modeling of the electromagnetic response of complex shaped spatially dispersive bodies,” in *Proc. IEEE AP-S/URSI International Symposium on Antennas and Propagation*, Chicago, United States, July, 2012.

[C.4] **J. T. Costa** and M. G. Silveirinha, “Broadband DNG response based on high-index materials embedded in a plasmonic host,” in *Proc. Metamorphose International Congress on Advanced Electromagnetic Materials in Microwaves and Optics – Metamaterials 2011*, Barcelona, Spain, October, 2011.

[C.5] **J. T. Costa** and M. G. Silveirinha, “Efficient characterization of the effective response of complex shaped double wire medium structures,” in *Proc.Young Scientist Meeting on Metamaterials*, Valencia, Spain, February, 2011.

[C.6] **J. T. Costa** and M. G. Silveirinha, "Numerical study of the definition of the Poynting vector in metamaterials," in *Proc. Metamorphose International Congress on Advanced Electromagnetic Materials in Microwaves and Optics – Metamaterials 2010*, Karlsruhe, Germany, September, 2010.

[C.7] M. G. Silveirinha and **J. T. Costa**, "Poynting vector, heating rate, and stored energy in structured materials: a first principles derivation", in *Proc. IEEE AP-S/URSI International Symposium on Antennas and Propagation*, Toronto, Canada, July 2010 (invited talk).

[C.8] **J. T. Costa** and M. G. Silveirinha, "Nonlocal homogenization using a finite-difference-frequency-domain numerical code," in *Proc. Metamorphose International Congress on Advanced Electromagnetic Materials in Microwaves and Optics – Metamaterials 2009*, London, United Kingdom, September, 2009.

[C.9] **J. T. Costa** and M. G. Silveirinha, "Computation of the effective parameters of metamaterials using a finite-difference frequency-domain method," *in Proc. Conf. on Telecommunications- ConfTele, Santa Maria da Feira*, Portugal, May 2009.

References

[1] V. G. Veselago, "The electrodynamics of substances with simultaneously negative values of ε and μ," *Sov. Phys. Usp*. **10**, 509, 1968.

[2] J. B. Pendry, "Negative refraction makes a perfect lens," *Phys. Rev. Lett.* **85**, 3966, 2000.

[3] V. Agranovich and V. Ginzburg, *Spatial Dispersion in Crystal Optics and the Theory of Excitons*, Willey-Interscience, New York, 1966.

[4] R. Liu, C. Ji, J. J. Mock, J. Y. Chin, T. J. Cui, and D. R. Smith, "Broadband ground-plane cloak," *Science* **323**, 366, 2009.

[5] H. Chen, C. T. Chan, and Ping Sheng, “Transformation optics and metamaterials,” *Nature Materials* **9**, 387, 2010.

[6] M. G. Silveirinha, C. A. Fernandes, and J. R. Costa, “Additional boundary condition for a wire medium connected to a metallic surface,” *New J. Phys.* **10**, 053011, 2008.

[7] P. A. Belov, R. Marqués, S. I. Maslovski, I. S. Nefedov, M. G. Silveirinha, C. R. Simovski, and S. A. Tretyakov, “Strong spatial dispersion in wire media in the very large wavelength limit,” *Phys. Rev. B* **67**, 113103, 2003.

[8] G. Shvets, A. K. Sarychev, and V. M. Shalaev,” Electromagnetic properties of three-dimensional wire arrays: photons, plasmons, and equivalent circuits,” *Proc. SPIE* **5218**, 156, 2003.

[9] C. R. Simovski and P. A. Belov, “Low-frequency spatial dispersion in wire media,” *Phys. Rev. E* **70**, 046616, 2004.

[10] D. R. Smith and S. Schultz, “Determination of effective permittivity and permeability of metamaterials from reflection and transmission coefficients,” *Phys. Rev. B* **65**, 195104, 2002.

[11] X. Chen, T. M. Grzegorczyk, Bae-Ian Wu, J. Pacheco, Jr., and J. A. Kong, “Robust method to retrieve the constitutive effective parameters of metamaterials,” *Phys. Rev. E* **70**, 016608, 2004.

[12] Y. Zhao, P. A. Belov, and Y. Hao, “Spatially dispersive finite-difference time-domain analysis of sub-wavelength imaging by the wire medium slabs,” *Opt. Express* **14**, 5154, 2006.

[13] Y. Zhao, P. A. Belov, and Y. Hao, “Modelling of wave propagation in wire media using spatially dispersive finite-difference time-domain method: numerical aspects,” *IEEE Trans. Antennas and Propag.* **55**, 1506, 2007.

[14] Y. Zhao, P. A. Belov, and Y. Hao, “Subwavelength internal imaging by means of a wire medium,” *J. Opt. A: Pure Appl. Opt.* **11** 075101, 2009.

[15] S. Raza, G. Toscano, Antti-Pekka Jauho, M. Wubs, and N. A. Mortensen, “Unusual resonances in nanoplasmonic structures due to nonlocal response,” *Phys. Rev. B* **84***,* 121412(R), 2011.

[16] M. G. Silveirinha, “Metamaterial homogenization approach with application to the characterization of microstructured composites with negative parameters,” *Phys. Rev. B* **75**, 115104, 2007.

[17] A. K. Sarychev, G. Shvets, and V. M. Shalaev, “Magnetic plasmon resonance,” *Phys. Rev. E* **73**, 036609, 2006.

[18] J. D. Jackson, *Classical Electrodynamics*, Sect. 6.6, Wiley, 1998.

[19] M. G. Silveirinha, “Poynting vector, heating rate, and stored energy in structured materials: A first-principles derivation,” *Phys. Rev. B* **80**, 235120, 2009.

[20] CST Microwave Studio Suite^{TM} 2010, (http://www.cst.com).

[21] S. I. Maslovski and M. G. Silveirinha, “Nonlocal permittivity from a quasistatic model for a class of wire media” *Phys. Rev. B* **80**, 245101, 2009.

II. Homogenization of Metamaterials

II.1. Introduction

Homogenization methods have been used over several decades to describe the interaction of electromagnetic waves with heterogeneous mater [1]. The key idea of homogenizing a material composed by different constituents is to regard it as a continuous medium whose electromagnetic response may be correctly described by only a few effective parameters, typically the effective permeability $\overline{\overline{\varepsilon_{\mathrm{eff}}}}$ and the effective permittivity $\overline{\overline{\mu_{\mathrm{eff}}}}$. By using such effective parameters it is avoided taking into account all the minute microscopic details of the material, which in turn tremendously simplifies solving radiation and propagation problems. Moreover, effective medium techniques significantly reduce the computational effort required to model the electromagnetic response of a given heterogeneous structure as well. Traditional homogenization techniques were originally derived to characterize the electromagnetic behavior in conventional media, whose dimensions of the inclusions are several orders of magnitude smaller than that of the wavelength of radiation.

As discussed in Chapter I, in contrast with conventional media, metamaterials are generally characterized by spatial dispersion, which is not taken into account by the traditional homogenization techniques.

In this chapter, the state of the art of homogenization methods for metamaterials and their respective limitations are reviewed. Furthermore, based on a spatially dispersive and completely general homogenization formalism derived in Ref. [2], a finite differences frequency domain (FDFD) formalism that enables an efficient and accurate extraction of the effective parameters of metamaterials is proposed.

II.2. The Homogenization Problem

II.2.1. Limitations of Traditional Homogenization Techniques

The pioneering contributions to the development of homogenization procedures for conventional media came from Plank, Lorentz, Planck, and Oseen [1]. Plank was in fact the first to introduce the concept of macroscopic electromagnetism i.e., the possibility of using averaged quantities of the microscopic fields in order to provide a useful and accurate mean for the characterization of the effective medium parameters of arbitrary materials. The theory of averaging procedures was further developed in the last century [3, 4] and, more recently, the concept of macroscopic electromagnetism was extended to the characterization of the effective response of metamaterials [5, 6].

Homogenization procedures based on the use of mixing formulas, e.g. the classic Clausius-Mossotti (CM) formula [7], are perhaps the simplest ones. Nevertheless, even though the CM formula may yield very accurate results in some very specific scenarios, it is limited by the fact that it relies on the assumption that the volume fraction of the inclusions is relatively small, which is rarely the case of metamaterials.

Metamaterials are mostly formed by periodic arrangements of dielectric or metallic particles, hence valuable information about their effective response may also be retrieved from their band structure, but the applicability of this procedure is obviously limited in cases of electromagnetic band gaps or in case of losses [6].

The effective parameters of metamaterials may also be retrieved from the inversion of computed or measured scattering data [8, 9]. In fact, this procedure is unquestionably the most popular retrieval method to characterize composite media nowadays. However, this method suffers from some drawbacks, namely it may fail in scenarios wherein the bianisotropic and spatially dispersive effects are not neglectable [J.5]. This inversion method may as well yield multiple solutions, making it cumbersome to determine the correct branch, and in some cases the extracted parameters may be unphysical [10, 11]. Other homogenization approaches have been proposed over the years [12-14], but their application is ultimately limited to very specific geometries, or to the quasi-static limit, or restricted by some other factor.

II.2.2. Nonlocal Homogenization model

A systematic and completely general homogenization method to extract the effective parameters of metamaterials was introduced in 2007 [2, 15]. This method is based on the solution of a source-driven numerical problem, and therefore it does not involve the computation of the eigenmodes. The homogenization procedure proposed in Ref. [2] describes the metamaterial in terms of a nonlocal dielectric function rather than in terms of the bianisotropic constitutive relations, which are commonly used in several works regarding homogenization techniques. This nonlocal homogenization method assumes particular importance in the characterization of metamaterials with strong spatial dispersion which, as already mentioned, cannot be homogenized with classical methods.

The dielectric function reported in [2] is defined as nonlocal since it takes into account the spatially dispersive effects inherent to most metamaterials. A spatially dispersive material is characterized by the fact that the polarization acquired by the inclusions does not depend exclusively on the macroscopic (averaged) field in the immediate vicinity of the particle but depends also on the macroscopic electric field at distances larger than the characteristic dimension of the basic cell. As a consequence of spatial dispersion, the electric displacement vector $\mathbf{D}$ and the electric field $\mathbf{E}$ are related through a spatial convolution in the space domain, and thus in the spectral domain (plane waves) the dielectric function becomes a function of both the frequency of operation ω and of the wave vector $\mathbf{k}$. In fact, it has been recently shown that such materials may have quite interesting applications such as the transport and manipulation of the electromagnetic fields in the nanoscale [16, 17], anomalous dispersion of light colors [18], subwavelength waveguiding [19, 20], suppressing the chromatic aberrations inherent to single glass lenses [J.2], amongst others. Therefore, it would be highly desirable to have nonlocal homogenization methods which properly characterize metamaterials with strong spatial dispersion.

An interesting property of the homogenization approach of Ref. [2] is that the constitutive relations implicit in the spatially dispersive model are very general. Namely, they can model arbitrary composit media, such that the electric displacement vector is related to the macroscopic electric field through a spatial convolution, and thus include as a particular case the conventional constitutive relations that characterize the material using effective permittivity and permeability tensors, and possibly bianisotropic parameters (magneto-electric tensors). In particular, it was shown in Ref. [2] that the conventional local parameters, if meaningful, may be extracted by differentiating the nonlocal dielectric function with respect to the wave vector.

II.2.2.1 Overview of the Homogenization Formalism

Here, an overview of the nonlocal homogenization framework is presented, explaining its principles and how it can be used to extract the effective parameters (e.g., $\overline{\overline{\varepsilon}}_{\text{eff}}$ and $\overline{\overline{\mu}}_{\text{eff}}$) of metamaterials.

For simplicity, without loss of generality, it is assumed that the structured material under study is a two-dimensional (2D) metal-dielectric crystal, obtained by translating a two dimensional unit cell along the primitive vectors $\mathbf{a}_1$ and $\mathbf{a}_2$ (Fig. 2.1). The periodic material can have dielectric and/or metallic inclusions with the magnetic permeability equal to μ_0 and relative permittivity $\varepsilon_{\mathrm{r}}(\mathbf{r},\omega)$.

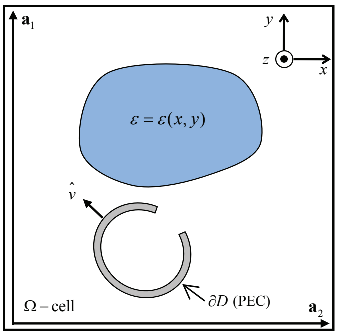

Fig. 2.1. Geometry of a two dimensional unit cell of a generic metallic-dielectric periodic material with a dielectric inclusion and a PEC inclusion.

The aim of the method introduced in Ref. [2] is to calculate the nonlocal dielectric function $\overline{\overline{\varepsilon_{\mathrm{eff}}}} = \overline{\overline{\varepsilon_{\mathrm{eff}}}}(\omega,\mathbf{k})$ of the metamaterial, where ω is the angular frequency and $\mathbf{k} = (k_x, k_y, k_z)$ is the wave vector. The possible dependence of the dielectric function $\overline{\overline{\varepsilon_{\mathrm{eff}}}}(\omega,\mathbf{k})$ on the wave vector results from spatial dispersion effects [21], which are characteristic of several metamaterials, even for very low frequencies [18, 19, 22, 23]. In order to compute the unknown dielectric function for a given $(\omega,\mathbf{k})$, the composite material is excited with a Floquet-periodic external distribution of electric current $\mathbf{j}_e$ of the form $\mathbf{j}_e = \mathbf{j}_{e,\mathrm{av}} e^{i\mathbf{k}.\mathbf{r}}$, where $\mathbf{j}_{e,\mathrm{av}}$ is a constant vector. Consequently, the induced "microscopic" electric and induction fields $\mathbf{e}$ and $\mathbf{b}$, respectively, have also the Floquet property, and satisfy the microscopic Maxwell's equations:

$$\nabla \times \mathbf{e} = i\omega\mathbf{b} \tag{2.1a}$$

$$\nabla \times \frac{\mathbf{b}}{\mu_0} = \mathbf{j}_e + \mathbf{j}_d - i\varepsilon_0\omega\mathbf{e}, \tag{2.1b}$$

where $\mathbf{j}_d = -i\omega\varepsilon_0(\varepsilon_{\mathrm{r}} - 1)\mathbf{e}$ is the induced microscopic current relative to the host medium and ε_{r} is the periodic permittivity of the material.

The macroscopic average fields $\mathbf{E}_{\text{av}}$ and $\mathbf{B}_{\text{av}}$ for a 2D metamaterial are defined as follows:

$$\mathbf{E}_{\text{av}} = \frac{1}{A_{\text{cell}}} \int_{\Omega} \mathbf{e}(\mathbf{r}) e^{-i\mathbf{k}\cdot\mathbf{r}} d^2\mathbf{r}, \qquad \mathbf{B}_{\text{av}} = \frac{1}{A_{\text{cell}}} \int_{\Omega} \mathbf{b}(\mathbf{r}) e^{-i\mathbf{k}\cdot\mathbf{r}} d^2\mathbf{r}. \tag{2.2}$$

In the above, Ω is the unit cell of the material and $A_{\text{cell}} = |\mathbf{a}_1 \times \mathbf{a}_2|$ is the area of Ω (Fig. 2.1). It can be easily verified that the macroscopic fields verify the following equations:

$$-\mathbf{k} \times \mathbf{E}_{\text{av}} + \omega \mathbf{B}_{\text{av}} = 0 \tag{2.3a}$$

$$\omega \mathbf{D}_{g,\text{av}} + \mathbf{k} \times \frac{\mathbf{B}_{\text{av}}}{\mu_0} = -\omega \mathbf{P}_e, \tag{2.3b}$$

where $\mathbf{P}_e = \frac{1}{i\omega A_{\text{cell}}} \int_{\Omega} \mathbf{j}_e(\mathbf{r}) e^{-i\mathbf{k}.\mathbf{r}} d^2\mathbf{r}$ is by definition the applied polarization vector. Moreover the generalized electric displacement $\mathbf{D}_{g,\text{av}}$ verifies the constitutive relation,

$$\mathbf{D}_{g,\text{av}} \equiv \varepsilon_0 \mathbf{E}_{\text{av}} + \mathbf{P}_g = \overline{\overline{\varepsilon_{\text{eff}}}}(\omega, \mathbf{k}) \cdot \mathbf{E}_{\text{av}}, \tag{2.4}$$

where

$$\mathbf{P}_g = \frac{1}{i\omega A_{\text{cell}}} \int_{\Omega} \mathbf{j}_d(\mathbf{r}) e^{-i\mathbf{k}\cdot\mathbf{r}} d^2\mathbf{r} \tag{2.5}$$

is the so-called generalized polarization vector, which can be related to the classical polarization and magnetization vectors, $\mathbf{P}$ and $\mathbf{M}$, respectively, and with higher-order multipoles [2]:

$$\mathbf{P}_g = \mathbf{P} - \mathbf{M}/i\omega + \ldots \quad . \tag{2.6}$$

The omitted terms in Eq. (2.6) involve spatial derivatives of the quadrupole density and other higher-order multipole moments. It should be clear that Eq. (2.4) permits determining the dielectric function for a given $(\omega, \mathbf{k})$ provided $\mathbf{P}_g$ is known for three independent vectors $\mathbf{E}_{\text{av}}$ (e.g., for $\mathbf{E}_{\text{av}} \sim \hat{\mathbf{u}}_i$, where $\hat{\mathbf{u}}_i$ is directed along the coordinate axes). Hence, the unknown dielectric function can be computed using the algorithm described next: (i) For a fixed ω and $\mathbf{k}$, determine the microscopic fields. To this purpose, select three independent vector amplitudes $\mathbf{j}_{e,\mathrm{av}}$ for the applied current $\mathbf{j}_e$ and then solve the microscopic Maxwell's Equations [Eq. (2.1)] for each distribution of current (it is assumed that the obtained average fields $\mathbf{E}_{\mathrm{av}}$ form an independent set of vectors). (ii) determine the generalized polarization vector $\mathbf{P}_g$ associated with each distribution of microscopic fields using Eq. (2.5). (iii) Calculate the dielectric function of the material $\overline{\overline{\varepsilon_{\mathrm{eff}}}} = \overline{\overline{\varepsilon_{\mathrm{eff}}}}(\omega,\mathbf{k})$ so that it is consistent with Eq. (2.4). The calculated dielectric function is independent of the excitation, i.e. it is independent of the specific set of constant vectors $\mathbf{j}_{e,\mathrm{av}}$ that is considered in the calculation.

II.2.2.2 Extraction of Local Parameters

An important property derived in Ref. [2] (see also Refs. [24, 25]) is that in the presence of weak spatial dispersion, so that the composite material can be described using conventional constitutive relations and its response is to some degree of approximation local, the effective parameters of the artificial medium (local permittivity, local permeability and magneto-electric parameters) can be readily extracted from the nonlocal dielectric function. Specifically, the relation between the nonlocal dielectric function and the local parameters is as follows:

$$\frac{\overline{\overline{\varepsilon_{\mathrm{eff}}}}}{\varepsilon_0}\left(\omega,\mathbf{k}\right) = \overline{\overline{\varepsilon}}_{\mathrm{r}} - \overline{\overline{\xi}}\cdot\overline{\overline{\mu}}_{\mathrm{r}}^{-1}\cdot\overline{\overline{\zeta}} + \frac{c}{\omega}\left(\overline{\overline{\xi}}\cdot\overline{\overline{\mu}}_{\mathrm{r}}^{-1}\times\mathbf{k} - \mathbf{k}\times\overline{\overline{\mu}}_{\mathrm{r}}^{-1}\cdot\overline{\overline{\zeta}}\right) + \frac{c^2}{\omega^2}\mathbf{k}\times\left(\overline{\overline{\mu}}_{\mathrm{r}}^{-1} - \overline{\overline{\mathbf{I}}}\right)\times\mathbf{k}, \qquad (2.7)$$

where $\overline{\overline{\mathbf{I}}}$ is the identity dyadic, $\overline{\overline{\varepsilon}}_r(\omega)$ and $\overline{\overline{\mu}}_r(\omega)$ are the relative *local* permittivity and permeability dyadics, respectively, and $\overline{\overline{\xi}}\left(\omega\right)$ and $\overline{\overline{\zeta}}\left(\omega\right)$ are dimensionless tensors that characterize the magneto-electric coupling [2]. The constitutive relations implicit in the definition of the local parameters are [2]:

$$\mathbf{D} = \varepsilon_0 \overline{\overline{\varepsilon}}_{\mathrm{r}}.\mathbf{E}_{\mathrm{av}} + \sqrt{\varepsilon_0 \mu_0}\, \overline{\overline{\xi}}.\mathbf{H} \tag{2.8a}$$

$$\mathbf{B}_{\mathrm{av}} = \sqrt{\varepsilon_0 \mu_0}\, \overline{\overline{\zeta}}.\mathbf{E}_{\mathrm{av}} + \mu_0 \overline{\overline{\mu}}_{\mathrm{r}}.\mathbf{H}. \tag{2.8b}$$

It is important to emphasize that the above constitutive relations are different from the constitutive relation implicit in Eq. (2.4). The constitutive relations (2.8) are local, i.e., their components are independent of the wave vector, which is an advantage since it drastically reduces the number of parameters that characterize the material. Moreover, the constitutive relations (2.8) are valid both in the spectral and in the spatial domains, which considerably simplifies the analysis of problems involving interfaces between different local media. The constitutive relations (2.8) have been used for a long time in the characterization of media with optical activity [25, 26].

As mentioned in Sec. II.2.2.1, it is assumed that the geometry of the metamaterial is intrinsically two-dimensional (the axis of the structure is along z (Fig. 2.1)) and that $k_z = 0$. Furthermore, it is also supposed that the electromagnetic wave is transverse electric to z (TE$^{\mathrm{z}}$). In such a scenario, it may be assumed that $\overline{\overline{\mu}}_{\mathrm{r}}(\omega) = \mu_{\mathrm{r},zz}\hat{\mathbf{u}}_z\hat{\mathbf{u}}_z$, and the relative magnetic permeability of the medium $\mu_{r,zz}$ can be numerically calculated as follows [2]:

$$\frac{\mu_{\mathrm{eff}}}{\mu_0} \equiv \mu_{\mathrm{r},zz}(\omega) = \frac{1}{1 - \left(\dfrac{\omega}{c}\right)^2 \dfrac{1}{2\varepsilon_0} \left.\dfrac{\partial^2 \varepsilon_{\mathrm{eff},yy}}{\partial k_x^2}\right|_{\mathbf{k}=0}}, \tag{2.9}$$

where $\varepsilon_{\mathrm{eff},yy} = \hat{\mathbf{u}}_y \cdot \overline{\overline{\varepsilon}}_{\mathrm{eff}}(\omega, \mathbf{k}=0) \cdot \hat{\mathbf{u}}_y$ (the homogenization method is summarized in Fig. (2.2)).

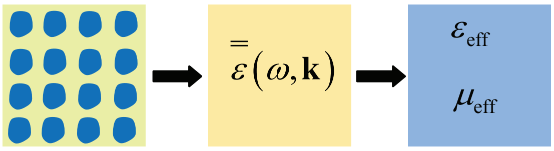

Fig. 2.2. Extraction of the effective-medium parameters of a composite material based on the theory of Ref. [2].

It is clear from Eq. (2.9) that the emergence of artificial magnetism is intrinsically related to spatial dispersion effects of second order [2, 24]. On the other hand, putting $\mathbf{k}=0$ in Eq. (2.7) it is readily found that:

$$\frac{\overline{\overline{\varepsilon_{\text{eff}}}}}{\varepsilon_0}(\omega,\mathbf{k}=0)=\overline{\overline{\varepsilon}}_{\text{r}}-\overline{\overline{\xi}}\cdot\overline{\overline{\mu}}_{\text{r}}^{-1}\cdot\overline{\overline{\zeta}}\,. \qquad (2.10)$$

If a given material has inversion symmetry, i.e., it is invariant under the transformation $\mathbf{r}\to-\mathbf{r}$ with respect to some suitable origin of the coordinates, the magneto-electric coupling is inexistent ($\overline{\overline{\xi}}=\overline{\overline{\zeta}}=0$). In such a case, the local electric permittivity is given by $\overline{\overline{\varepsilon}}_r(\omega)=\overline{\overline{\varepsilon_{\text{eff}}}}(\omega,\mathbf{k}=0)$. However, generally the tensors $\overline{\overline{\xi}}$ and $\overline{\overline{\zeta}}$ do not vanish and must be taken into account to properly describe the electromagnetic response of the material. It may be easily shown that the meaningful components of the tensor $\overline{\overline{\zeta}}$ for the 2D geometry under analysis (TE^{z} –polarized waves with $k_z=0$) are ζ_{zx} and ζ_{zy}. Thus, it may be assumed that

$$\overline{\overline{\zeta}}=\zeta_{zx}\hat{\mathbf{u}}_z\hat{\mathbf{u}}_x+\zeta_{zy}\hat{\mathbf{u}}_z\hat{\mathbf{u}}_y\,, \qquad (2.11)$$

where $\hat{\mathbf{u}}_z\hat{\mathbf{u}}_x\equiv\hat{\mathbf{u}}_z\otimes\hat{\mathbf{u}}_x$ represents the tensor product of two vectors. Taking into account that in reciprocal media the tensor $\overline{\overline{\xi}}$ is linked to $\overline{\overline{\zeta}}$ by the relation $\overline{\overline{\xi}}=-\overline{\overline{\zeta}}^{T}$ [26] (the superscript “*T*” represents the transpose tensor), and substituting Eq. (2.11) into Eq. (2.7) it is readily found that

$$\zeta_{zx}=-\frac{\omega}{c}\mu_{\text{r},zz}\frac{1}{\varepsilon_0}\frac{\partial\varepsilon_{\text{eff},xy}}{\partial k_x}\bigg|_{\mathbf{k}=0}\,,\qquad \zeta_{zy}=-\frac{\omega}{c}\mu_{\text{r},zz}\frac{1}{\varepsilon_0}\frac{\partial\varepsilon_{\text{eff},xy}}{\partial k_y}\bigg|_{\mathbf{k}=0}\,. \qquad (2.12)$$

It is clear from the above equation that the magneto-electric parameters are obtained from the first order derivatives of the nonlocal dielectric function with respect to the wave vector.

It is important to stress that the extraction of the local material parameters ($\overline{\overline{\varepsilon_{\mathrm{eff}}}} / \varepsilon_0\left(\omega,\mathbf{k}=0\right)$, μ_{eff}, ζ_{zx} and ζ_{zy}) is obviously based on the assumption that the response of the material is to some degree of extent local. This is equivalent to say that the effective medium can be accurately described by the bianisotropic constitutive relations [Eq. (2.8)]. In these conditions, if follows from Eq. (2.7) that the nonlocal dielectric function is necessarily a quadratic form of the wave vector. In particular, it should be clear that the magnetic permeability μ_{eff} [Eq. (2.9)] should completely determine the spatial dispersion effects of second order, or equivalently it should univocally determine the second order derivates of the nonlocal dielectric function $\overline{\overline{\varepsilon_{\mathrm{eff}}}}$ with respect to $\mathbf{k}$. It may be straightforwardly verified from Eq. (2.7) (by calculating the derivatives $\partial^2/\partial k_x^2$ and $\partial^2/\partial k_x \partial k_y$ at the origin) that μ_{eff} should verify, besides Eq. (2.9), the following formulas:

$$\frac{\mu_{\mathrm{eff}}^{(2)}}{\mu_0} = \frac{1}{1-\left(\dfrac{\omega}{c}\right)^2 \dfrac{1}{2\varepsilon_0} \left.\dfrac{\partial^2 \varepsilon_{\mathrm{eff},xx}}{\partial k_y^2}\right|_{\mathbf{k}=0}} \tag{2.13a}$$

$$\frac{\mu_{\mathrm{eff}}^{(3)}}{\mu_0} = \frac{1}{1+\left(\dfrac{\omega}{c}\right)^2 \dfrac{1}{\varepsilon_0} \left.\dfrac{\partial^2 \varepsilon_{\mathrm{eff},xy}}{\partial k_x \partial k_y}\right|_{\mathbf{k}=0}} \tag{2.13b}$$

The above formulas should be regarded as consistency conditions of the bianisotropic model, i.e. if the material is in fact local it must verify $\mu_{\mathrm{eff}}^{(1)} = \mu_{\mathrm{eff}}^{(2)} = \mu_{\mathrm{eff}}^{(3)}$, where $\mu_{\mathrm{eff}}^{(1)}$ is the magnetic permeability extracted using Eq. (2.9).

II.2.2.3 2D-FDFD Discretization

In Ref. [2] it was shown that the Method of Moments (MoM) may be used to numerically compute the nonlocal dielectric function $\overline{\overline{\varepsilon_{\mathrm{eff}}}}\left(\omega,\mathbf{k}\right)$. However, it is well known that the MoM is mainly suitable for the characterization of metallic structures, being less efficient in scenarios wherein the metamaterial is composed by dielectric inclusions.

In fact, finite differences (FD) methods are usually much more versatile and powerful [27]. In general, either in the frequency or time domains, FD methods are excellent to model devices with a complex geometry or structures of finite size. They are accurate and stable methods where the sources of error such as the grid resolution, nonphysical reflections from the grid boundaries, and the effect of representing curved surfaces on a Cartesian grid, are well modeled and understood. For example in Ref. [28], also based on the nonlocal homogenization formalism, a robust and efficient finite differences time domain (FDTD) algorithm was proposed to compute the effective nonlocal dielectric function of metamaterials formed by either metallic and/or metallic inclusions embedded in a host medium.

As described in Sec. II.2.2.1, the first step of the algorithm used to extract the nonlocal dielectric function consists in determining the microscopic electric fields along the unit cell of the metamaterial. For the sake of simplicity it is assumed that the electromagnetic field is TE^{-z} polarized and hence it has only the e_x, e_y and h_z Cartesian components. It is also assumed that the wave vector is restricted to the *xoy* plane $(k_z = 0)$. Hence, in such case, the problem to be solved [Eq. (2.1)] reduces to:

$$\begin{cases} \dfrac{\partial^2 e_y}{\partial x \partial y} - \dfrac{\partial^2 e_x}{\partial_y^2} - \left(\dfrac{\omega}{c}\right)^2 \varepsilon_{\mathrm{r}} e_x = i\omega\mu_0 j_{e,x} \\ \dfrac{\partial^2 e_x}{\partial x \partial y} - \dfrac{\partial^2 e_y}{\partial_x^2} - \left(\dfrac{\omega}{c}\right)^2 \varepsilon_{\mathrm{r}} e_y = i\omega\mu_0 j_{e,y} \end{cases}. \tag{2.14}$$

In the above, $j_{e,x}$ and $j_{e,y}$ are the components of the applied current density ($\mathbf{j}_e = \mathbf{j}_{e,\mathrm{av}} e^{i\mathbf{k}.\mathbf{r}}$) along the x and y coordinates, respectively.

Here, a FDFD numerical formalism to solve the nonlocal homogenization formalism is developed. Being a frequency-domain method, it is able to resolve sharp resonances and obtain solutions at a single frequency more efficiently than time-domain methods. In the FD method the unit cell Ω is divided into many rectangular grids. A portion of the grid with a dielectric inclusion is illustrated in Fig. 2.3.

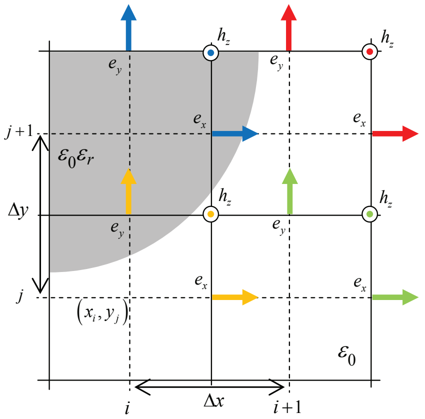

Fig. 2.3. Geometry of the grid mesh for the FDFD method. The nodes are spaced by Δx and Δy along the x- and y-directions, respectively. The shaded region represents a portion of the dielectric inclusion with dielectric permittivity ε_r.

In order to discretize the derivates of the microscopic electric fields in Eq. (2.14) the FDFD formulas proposed in [29] are employed:

$$\frac{\partial^2 e_y}{\partial x^2}(i,j) = \frac{e_y(i+1,j) - 2e_y(i,j) + e_y(i-1,j)}{(\Delta x)^2} \tag{2.15a}$$

$$\frac{\partial^2 e_y}{\partial x \partial y}(i,j) = \frac{e_y(i+1,j) - e_y(i,j) - e_y(i+1,j-1) + e_y(i,j-1)}{\Delta x \Delta y} \tag{2.15b}$$

$$\frac{\partial^2 e_x}{\partial y^2}(i,j) = \frac{e_x(i,j+1) - 2e_x(i,j) + e_x(i,j-1)}{(\Delta y)^2} \tag{2.15c}$$

$$\frac{\partial^2 e_x}{\partial x \partial y}(i,j) = \frac{e_x(i,j+1) - e_x(i,j) - e_x(i-1,j+1) + e_x(i-1,j)}{\Delta x \Delta y}, \tag{2.15d}$$

where Δx and Δy is the grid spacing along the x- and y- directions, respectively (Fig. 2.3). The discrete indices (i,j) attached to the field components are such that $e_x(i,j) \equiv e_x\big|_{(x_i+\Delta x/2,y_j)}$, $e_y(i,j) \equiv e_y\big|_{(x_i,y_j+\Delta y/2)}$, where (x_i, y_j) are the Cartesian coordinates of the considered node (see Fig. 2.3). If the mesh of Fig. 2.3 has N nodes in the unit cell, then there are $2N$ unknowns, as each node corresponds two components of the electric field, e_x and e_y respectively. The microscopic magnetic field $h_z = \frac{1}{i\omega\mu_0}\left(\frac{\partial e_y}{\partial x} - \frac{\partial e_x}{\partial y}\right)$ is calculated using the formula [27]:

$$h_z(i,j) = \frac{1}{i\omega\mu_0}\left(\frac{e_y(i+1,j) - e_y(i,j)}{\Delta x} - \frac{e_x(i,j+1) - e_x(i,j)}{\Delta y}\right), \tag{2.16}$$

being $h_z(i,j) \equiv h_z\big|_{(x_i+\Delta x/2,\, y_j+\Delta y/2)}$. All the nodes situated at the boundary of the unit cell have some adjacent nodes lying outside the unit cell, but they can be “brought back” using the Bloch-Floquet periodic boundary conditions,

$$\phi(x+a, y+b) = e^{ik_x a + ik_y b}\phi(x,y). \tag{2.17}$$

In the formula above, $\phi(x,y)$ is any microscopic field component, k_x, k_y and a, b are the wave vector components and the lattice constants along the x- and y- directions, respectively. Substituting Eqs. (2.15) into the linear system of equations (2.14) and taking into account the Bloch-Floquet boundary conditions (2.17), it is possible to reduce the homogenization problem to a standard linear system that can be numerically solved with respect to the unknowns (microscopic electric field components at the grid nodes). In such a manner it is possible to obtain the microscopic fields along the unit cell, which are then used to compute the nonlocal dielectric function as described in II.2.2.1. Moreover, since the problem under discussion is effectively two-dimensional it is only needed to solve two excitation problems (rather than three excitation problems as in three-dimensional scenarios) to retrieve the nonlocal dielectric function.

II.3. Application of the Homogenization Method

II.3.1. Computation of the Effective Parameters of Quasi-Local Media

In this section of the thesis, in order to validate the FDFD numerical code developed in Sec. II.2.2.3, the effective parameters are computed for metamaterials formed by cylindrical inclusions. Such metamaterials are characterized by a nearly local electromagnetic response, i.e., their effective medium can be accurately described by the bianisotropic constitutive relations [Eq. (2.8)]. Thus, the electromagnetic responses of these metamaterials verify to a good approximation the consistency conditions of the bianisotropic model described in Sec. II.2.2.2. Moreover, due do the cylindrical shape of the inclusions, the respective metamaterials have inversion symmetry, and hence the magneto-electric coupling is inexistent ($\overline{\overline{\xi}} = \overline{\overline{\zeta}} = 0$).

II.3.1.1 Dielectric Cylinders

To begin with, the dielectric function is computed for a metamaterial formed by lossless cylindrical dielectric inclusions with circular cross-section and dielectric constant ε_r with $\varepsilon_r \geq 1$. The cylindrical inclusions with radius R stand in air and are arranged in a square lattice with period a (see inset of Fig. 2.4a). The effective dielectric function (Fig. 2.4) is computed for $\mathbf{k} = 0$ and for the normalized frequency $\omega a / c = 0.001$ (quasi-static regime). A uniform mesh with $\Delta x = \Delta y = a/34$ is used. The computation time for each sample is approximately 15s in a standard personal computer [30].

The calculated permittivity is compared with the effective permittivity extracted from the band structure of the periodic material (slope of the fundamental mode near the origin of the Brillouin zone) using the hybrid plane-wave integral-equation-based method described in Refs. [31, 32].

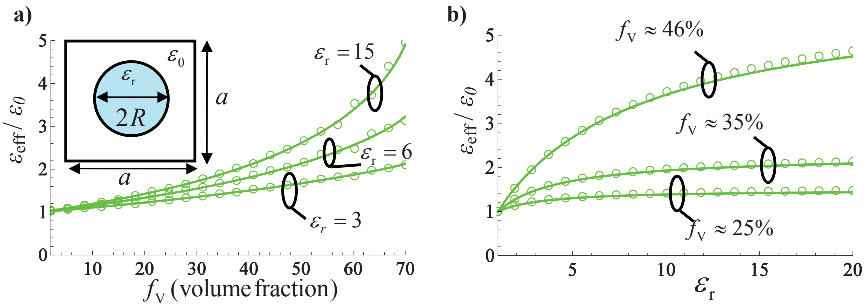

Fig. 2.4. (a): Quasi-static effective permittivity as a function of the volume fraction $f_{\rm V}$ (in percentage) of the inclusions for different values of the permittivity $\varepsilon_{\rm r}$. (b): effective permittivity as a function of $\varepsilon_{\rm r}$ for different values of $f_{\rm V}$. The discrete symbols in (a) and (b) correspond to the values computed with the homogenization method and the solid lines are obtained from the slope of the band structure of the material at the origin of the Brillouin zone. The geometry of the unit cell of the two dimensional metamaterial is shown in the inset: the unit cell consists of a cylindrical inclusion with circular cross-section, radius R , and permittivity $\varepsilon_{\rm r}$.

In Fig. 2.4a the computed results are shown as a function of the volume fraction of the cylinders for different values of the permittivity: $\varepsilon_{\rm r}=3$, $\varepsilon_{\rm r}=6$ and $\varepsilon_{\rm r}=15$. It can be seen that the results obtained using the homogenization method concur very well with the results obtained from the slope of the band structure at the origin of the Brillouin zone. As expected, the effective permittivity increases with the volume fraction of the cylinders. In Fig. 2.4a, the effective permittivity is plotted as a function of the relative permittivity of the cylinders, now for a fixed volume fraction of the inclusions. It is seen that the effective permittivity is more sensitive to the variation of $\varepsilon_{\rm r}$ for cylinders with large radii.

In a second example, both $\varepsilon_{\rm eff}$ and $\mu_{\rm eff}$ are extracted for a mixture of lossless high-index cylinders with permittivity $\varepsilon_{\rm r}=56$ and normalized radius $R=0.4a$ (Fig. 2.5), also standing in air. It has been reported in the literature that metamaterials formed by a mixture of cylinders with large dielectric constant may exhibit a strong magnetic response due to the excitation of the Mie resonance in the particles [33]. Related configurations (with spherical inclusions) have been studied to mimic the response of an isotropic double-negative medium [34, 35]. Using the FDFD implementation of the nonlocal homogenization model, the effective parameters of the considered system are computed as a function of the normalized frequency $\omega a / c$ (Fig. 2.5). Consistent with Ref. [33], it can be seen that the composite material may have an effective response very different from that of its non-magnetic dielectric constituents, and in particular that the magnetic response may be greatly enhanced near $\omega a / c \approx 0.8$, while the electric response has a sharp resonance around $\omega a / c \approx 1.2$.

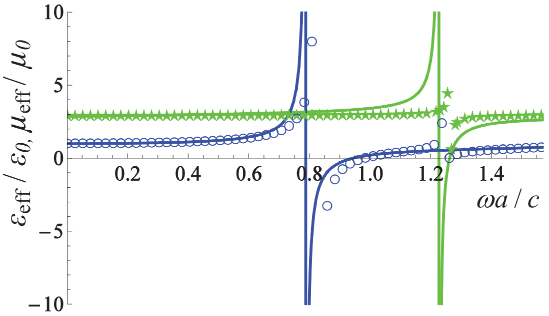

Fig. 2.5. Effective permittivity $\varepsilon_{\mathrm{eff}}$ (green curves) and permeability μ_{eff} (blue curves) as a function of the normalized frequency $\omega a / c$. The discrete symbols correspond to the values extracted with the FDFD method and the solid lines are the values obtained using the Clausius-Mossotti formula. The high-index cylindrical-shaped inclusion has a radius $R = 0.4a$ and permittivity $\varepsilon_{\mathrm{r}} = 56$. The host material is air.

The obtained results are compared with those predicted by the Clausius-Mossotti mixing formula (the expressions of the dynamic electric and magnetic polarizabilities can be found in Ref. [36]). As can be seen in Fig. 2.5, despite the relatively large diameter of the cylinders, the results extracted with the FDFD method agree surprisingly well with those obtained using the Clausius-Mossotti formula. This indicates that the interaction between the inclusions is predominantly of the dipole type.

II.3.1.2 Plasmonic Cylinders

Particles with a plasmonic response are important building blocks of optical metamaterials. Several configurations that exploit the existence of plasmonic resonances (which occur even for extremely subwavelength particles) in order to tailor the effective properties of a composite material (notably the magnetic response in the optical regime) have been put forward in the literature [37-39]. Thus, it is relevant to characterize the optical response of a metamaterial formed by an array of such particles. For simplicity, it is supposed that the complex permittivity of the inclusions is described by the Drude model $\varepsilon_r(\omega) = 1 - \frac{\omega_p^2}{\omega(\omega + i\Gamma)}$, where ω_p is the plasma frequency and Γ is the collision frequency. The Drude dispersion model may describe accurately the response of noble metals through the infrared and optical regimes. It is assumed that the normalized plasma frequency satisfies $\omega_p a / c = 1$, where a is the lattice period. The inclusions stand in air, are arranged in a square lattice and have a normalized radius $R = 0.45a$. Note that these parameters are the same as in Ref. [37].

The extracted permittivity ($\varepsilon_{\mathrm{eff}} = \varepsilon_{\mathrm{eff}}\left(\omega, \mathbf{k} = 0\right)$) is depicted in Fig. 2.6 as a function of the normalized frequency ω / ω_p. Clearly, the effective permittivity of the metamaterial has several sharp singularities, especially close to the frequency $\omega / \omega_p = 0.7$, which corresponds to the surface plasmon resonance for a single cylindrical particle ($\varepsilon_{\mathrm{r}} = -1$). This irregular behavior of the electric response is a consequence of the excitation of multiple quasi-static resonances that are characteristic of closely coupled plasmonic particles, consistent also with the results of Ref. [37], which showed that in general the material may support almost dispersionless bulk plasmons, propagating plasmon polaritons, and modes associated with high-multipole resonances. In Ref. [37] it was shown that these “high-multipole resonances” may be associated with a regime where the structure behaves as a double negative material. This is indeed supported by the developed FDFD homogenization method. It is shown in Fig. 2.6 that in the vicinity of $\omega / \omega_p = 0.63$ both the effective permittivity and the effective permeability are simultaneously negative (the effective permeability is plotted in the inset of Fig. 2.6, and is evaluated using Eq. (2.9)). In particular, the FDFD results yield that at $\omega / \omega_p = 0.637$ the effective permittivity is $\varepsilon_{\text{eff}} = -0.56$ and the effective permeability is $\mu_{\text{eff}} = -2.35$, consistent with the values reported in Ref. [37] for a nearby frequency ($\varepsilon_{\text{eff}} = -0.427$ and $\mu_{\text{eff}} = -2.35$ at $\omega / \omega_p = 0.6$).

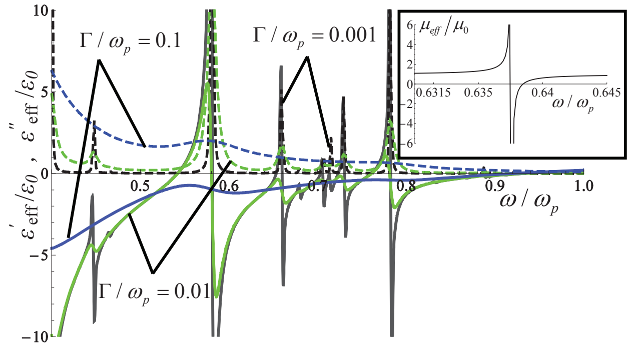

Fig. 2.6. Real and imaginary parts of the effective permittivity $\varepsilon_{\text{eff}} / \varepsilon_0 = \varepsilon' + i\varepsilon''$ as a function of the normalized frequency ω/ω_p, for a mixture with plasmonic-cylinders arranged in a regular lattice, for different values of the damping frequency: $\Gamma / \omega_p = 0.001$ (black curves), $\Gamma / \omega_p = 0.01$ (green curves) and $\Gamma / \omega_p = 0.1$ (blue curves). The solid lines correspond to the real part of ε_{eff} while the dashed lines represent the imaginary part. The host material is air. The inset shows the real part of the effective magnetic permeability ($\Gamma / \omega_p = 0.001$) of the system in the vicinity of $\omega / \omega_p = 0.64$.

When the absorption is increased, i.e. Γ is increased, so that the surface plasmon polaritons are more damped, the somewhat irregular behavior of the electric response tends to disappear. The effect of loss is particularly important at the frequencies associated with the plasmonic resonances. In Ref. [40] it was shown that similar to this example, the effective permittivity (in the quasi-static regime) of a metamaterial formed by square-shaped tilted plasmonic inclusions with sharp corners also has several singularities which are a consequence of the excitation of multiple quasi-static plasmonic resonances. Such a property was also validated and confirmed in Ref. [J.5] using the FDFD implementation of the nonlocal homogenization formalism.

II.3.1.3 Zero-Index Media

Zero-index media is a class of metamaterials with index of refraction equal to zero (or near zero) at a given frequency of operation. Due to the relatively long wavelengths intrinsic to these materials, they may have interesting potentials in tunneling electromagnetic energy through narrow channels and bends [36, 41, 42], to increase the directivity of an antenna [43], to manipulate the shape of wave fronts [44], and to design metamaterials with a broadband negative refraction and imaging with super resolution [J.3]. In general, zero-index media are strongly mismatched with free-space due to the huge difference between the wave impedance $\eta = \sqrt{\mu / \varepsilon}$ in such materials and free-space. Nevertheless, when both the permeability and the permittivity are near zero, the metamaterial may have near zero-index and may be matched to the free-space. The possibility of matching the response of the metamaterial with that of free-space will be further discussed in the next Chapter.

Clearly, the realization of a material with such properties is not a trivial matter. One possibility to realize zero-index materials relies on racemic mixtures of left-handed and right-handed helices of certain pitch angle, as considered in [45]. In 2007 [36], a different strategy to obtain a material with simultaneously near zero permittivity and permeability was explored. It was shown that such material may be easily implemented provided a material with near zero permittivity (and no magnetic response) is somehow available. This may be the case of some metals at optical and UV frequencies, and some semiconductors and polar dielectrics at infrared frequencies. Specifically, it was shown in Ref. [36] that by embedding dielectric particles with suitable size and permittivity in a host background with near zero permittivity it may be possible to realize a composite material with simultaneously near zero permittivity and permeability. In this section of the thesis, the effective parameters of such zero-index composite materials are characterized. For simplicity, it is supposed that the geometry of the metamaterial is similar to that of Sec. II.3.1.1. Specifically, the metamaterial is formed by lossless cylindrical-shaped inclusions with normalized radius $R / a = 0.4$ and arranged in a square lattice. However, instead of being embedded in air, it is considered that the cylindrical inclusions are embedded in an epsilon-near zero (ENZ) host medium $(\varepsilon_h \approx 0)$. It was demonstrated in Ref. [36] that at the frequency where $\varepsilon_{\mathrm{h}} = 0$, the effective permittivity of the composite material vanishes, whereas the effective permeability is given by the following exact formula.

$$\mu_{\mathrm{eff}} = \mu_0 \left(\frac{A_{\mathrm{h,cell}}}{A_{\mathrm{cell}}} + \frac{2\pi R^2}{A_{\mathrm{cell}}} \frac{1}{k_{\mathrm{r}} R} \frac{J_1(k_{\mathrm{r}} R)}{J_0(k_{\mathrm{r}} R)} \right), \qquad \text{at} \qquad \omega = \omega_p \tag{2.18}$$

where, $A_{\mathrm{h,cell}} = A_{\mathrm{cell}} - \pi R^2$, $k_{\mathrm{r}} = \omega\sqrt{\varepsilon_{\mathrm{r}}\varepsilon_0\mu_0}$ and J_l is the Bessel function of 1st kind and order l.

As a further validation of the FDFD numerical code described in Sec. II.2.2.3, the effective permeability of this composite material was computed. The effective permeability is written in terms of the derivatives of the nonlocal dielectric function with respect to the wave vector [Eq. (2.9)]. The calculated result is shown in Fig. 2.7 (discrete symbols) as a function of the relative dielectric permittivity of the cylinders ε_{r}, and compares very well with the exact result given by Eq. (2.18) (solid line). It may be seen that the magnetic response has a resonance when $\varepsilon_{\mathrm{r}} \approx 36$ and that the permeability is near zero, $\mu_{\mathrm{eff}} \approx 0$, when $\varepsilon_{\mathrm{r}} \approx 56$.

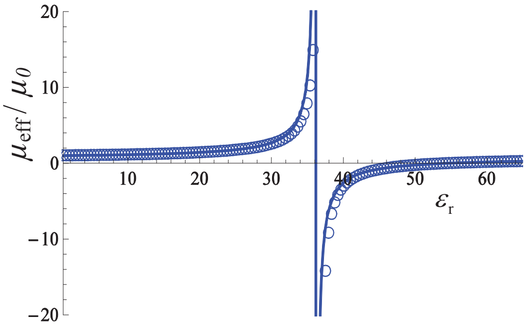

Fig. 2.7. Effective permeability μ_{eff} as a function of the permittivity ε_{r} of dielectric cylinders arranged in a square lattice and embedded in a host medium with permittivity near to zero ($\varepsilon_{\mathrm{h}} \approx 0$). The cylindrical-shaped inclusions have normalized radius $R = 0.4a$. The solid curve was obtained using the formula derived in Ref. [36] and the discrete symbols were obtained with the FDFD method.

In order to study the frequency response of the metamaterial, the effective permittivity and the effective permeability are calculated as functions of frequency. It is assumed that the host permittivity (ε_h) is described by the Drude dispersion model, and that the permittivity of the cylinders is independent of frequency, such that $\varepsilon_\mathrm{r} = 56$. The normalized plasma frequency verifies $\omega_p a / c = 1.0$ and the collision frequency is such that $\Gamma / \omega_p = 0.001$. Figure 2.8a shows the extracted effective parameters (discrete symbols) as function of the normalized frequency ω / ω_p, showing that consistent with the theory of [36], both the permittivity and permeability are near zero at the plasma frequency: $\varepsilon_\mathrm{eff}(\omega_p) = \mu_\mathrm{eff}(\omega_p) \approx 0$. The solid lines in Fig. 2.8a represent the effective parameters predicted by the Clausius-Mossotti mixing formula (see Ref. [36]), and it can be seen that the general agreement with the data extracted with the FDFD homogenization model is quite good. It can also be seen in Fig. 2.8a that in the frequency window $0.8 \le \omega/\omega_p \le 1$, both the effective permittivity and permeability are negative and hence the material behaves as a double negative (DNG) material. This topic will be further developed in Chapter III. In Fig. 2.8b the amplitude of the electric field component e_y is shown at different frequencies of operation marked in Fig. 2.8a, and supposing that the excitation $\mathbf{j}_e = \mathbf{j}_{e,\mathrm{av}} e^{i\mathrm{k.r}}$ is directed along y and $\mathbf{k} = 0$. It may be seen in Fig. 2.8b (i) that when $\omega/\omega_p \approx 1$ ($\varepsilon_\mathrm{h} \approx 0$) the electric field does not penetrate into the cylinder and is strongly concentrated in the ENZ region, so that the spatially average electric displacement vector $\langle d_y \rangle = \langle \varepsilon e_y \rangle$ vanishes ($\varepsilon_\mathrm{eff} \approx 0$). The situation is quite different at the resonance of the electric response , $\omega/\omega_p \approx 1.282$, as shown in Fig. 2.8b (ii).

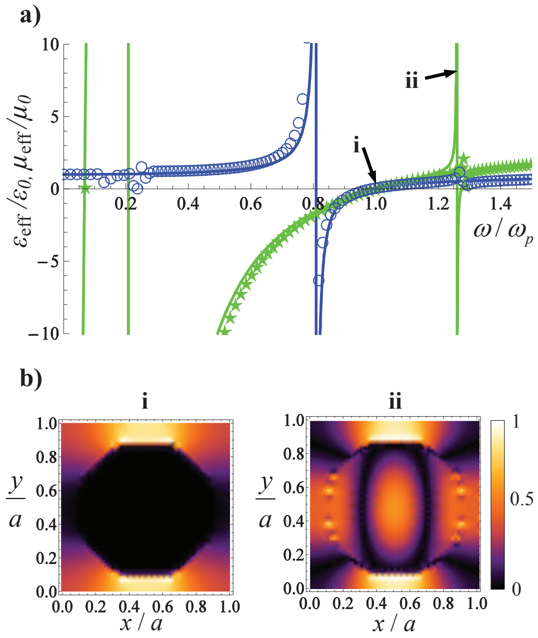

Fig. 2.8. (a) Real parts of the effective permittivity ε_{eff} (green curves) and permeability μ_{eff} (blue curves) as a function of the normalized frequency ω/ω_p. The discrete symbols correspond to the values extracted with the FDFD method and the solid lines were obtained using the Clausius-Mossotti formula. The inclusion has a radius $R = 0.4$ and permittivity $\varepsilon_r = 56$ and the host medium is characterized by a Drude type dispersion model. (b) normalized amplitude of the electric field component e_y in the unit cell (when the current source is directed along y at the frequency where the effective permittivity hits a resonance (ii) and when $\varepsilon_{\text{eff}} \approx 0$ (i).

II.3.2. Computation of the Effective Parameters of Nonlocal Media

Next, the effective response of a metamaterial composed by plasmonic inclusions shaped as a horseshoe is studied. It is shown that because of the asymmetric shape of the inclusions, the bianisotropic effects must be considered and hence the relevant magneto-electric tensors are computed using Eqs. [2.12]. Moreover, using the consistency conditions of the local model described in Sec. II.2.2.2 it is shown that the effective response of the metamaterial is spatially dispersive, and therefore it cannot be fully described by the bianisotropic relations [Eq. (2.8)].

II.3.2.1 Horseshoe Inclusions

An interesting proposal to obtain a strong magnetic response using plasmonic nanoparticles is based on nanostructures shaped as a horseshoe. It was shown in Ref. [46]

that such "U-shaped nanoantennas" with dimensions much smaller than the light wavelength can have a magnetic plasmon resonance with resonant frequency depending on the shape and material properties rather than on the wavelength.

The two-dimensional metamaterial consists of metallic nanoantennas arranged in a square lattice (see inset of Fig. 2.9a). The permittivity ε_{r} of the inclusions follows the Drude dispersion model, being the normalized plasma frequency $\omega_p a/c = 30.0$ and the collision frequency $\Gamma/\omega_p = 0.001$. The normalized thickness of the "arms" of the nanoantennas is $b/a = 0.18$ and the distance between the opposite arms is $d/a = 0.26$. Using the homogenization FDFD method, the effective permeability μ_{eff} of the composite material is calculated as a function of the normalized frequency $\omega a/c$ (solid line Fig. 2.9a). As in the examples of Sec. II.3.1, the effective permeability is calculated from the second order derivatives of the nonlocal dielectric function with respect to the wave vector [Eq. (2.9)]. The homogenization method predicts that there is a magnetic resonance around $\omega a/c = 1.47$. It is interesting to compare the FDFD-homogenization results with the effective parameters obtained with the well-known method of extraction based on the inversion of the reflection and transmission coefficients [8, 9]. In order to calculate the required reflection and transmission coefficients (for a metamaterial with one layer thickness), a commercial full-wave electromagnetic simulator [47] is used. The extracted parameters are also shown in Fig. 2.9a (discrete symbols), revealing a fair agreement with the FDFD-homogenization results. It may be seen that the resonance is slightly shifted to higher frequencies and that the magnetic response is weaker. The justification for these properties may be that the effective permeability extracted with the FDFD method is a parameter intrinsic to the periodic material (bulk permeability), whereas the method of extraction reported in Refs. [8, 9] depends on the thickness of the metamaterial slab (in the simulation a mono-layer) as well on interface effects.

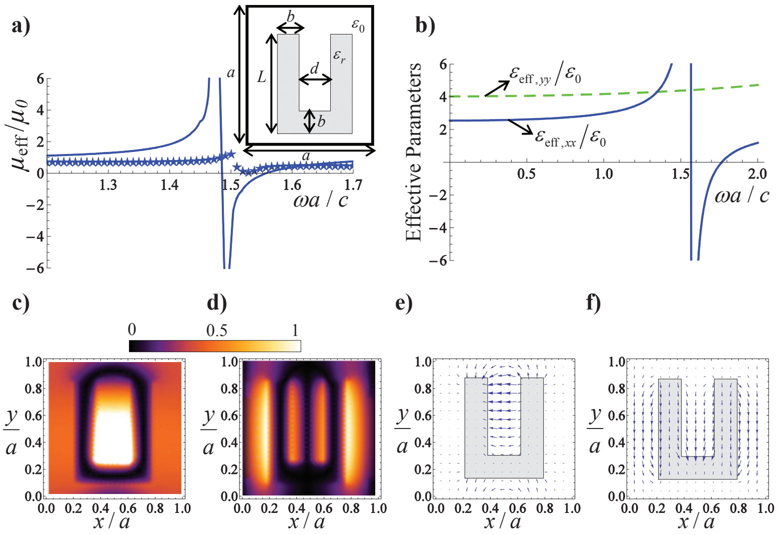

Fig. 2.9. (a) Real part of the effective permittivity $\mu_{\rm eff}$ as a function of the normalized frequency $\omega a/c$. Solid line: homogenization method desccribed in this thesis; Discrete symbols: parameters extracted using the inversion of the reflection and transmission coefficients [8, 9]. The geometry of the unit cell is shown in the inset and consists of a U-shaped plasmonic inclusion with complex permittivity ε_r. The arms of the horseshoe have a normalized thickness $b = 0.18a$ and normalized length $L = 0.79a$. The distance between the two arms is $d = 0.26a$. (b) Real parts of $\varepsilon_{{\rm eff},xx}(\omega,\mathbf{k}=0)$ (blue solid curve) and $\varepsilon_{{\rm eff},yy}(\omega,\mathbf{k}=0)$ (green dashed curve) as a function of the frequency. The host medium is air. (c) and (d) normalized amplitude of the magnetic field h_z in the unit cell, when the current source is directed along x and y respectively, at $\omega a/c \approx 1.47$. (e) and (f) represent the real part of the electric field vector $\mathbf{e}$ in the unit cell, when the current source is directed along x and y respectively.

Figure 2.9b shows the real part of the effective permittivity components $\varepsilon_{{\rm eff},xx}(\omega,\mathbf{k}=0)$ and $\varepsilon_{{\rm eff},yy}(\omega,\mathbf{k}=0)$ along the two principal directions of the structure, x and y respectively, as a function of frequency. It can be seen that the dielectric function along the y axis $\varepsilon_{{\rm eff},yy}$ (dashed green curve) is barely sensitive to the variation of the frequency whereas $\varepsilon_{{\rm eff},xx}$ hits a resonance at $\omega a/c \approx 1.57$. This resonance is a consequence of the coupling between the electric and magnetic fields (bianisotropy) existent in this structure. This will be further discussed ahead.

Figures 2.9c and 2.9d show the normalized amplitude of the magnetic field $h_z/h_{z,\max}$ (at $\omega a/c = 1.47$, and for the same material parameters as in the example of Fig 2.9a) when the external current source is directed along x and y (supposing that $\mathbf{k}=0$), respectively. Likewise, Figs. 2.9e and 2.9f show snapshots (at t=0) of the microscopic electric field vector $\mathbf{e}$ in the unit cell when the current source is directed along x and y, respectively. It can be easily shown from the Maxwell's Equations that for $\mathbf{k}=0$ the external excitation enforces a nonzero external electric field in the system, while the external magnetic induction field vanishes. In other words, if $\mathbf{k}=0$, only the electric response is excited. Consistent with this property, it is seen from Fig. 2.9f (current source directed along y) that the electric field distribution is somewhat similar to that of two electric dipoles. Figure 2.9d (current source directed along y) shows that the induced current flows from one end to the other in each arm of the horseshoe, creating two magnetic fields that cancel out in all the points with coordinates $x/a=0.5$.

On the other hand, when the current source is directed along x (Figs. 2.9c and 2.9e), i.e. $\mathbf{j}_e = j_e \hat{\mathbf{u}}_x$, the magnetic field h_z and the electric field are highly concentrated between the arms of the horseshoe. Even though $\mathbf{k}=0$, such field distribution corresponds to the excitation of a magnetic resonance of the system. This occurs due to the lack of inversion symmetry of the considered material, which permits the emergence of bianisotropic effects. Thus, even though the external excitation is purely electric $(\mathbf{k}=0)$, the field distribution in Figs. 2.9c and 2.9e is mostly determined by the magnetic response of the metamaterial, since the metamaterial is operated close to the magnetic resonance (see Fig. 2.9a).

To demonstrate in a conclusive manner the emergence of the bianisotropic effects, the magneto-electric coupling parameters ζ_{zx} and ζ_{zy} of the metamaterial are calculated using Eq. (2.12). The numerical simulations predict (not shown here) that $\zeta_{zy} \approx 0$, consistent with the fact that the structure of this metamaterial is invariant under the transformation $(x,y,z) \to (-x,y,z)$. On the other hand, the amplitude of the parameter ζ_{zx} may be quite significant.

Figure 2.10 depicts $\operatorname{Im}\{\zeta_{zx}\}$ as a function of frequency (for a lossless metamaterial the tensor $\overline{\overline{\zeta}}$ is purely imaginary [26]), showing that it exhibits the same behavior as the magnetic permeability, hitting a resonance at nearly the same frequency ($\omega a/c = 1.47$). Figure 2.10 depicts the frequency dependence of $\varepsilon_{\text{eff},xx}(\omega, \mathbf{k}=0)$ (also shown in Fig. 2.9b), which, from Eq. (2.10), is related to the local parameters through the relation $\varepsilon_{\text{eff},xx}(\omega, \mathbf{k}=0) = \varepsilon_{xx} + \frac{1}{c^2}\zeta_{zx}^2 \frac{1}{\mu_{eff}}$, where ε_{xx} is the relative *local* permittivity along x. Interestingly, the previous formula predicts that in presence of bianisotropic effects, $\varepsilon_{\text{eff},xx}$ has a resonance at the frequency where the permeability vanishes. This is confirmed by Fig. 2.10, which shows that at $\omega a/c \approx 1.55$ the magnetic permeability vanishes and the xx component of the nonlocal dielectric function has a pole.

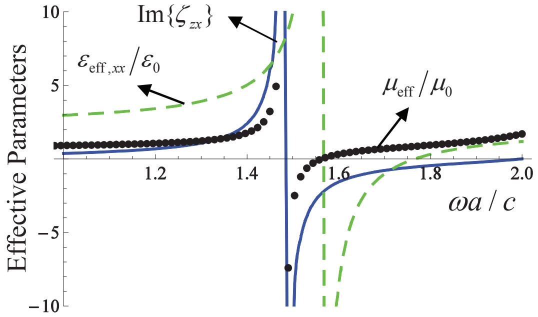

Fig. 2.10. Nonlocal dielectric function along the x-direction (green dashed line), effective permeability (black dotted line) and magneto-electric parameter (blue solid line) for the horseshoe geometry of Fig. 2.9a.

As already mentioned in Sec. II.2.2.2, the extraction of the material parameters (ζ_{zx}, μ_{eff}, ε_{xx}, and ε_{yy}) is based on the assumption that the effective medium can be accurately described by the bianisotropic constitutive relations [Eq. (2.8)]. In these conditions, the nonlocal dielectric function is necessarily a quadratic form of the wave vector [Eq. (2.7)]. In particular, it should be clear that the magnetic permeability μ_{eff} should completely determine the spatial dispersion effects of second order, or equivalently it should univocally determine the second order derivatives of the nonlocal dielectric function $\overline{\overline{\varepsilon_{\text{eff}}}}$ with respect to $\mathbf{k}$. As already mentioned, if a metamaterial is local it must verify the consistency conditions of the bianisotropic model, i.e., it must verify $\mu_{\text{eff}}^{(1)} = \mu_{\text{eff}}^{(2)} = \mu_{\text{eff}}^{(3)}$ where $\mu_{\text{eff}}^{(1)}$ is the magnetic permeability extracted using Eq. (2.9), and $\mu_{\text{eff}}^{(2)}$ and $\mu_{\text{eff}}^{(3)}$ are calculated using Eqs. (2.13a) and (2.13b), respectively. Figure 2.11 demonstrates that the consistency relations are not satisfied in the horseshoe configuration, because the curves describing each of the extraction formulas do not agree. Moreover, the curves associated with $\mu_{\text{eff}}^{(2)}$ and $\mu_{\text{eff}}^{(3)}$ exhibit a resonance with a nonphysical dispersion at $\omega a/c = 1.6$. This unsettling result implies that the magnetic permeability of the structure depends on the direction of propagation, and thus the response of the horseshoe particle cannot be fully described by the assumed bianisotropic relations [Eq. (2.8)].

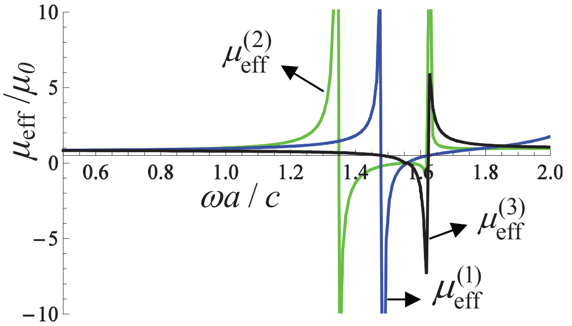

Fig. 2.11. Real part of the effective permittivity μ_{eff} as a function of the normalized frequency $\omega a/c$ considering different formulas for the extraction of μ_{eff}.

Indeed, it must be emphasized that a truly local material (with ζ_{zx}, $\mu_{\text{eff}}, \varepsilon_{xx}$, and ε_{yy} independent of $\mathbf{k}$) should satisfy $\mu_{\text{eff}}^{(1)} = \mu_{\text{eff}}^{(2)} = \mu_{\text{eff}}^{(3)}$, and hence, in general the horseshoe metamaterial should be regarded as nonlocal. The origin of the spatially dispersive response of the metamaterial may be related to the excitation of the electric quadrupole moment, which is known to have strength comparable to that of the magnetic dipole in other metamaterials with a topology similar to that of the horseshoe [48, 49]. The excitation of the electric quadrupole is a consequence of the fact that the induced electric current does not form a closed loop [48] (Figs. 2.9c and 2.9d). Indeed, it was numerically verified (not shown here) that to a very good approximation $\mu_{\mathrm{eff}}^{(1)} = \mu_{\mathrm{eff}}^{(2)} \approx \mu_{\mathrm{eff}}^{(3)}$ in the examples considered in Sec. II.3.1, wherein the metamaterials were formed by inclusions with circular cross-section, which force the induced current to circulate in a loop.

Another reason for the lack of consistency between $\mu_{\mathrm{eff}}^{(1)}$, $\mu_{\mathrm{eff}}^{(2)}$ and $\mu_{\mathrm{eff}}^{(3)}$ in the geometry of Fig. 2.9a may be the fact that the volume density of the horseshoe inclusions in that example is too high to expect a local response of the material (these high densities of particles are typical of metamaterials, and are necessary to have a strong magnetic response). When working with densely packed crystals the expansion of the dielectric function must include additional terms which are second-order with respect to $\mathbf{k}$ and possibly other terms of even higher orders. Physically, those terms are related to the higher-order multipole moments that are not taken into account by the bianisotropic constitutive relations [Eq. (2.8)].

It was also shown in Ref. [J.5] using the FDFD formalism (and confirmed using the inversion process of Refs. [8, 9]) that in order to obtain very subwavelength resonant horseshoe particles ($\omega_r a / c << 1$) the absolute value of the real part of the permittivity of the inclusions $-\varepsilon_{\mathrm{r}}'$ must be relatively small. Specifically, it was shown that in order to obtain ultra subwavelength particles, it is necessary that the skin depth of the metal, δ, is comparable to or larger than the thickness of the nanoantennas.

II.4. Concluding Remarks

In this chapter, a FDFD implementation of the nonlocal homogenization approach proposed in [2] was developed. It was demonstrated that the proposed numerical method may be an excellent solution to solve the homogenization problem, yielding very accurate results, and allowing for the computation of the effective parameters of metamaterials formed by dielectric and metallic inclusions with arbitrary shapes, taking into account both the effect of loss and frequency dispersion. The derived FDFD formalism was compared with several homogenization methods, demonstrating not only its accuracy but also its generality.

In particular, the electrodynamics of arrays of horseshoe shaped nanoparticles were analyzed, and it was emphasized the fact that such metamaterials may be characterized by significant magneto-electric coupling, as well as nonlocal effects that cannot be described by the usual bianisotropic constitutive relations. The developed formalism can be easily extended to fully three-dimensional structures.

References

[1] J. van Kranendonk and J. E. Sipe, "Foundations of the macroscopic electromagnetic theory of dielectric media," chapter 5 in *Progress in Optics XV*, (ed. by E. Wolf), New York: North-Holland, 1977.

[2] M. G. Silveirinha, "Metamaterial homogenization approach with application to the characterization of microstructured composites with negative parameters," *Phys. Rev. B* **75**, 115104, 2007.

[3] G. Russakov, "A derivation of the macroscopic Maxwell Equations," *Am. J. Physics* **38**, 1188, 1970.

[4] J. Sipe and J. V. Kranendonk, "Macroscopic electromagnetic theory of resonant dielectrics," *Phys. Rev. A* **9**, 1806, 1974.

[5] J.-M. Lerat, N. Malléjac, and O. Acher, "Determination of the effective parameters of a metamaterial by field summation method," *J. Appl. Phys.* **100**, 084908, 2006.

[6] David R. Smith and John B. Pendry, "Homogenization of metamaterials by field averaging (invited paper)," *J. Opt. Soc. Am. B* **23**, 391, 2006.

[7] J. D. Jackson, *Classical Electrodynamics*, Sect. 6.6, Wiley, 1998.

[8] D. R. Smith and S. Schultz, "Determination of effective permittivity and permeability of metamaterials from reflection and transmission coefficients," *Phys. Rev. B* **65**, 195104, 2002.

[9] X. Chen, T. M. Grzegorczyk, Bae-Ian Wu, J. Pacheco, Jr., and J. A. Kong, “Robust method to retrieve the constitutive effective parameters of metamaterials,” *Phys. Rev. E* **70**, 016608, 2004.

[10] C. R. Simovski and S. A. Tretyakov,” Local constitutive parameters of metamaterials from an effective-medium perspective,” *Phys. Rev. B* **75**, 195111, 2007.

[11] C. R. Simovski, ” Bloch material parameters of magneto-dielectric metamaterials and the concept of Bloch lattices,” *Metamaterials* **1**, 62, 2008.

[12] S. Datta, C.T. Chan, K. M. Ho, and C. M. Soukoulis, “Effective dielectric constant of periodic composite structures,” *Phys. Rev. B* **48**, 14936, 1993.

[13] M. G. Silveirinha, C. A. Fernandes, “Effective permittivity of metallic crystals: a periodic Green's function formulation,” *Electromagnetics* **8**, 647, 2003.

[14] O. Ouchetto, C.-W. Qiu, S. Zouhdi, L.-W. Li, A. Razek, “Homogenization of 3-D Periodic Bianisotropic Metamaterials,” *IEEE Trans. Microw. Theory Tech.* **54**, 3893, 2006.

[15] M. G. Silveirinha, in *Theory and Phenomena of Metamaterials* (*Handbook of artificial materials*), edited by Filippo Capolino (CRC, Cleveland), 2009..

[16] P. A. Belov, Y. Hao, and S. Sudhakran, “Subwavelength microwave imaging using an array of parallel conducting wires as a lens,” *Phys. Rev. B* **73**, 033108, 2006.

[17] G. Shvets, S. Trendafilov, J. B. Pendry, and A. Sarychev, “Guiding, focusing, and sensing on the subwavelength scale using metallic wire arrays,” *Phys. Rev. Lett.* **99**, 053903, 2007.

[18] M. G. Silveirinha, “Anomalous refraction of light colors by a metamaterial prism,” *Phys. Rev. Lett.* **102**, 193903, 2009.

[19] M. G. Silveirinha and C.A. Fernandes, “Nonresonant structured material with extreme effective parameters,” *Phys. Rev. B*(BR) **78**, 033108, 2008.

[20] T. A. Morgado, J. S. Marcos, M.G. Silveirinha, and S.I. Maslovski, “Ultraconfined Interlaced Plasmons,” *Phys. Rev. Lett.* **107**, 063903, 2011.

[21] V. Agranovich and V. Ginzburg, *Spatial Dispersion in Crystal Optics and the Theory of Excitons*, Wiley-Interscience, New York, 1966.

[22] P. A. Belov, R. Marqués, S. I. Maslovski, I. S. Nefedov, M. Silveirinha, C. R. Simovski, and S. A. Tretyakov, “Strong spatial dispersion in wire media in the very large wavelength limit,” *Phys. Rev. B* **67**, 113103, 2003.

[23] A. L. Pokrovsky and A. L. Efros, "Nonlocal electrodynamics of two-dimensional wire mesh photonic crystals," *Phys. Rev. B* **65**, 045110, 2002.

[24] V. M. Agranovich, Y. R. Shen, R. H. Baughman, and A. A. Zakhidov, "Linear and nonlinear wave propagation in negative refraction metamaterials," *Phys. Rev. B* **69**, 165112, 2004.

[25] E. M. Hornreich and S. Shtrikman, "Theory of gyrotropic birefringence," *Phys. Rev.* **171**, 1065, 1968.

[26] A. Serdyukov, I. Semchenko, S. Tretyakov, and A. Sihvola, *Electromagnetics of Bi-anisotropic Materials Theory and Applications*, 1st ed., Gordon and Breach Science, New York, 2001.

[27] A. Taflove and S. C. Hagness, *Computational Electrodynamics: The Finite-Difference Time-Domain Method*, Artech House, London, 2005.

[28] M. G. Silveirinha, "Time domain homogenization of metamaterials," *Phys. Rev. B* **83**, 165104, 2011.

[29] K. Yasumoto, *Electromagnetic Theory and Applications for Photonic Crystals Taylor and Francis*, New York, 2006.

[30] The numerical code was ran in a system with the Intel(R) Core(Tm)2 Quad CPU Q6600 @ 2.4 GHz processor.

[31] M. Silveirinha and C. A. Fernandes, "Efficient calculation of the band structure of artificial materials with cylindrical metallic inclusions," *IEEE Trans. Microwave Theory Tech.* **51**, 1460, 2003.

[32] M. G. Silveirinha and C. A. Fernandes, "Computation of the electromagnetic modes in 2D-photonic crystals: techniques to improve the convergence rate of the plane wave method," *Electromagnetics* **26**, 175, 2006.

[33] S. O'Brien and J. B. Pendry, "Photonic band-gap effects and magnetic activity in dielectric composites," *J. Phys.: Condens. Matter* **14**, 4035, 2002.

[34] I. Vendik, O. Vendik, and M. Odit, "An isotropic metamaterial formed with ferroelectric ceramic spherical inclusions," Microwave *Opt. Technol. Lett.* **48**, 2553, 2006.

[35] C. L. Holloway, E. F. Kuester, J. Baker-Jarvis, and P. Kabos, *IEEE Trans. Antennas Propag.* **51**, 2596, 2003.

[36] M. Silveirinha and N. Engheta, "Design of matched zero-index metamaterials using nonmagnetic inclusions in epsilon-near-zero media," *Phys. Rev. B* **75**, 075119, 2007.

[37] G. Shvets and Y. A. Urzhumov, "Engineering the electromagnetic properties of periodic nanostructures using electrostatic resonances," *Phys. Rev. Lett.* **93**, 243902, 2004.

[38] A. Alù, A. Salandrino, and N. Engheta, "Negative effective permeability and left-handed materials at optical frequencies," *Opt. Express* **14**, 1557, 2006.

[39] A. Alù and N. Engheta, "Three-dimensional nanotransmission lines at optical frequencies: A recipe for broadband negative-refraction optical metamaterials," *Phys. Rev. B* **75**, 024304, 2007.

[40] H. Wallén, H. Kettumen, and A. Sihvola, "Surface modes of negative-parameter interfaces and the importance of rounding sharp corners," *Metamaterials* **2**, 113, 2008.

[41] M. Silveirinha and N. Engheta, "Tunneling of electromagnetic energy through subwavelength channels and bends using ε-near-zero materials," *Phys. Rev. Lett.* **97**, 157403, 2006.

[42] B. Edwards, A. Alù, M. Young, M. G. Silveirinha, and N. Engheta, "Experimental verification of epsilon-near-zero metamaterial coupling and energy squeezing using a microwave waveguide," *Phys. Rev. Lett.* **100**, 033903, 2008.

[43] S. Enoch, G. Tayeb, P. Sabouroux, "A metamaterial for directive emission," N. Guerin, and P. Vincent, *Phys. Rev. Lett.* **89**, 213902, 2002.

[44] A. Alù, M. G. Silveirinha, A. Salandrino, and N. Engheta, "Epsilon-near-zero metamaterials and electromagnetic sources: Tailoring the radiation phase pattern," *Phys. Rev. B* **75**, 155410, 2007.

[45] S. Tretyakov, I. Nefedov, A. Sihvola, S. Maslovski, and C. Simovski, "Waves and energy in chiral nihility," *J. Electromagn. Waves Appl.* **17**, 695, 2003.

[46] A. K. Sarychev, G. Shvets, and V. M. Shalaev, "Magnetic plasmon resonance," *Phys. Rev. E* **73**, 036609, 2006.

[47] CST Microwave Studio Suite^{TM} 2010, (http://www.cst.com).

[48] A. Alù and N. Engheta, "Dynamical theory of artificial optical magnetism produced by rings of plasmonic nanoparticles," *Phys. Rev. B* **78**, 085112, 2008.

[49] D. J. Cho, F. Wang, X. Zhang, and Y. R. Shen, "Contribution of the electric quadrupole resonance in optical metamaterials," *Phys. Rev. B* **78**, 121101(R), 2008.

III. Negative Index Metamaterials

III.1. Introduction

In 1968, Veselago [1] theoretically investigated the electromagnetic behavior of a medium having both electric permittivity ε and magnetic permeability μ negative (DNG material) and concluded that such a medium would have propagation properties radically different from those of right-handed materials with both ε and μ greater than zero. Veselago argued that in such a medium the direction of the Poynting vector of a plane wave is oppositely directed to that of its phase velocity, suggesting that this isotropic medium supports backward wave propagation and also that its refractive index is negative. Based on Veselago's work, in 2000 Pendry suggested that a lossless material slab with negative index of refraction ($n = -1$ at a fixed frequency of operation) makes a perfect lens with resolution independent of the wavelength of operation and of the polarization of the light [2]. Since Pendry's seminal work, several authors have analyzed and proposed the design of metamaterial configurations whose effective response is characterized by a DNG regime in some frequency window [3-10], and in particular by an index of refraction $n = -1$ at a given frequency of operation [11-16]. A large variety of the physical effects associated with DNG materials as well as some of their very interesting potential applications were also highlighted and established in several works [17-22].

Even though some fundamental concepts such as negative permittivity and permeability are widely accepted and relatively well understood today, there are still some elementary concepts related with the physics of DNG metamaterials such as the "heating rate," "stored electromagnetic energy" and "Poynting vector" that remain a topic of discussion and controversy [23, 24]. More specifically, it has been discussed whether the classic definition of the Poynting vector, which defines the power flux per unit surface, should be modified or not when dealing with DNG metamaterials.

In this chapter, based on the effective response of the Zero-Index metamaterial analyzed in Chapter II (Sec. II.2.3.1), the physics of negative refraction is settled, showing that the Poynting vector and other power relations may be unambiguously defined consistently with the classic formulas for homogenous bulk media. Moreover, it is shown that the Zero-Index metamaterial may be an excellent route to design broadband DNG metamaterials and for achieving imaging with super resolution as well. Similar to Chapter II, in all the scenarios reported in this Chapter the electric field is assumed to lie in the *xoy* plane, whereas the magnetic field is directed along the *z*-direction.

III.2. Poynting Vector

III.2.1. Power Flux in Macroscopic Media

The Poynting vector is one of the cornerstones of the monument of Maxwell's theory. It is usually introduced starting from the calculation of the instantaneous time variation of the electromagnetic energy stored within a certain volume, which in vacuum is equal to the flux of $\mathbf{s} = \mathbf{e} \times \mathbf{b} / \mu_0$ through the boundary of the considered region [25, 26] (here, as in Chapter II, $\mathbf{e}$ and $\mathbf{b}$ represent the microscopic local fields and μ_0 is the free-space permeability). Although it is arguable whether $\mathbf{s}$ may be considered a local electromagnetic power density vector [25-27], its flux through an arbitrary closed surface is well known to represent the instantaneous rate of energy change in the interior volume. When dealing with an idealized continuous isotropic material other than vacuum, with local permittivity and permeability ε and μ, respectively, it is well established that its definition should be modified as $\mathbf{s} = \mathbf{e} \times \mathbf{b} / \mu$. In practice, any natural material is actually formed by a collection of finite-sized atoms and molecules and therefore proper care should be taken in the definition of such 'continuum' and in the way how the fields and constitutive parameters are averaged over several of these basic elements. Nevertheless, the classic definition of Poynting vector has been validated by over a century-long series of experiments on electromagnetic wave propagation and it is well consistent with the continuity of power flow across a boundary between two materials with different constitutive parameters.

A rigorous definition of the Poynting vector gets more challenging when dealing with metamaterials, i.e., artificial materials formed by arrays of sub-wavelength inclusions with exotic electromagnetic properties. As described in Chapter II, one of the goals of the research in metamaterials consists of properly describing these structures as bulk materials, which can be done through homogenization techniques. In fact, it has been shown theoretically (using rigorous homogenization procedures) and also experimentally how negative index metamaterials (NIMs), for which the average power flow bends towards a regular dielectric or vacuum, may be realized in given frequency windows. As predicted in Veselago's work [1], the effective permittivity and permeability of such materials have a negative real part, consistent with the backward flow of $\mathbf{s}$ with respect to the phase velocity. Despite the success of various experiments proving these anomalous properties, the counterintuitive wave interaction of NIMs [1] has raised a series of concerns about the applicability of classic electromagnetic theorems to such values of homogenized parameters, and this debate has recently been extended to the very definition of Poynting vector [23, 24]. In the case of metamaterials, it is evident that it should first be defined a proper averaging procedure for the microscopic fields that filters out their irrelevant higher-order fluctuations around the inclusions [25, 26]. Assuming that the averaged source fields are defined with capital letters in the form $\mathbf{E} = \langle \mathbf{e} \rangle$ and $\mathbf{B} = \langle \mathbf{b} \rangle$, it has been argued that the proper definition of averaged Poynting vector in metamaterials should be modified to neglect the artificial magnetic effects on which negative refraction is based, and the creative definition $\mathbf{S} = \mathbf{E} \times \mathbf{B} / \mu_0$ has been put forward [24], independent of the actual value of the effective permeability. Based on this definition of Poynting vector, the very notion of negative refraction has been put into discussion [23, 24]. Since the Poynting vector is inherently based on a (nonlinear) quadratic expression, the relation $\langle \mathbf{e} \times \mathbf{b} \rangle = \langle \mathbf{e} \rangle \times \langle \mathbf{b} \rangle$ is generally incorrect and thus, in general, $\mathbf{E} \times \mathbf{B} / \mu_0$ may not have the same meaning as its microscopic counterpart (this is evident if one considers the interface between such material and a magnetic homogeneous material with $\mu \neq \mu_0$, for which power conservation would not be satisfied if one associates to this expression the meaning of power flux density). Here, based on the theory of Ref. [28], these issues are clarified and it is proven from first-principles considerations that it is indeed possible to put forward a meaningful and self-consistent definition of averaged Poynting vector and other power relations in metamaterials, consistent with those in natural materials.

III.2.2. Poynting Self-Consistently

Here, it is assumed that the time-averaged Poynting vector in media with no magnetism ($\mu = \mu_0$) is defined such that $\mathbf{s}_c = \frac{1}{2} \mathrm{Re}\left\{ \mathbf{e} \times \mathbf{b}^* / \mu_0 \right\}$.

In Ref. [28], it was theoretically proven that in low-loss 2D periodic arrays of inclusions, the spatially averaged microscopic Poynting vector,

$$\mathbf{S} = \frac{1}{A_{\text{cell}}} \int_{\Omega} \mathbf{s}_c \, d^2\mathbf{r}, \tag{3.1}$$

associated with Bloch-periodic time-harmonic fields $e^{i(\mathbf{k}\cdot\mathbf{r}-\omega t)}$, with real valued wave vector **k**, may be *exactly* related to the macroscopic generalized effective permittivity of the homogenized metamaterial by the following relation:

$$\mathbf{S}\cdot\hat{l}=\frac{1}{2}\mathrm{Re}\left\{\left(\mathbf{E}\times\mathbf{B}^{*}/\mu_0\right)\cdot\hat{l}\right\}-\frac{1}{4}\omega\mathbf{E}^{*}\cdot\frac{\partial\overline{\overline{\varepsilon_{\mathrm{eff}}}}}{\partial k_l}\left(\omega,\mathbf{k}\right)\cdot\mathbf{E},\ l=x,y \qquad (3.2)$$

where $\mathbf{E}=\langle\mathbf{e}\rangle$, $\mathbf{B}=\langle\mathbf{b}\rangle$, the effect of the spatial averaging operator $\langle\ \rangle$ is an ideal low pass filter such that $\mathbf{E}=\mathbf{E}_{\mathrm{av}}e^{i\mathbf{k}\cdot\mathbf{r}}$, where $\mathbf{E}_{\mathrm{av}}$ is calculated using Eq. (2.2) (Chapter II Sec. II.2.2.1) and k_l is the l-th component of $\mathbf{k}$. The nonlocal permittivity tensor $\overline{\overline{\varepsilon_{\mathrm{eff}}}}$ is that defined in the previous Chapter and can be calculated using the retrieval algorithm described in Sec. II.2.2.1. Equation (3.2) is written in perfect analogy with the definition of power flux in natural optical crystals with spatially dispersive properties [29], and this is not necessarily surprising as this homogenization procedure may also be applied to natural materials. Even though Ref. [28] considered only the case of Bloch natural modes, it may be proven that the validity of (3.2) extends even to the case in which external sources are embedded in the composite material. Equation (3.2) shows that the proper expression for $\mathbf{S}$ needs to be corrected to include the spatial dispersion in $\overline{\overline{\varepsilon_{\mathrm{eff}}}}$.

After having discussed that the result (3.2) may be applied to arbitrarily excited metamaterials with a general form of spatial dispersion, let us apply it specifically to the case wherein the macroscopic description of the metamaterial may be characterized by effective local relative permittivity $\varepsilon_{\mathrm{eff}}=\overline{\overline{\varepsilon_{\mathrm{eff}}}}\left(\omega,\mathbf{k}=0\right)$ and permeability μ_{eff} [Eq. (2.9)]. Moreover, for the sake of simplicity, the discussion is restricted to the case of isotropic media and it is assumed no magneto-electric coupling, i.e. $\overline{\overline{\xi}}=\overline{\overline{\zeta}}=0$, as in NIMs. In such a scenario, the nonlocal permittivity tensor described in the previous Chapter (Eq. (2.7)) reduces to:

$$\frac{\overline{\overline{\varepsilon_{\text{eff}}}}}{\varepsilon_0}(\omega,\mathbf{k}) = \varepsilon_{\text{eff}}\overline{\overline{\mathbf{I}}} + \left(\mu_{\text{eff}}^{-1}-1\right)\frac{c^2}{\omega^2}\mathbf{k}\times\overline{\overline{\mathbf{I}}}\times\mathbf{k}. \qquad (3.3)^{1}$$

Substituting the above formula into (3.2), the classic textbook formula for time-averaged Poynting vector in magneto-dielectric media [28] is readily recuperated:

$$\mathbf{S} = \frac{1}{2}\text{Re}\{\mathbf{E}\times\mathbf{H}^*\}, \qquad (3.4)$$

where $\mathbf{H} \equiv \mu_0^{-1}\mu_{\text{eff}}^{-1}\mathbf{B}$, ensuring that the only meaningful definition of power flux vector density in metamaterials coincides with the well established one for natural materials. This expression applies equally well to negative values of μ_{eff}, i.e., it holds for NIMs.

In order to highlight the importance of the findings described above, let us consider an arbitrary surface Σ that may intersect one or more different materials and may enclose sources of radiation, as illustrated in Fig. 3.1.

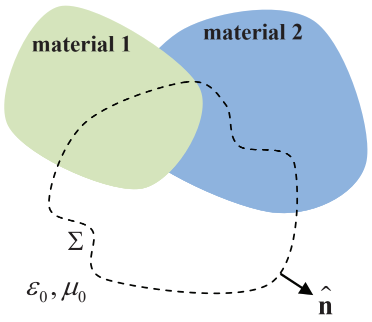

Fig. 3.1. A closed surface Σ encloses a non-uniform region.

The power flow towards the region outside Σ can be unambiguously calculated through the microscopic Poynting vector as $P = \int_{\Sigma} \hat{\mathbf{n}}.\mathbf{s}_c \, ds$. Obviously, because of the strong

---

[1] Even though Eqs. (2.7) and (3.3) appear to be different in this scenario wherein the 2D metamaterial is characterized by a nearly local isotropic response and the magneto-electric tensors are negligible, it may be easily shown that in such a scenario $\varepsilon_{\text{eff},xx} = \varepsilon_{\text{eff},yy}$ whereas $\varepsilon_{\text{eff},xy} = \varepsilon_{\text{eff},yx} = 0$, where $\varepsilon_{\text{eff},ij} = \hat{\mathbf{u}}_i \cdot \overline{\overline{\varepsilon_{\text{eff}}}}(\omega,\mathbf{k}=0)\cdot\hat{\mathbf{u}}_j$, and $\overline{\overline{\varepsilon_{\text{eff}}}}(\omega,\mathbf{k}=0) = \overline{\overline{\varepsilon_{\text{r}}}}$. Therefore, in such a scenario the term $\overline{\overline{\varepsilon_{\text{r}}}}$ in Eq. (2.7) is precisely equal to the term $\varepsilon_{\text{eff}}\overline{\overline{\mathbf{I}}}$ in Eq. (3.3). Similarly, the term $\mathbf{k}\times\left(\overline{\overline{\mu_{\text{r}}}}^{-1}-\overline{\overline{\mathbf{I}}}\right)\times\mathbf{k}$ in Eq. (2.7) is the same as $\left(\mu_{\text{eff}}^{-1}-1\right)\mathbf{k}\times\overline{\overline{\mathbf{I}}}\times\mathbf{k}$ in Eq. (3.3).

fluctuations of the microscopic fields near the portions of Σ that intersect regions with matter, the use of $\mathbf{e}$ and $\mathbf{b}$ to calculate the power flow is impractical. However, provided the wavelength of radiation is much larger than the characteristic granularity of the materials, it is possible to average out the fluctuations of the microscopic fields and use effective medium theory. Indeed, assuming that Σ encloses a macroscopic region, it can be written:

$$P = \int_{\Sigma} \hat{\mathbf{n}}.\mathbf{s}_c \; ds \approx \int_{\Sigma} \hat{\mathbf{n}}.\mathbf{S} \; ds \,, \tag{3.5}$$

where $\mathbf{S}$ is the spatially averaged Poynting vector, which, as discussed before, in case of local materials may be written in terms of the average fields and effective parameters as in Eq. (3.4). It follows that $\mathbf{S}$ can be really regarded as an averaged flux of electromagnetic power, and the power flow through the generic surface Σ remains the same, independent of one using the microscopic or the macroscopic fields. Actually, this property is true even if Σ is not a closed surface, because the averaging operator $\langle \; \rangle$ establishes an intrinsically local relation between macroscopic and microscopic fields.

From the previous discussion it should also be clear that in order for the Poynting vector to be really regarded as a flux of electromagnetic energy within an effective medium description, then $\mathbf{S}$ needs to be defined self-consistently as in Eq. (3.4) for every material, because any acceptable definition of a macroscopic Poynting vector is constrained to satisfy Eq. (3.5). In particular, the definition of macroscopic Poynting vector in a given material cannot be made independent of the definition of the (macroscopic) Poynting vector in vacuum, and it certainly cannot be simultaneously compatible with different forms, such as $\mathbf{D} \times \mathbf{B}$, $\mathbf{E} \times \mathbf{H}$, etc. [23].

III.2.3. Energy Relations

Here, within this framework, other spatially averaged energy quantities of interest (average stored energy and heating rate) are considered.

The expression for the averaged stored energy:

$$W_{\text{av}} = \frac{1}{4A_{\text{cell}}} \int_{\Omega} \frac{|\mathbf{b}|^2}{\mu_0} d^2\mathbf{r} + \frac{1}{4V_{\text{cell}}} \int_{\Omega} \frac{\partial}{\partial \omega}\left(\omega\varepsilon\right)|\mathbf{e}|^2 \, d^2\mathbf{r}, \tag{3.6}$$

may be related to the macroscopic effective parameters in analogy with Eq. (3.2) as [28]:

$$W_{\text{av}} = \frac{1}{4}\frac{|\mathbf{B}|^2}{\mu_0} + \frac{1}{4}\mathbf{E}^* \cdot \frac{\partial}{\partial \omega}\left(\omega\overline{\overline{\varepsilon_{\text{eff}}}}\right) \cdot \mathbf{E}. \tag{3.7}$$

Equations. (3.6) and (3.7) are strictly valid for vanishingly small loss and time-harmonic Bloch microscopic fields. In the special case of local metamaterials, for which Eq. (3.3) applies, the stored energy expression becomes:

$$W_{\text{av}} = \frac{1}{4}\frac{\partial}{\partial \omega}\left(\omega\mu_0\mu_{\text{eff}}\right)|\mathbf{H}|^2 + \frac{1}{4}\frac{\partial}{\partial \omega}\left(\omega\varepsilon_0\varepsilon_{\text{eff}}\right)|\mathbf{E}|^2, \tag{3.8}$$

which is consistent with classic textbook formulas for magneto-electric dispersive media [25, 26], but extended here to local metamaterials and effective constitutive parameters.

Finally, analogous considerations can be applied to the heating rate in metamaterials. The spatially averaged heating rate is analogously defined as:

$$q_{\text{av}} = \frac{1}{A_{\text{cell}}} \int_{\Omega} \frac{\omega}{2} \varepsilon''(\mathbf{r})|\mathbf{e}(\mathbf{r})|^2 \, d^3\mathbf{r}, \tag{3.9}$$

which may be written in terms of the generalized permittivity tensor as [28]:

$$q_{\text{av}} = \frac{1}{2}\text{Re}\left\{-i\omega\mathbf{E}^* \cdot \overline{\overline{\varepsilon_{\text{eff}}}}\left(\omega,\mathbf{k}\right) \cdot \mathbf{E}\right\}. \tag{3.10}$$

The above formula holds exactly only in the case of real-valued wave vector $\mathbf{k}$, which, due to the presence of loss, can only be obtained if the metamaterial is excited by an external current distribution $\mathbf{j}_e = \mathbf{j}_{e,\text{av}} e^{i\mathbf{k}.\mathbf{r}}$ (evidently, they are not eigenmodes of a lossy array). For a local material, Eq. (3.10) simplifies into:

$$q_{\text{av}} = \frac{1}{2}\omega\varepsilon_0\varepsilon''_{\text{eff}}\left(\omega\right)\left|\mathbf{E}\right|^2 + \frac{1}{2}\omega\mu_0\mu''_{\text{eff}}\left(\omega\right)\left|\mathbf{H}\right|^2, \tag{3.11}$$

again extending to the textbook formulas for natural materials to local metamaterials.

III.2.4. Numerical Results

In Chapter II (Sec. II.3.1.3), it was briefly discussed that the effective response of the Zero-Index metamaterial may be characterized by a regime where both the effective permeability and permittivity are simultaneously negative (Fig. 2.8). Based on this finding, the Zero-Index metamaterial may be regarded as a NIM , and therefore it will be used in this section in order to numerically test the results derived in the previous sections. The high-index cylinders have relative permittivity $\varepsilon_r \approx 50.47$ and normalized radius $R/a = 0.435$, whereas the host plasmonic medium follows the Drude dispersion model with $\omega_p a/c = 1.0$. To begin with the host is assumed to be lossless, i.e. $\Gamma/\omega_p = 0$.

Figure 3.2 shows the local effective parameters $\varepsilon_{\text{eff},yy} = \hat{\mathbf{u}}_y \cdot \overline{\overline{\varepsilon_{\text{eff}}}}\left(\omega, \mathbf{k} = 0\right) \cdot \hat{\mathbf{u}}_y / \varepsilon_0$ and $\mu_{\text{eff}}(\omega)$, extracted using the nonlocal FDFD approach based on the retrieval algorithm described in Sec. II.2.2.1 and Eq. (2.9), respectively. As seen, both permittivity and permeability are simultaneously negative for a range of frequencies $0.85 < \omega a/c < 1$. It should be mentioned that an interesting characteristic of this metamaterial is that it can be tuned in order to provide not only a negative index of refraction but also a good matching with free-space. More specifically, the metamaterial parameters were tuned to ensure that $\varepsilon_{\text{eff}}(\omega) \approx \mu_{\text{eff}}(\omega) \approx -1$ at $\omega a/c = 0.88$. This topic will be further discussed in this Chapter, in a different context. The solid lines represent the effective parameters predicted by the Clausius-Mossotti mixing formulas [25, 26], and consistent with the results obtained in the previous chapter, the obtained curves agree fairly well with the data extracted using the FDFD method (dashed), confirming that a local description of such NIM is accurate.

In order to characterize the Poynting vector in the zero-index metamaterial, the wave vector was fixed at each frequency ω so that $k_x = \omega / c\sqrt{|\varepsilon_{\text{eff}}\mu_{\text{eff}}|}$, as reported in the inset of Fig. 3.2a. The structure is excited by an external current density distribution $\mathbf{j}_e = j_e \hat{\mathbf{u}}_y e^{+ik_x x}$, which effectively excites the natural Bloch mode of this array, and the corresponding microscopic fields are determined numerically [Eqs. (2.14) and (2.16)]. The macroscopic averaged electric and induction fields are then calculated as described in the previous chapter (Sec. II.2.2.1).

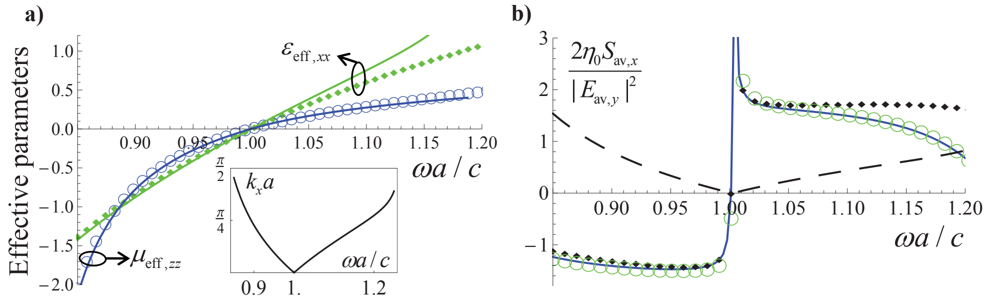

Fig. 3.2. Effective permittivity ε_{eff} (green curves) and permeability μ_{eff} (blue curves) versus normalized frequency $\omega a / c$. The discrete symbols correspond to nonlocal homogenization values and the solid lines are obtained using Clausius-Mossotti formulas. The inset shows the wave vector k_x as a function of frequency. (b) x-component of the Poynting vector calculated using: (i) Averaged microscopic Poynting vector (solid blue) [Eq. 3.1]; (ii) Nonlocal homogenization model (circles) [Eq. (3.3)]; (iii) Local effective parameters (diamonds) [Eq. (3.4)]; (iv) Results based on the definition of Poynting vector of Ref. [24] (dashed)..

Figure. 3.2b shows the x-component of the Poynting vector calculated using: (i) the spatial average of its exact microscopic definition $\mathbf{s}$ [Eq. (3.1)] (solid blue line); (ii) the macroscopic (averaged) fields and generalized permittivity tensor [Eq. (3.2)] (discrete circles); (iii) the local effective parameters [Eq. (3.4)] (discrete diamonds); (iv) the incorrect definition of Poynting vector $\mathbf{S} = \mathbf{E} \times \mathbf{B} / \mu_0$ proposed in [24] (dashed curve).

Consistent with the theory of Ref. [28], the results obtained with microscopic and macroscopic (averaged) fields are coincident. Even the results obtained with a local model, using the standard Poynting vector definition (3.4), follow very closely the exact curves, also confirming the effective response of this metamaterial is nearly local. In particular, it is seen that all three curves indeed flip the sign of power flow crossing the frequency ω_p, ensuring that for negative index propagation ($\omega < \omega_p$) power univocally flows backward. Finally, the curve obtained assuming the wrong definition in [24] yields a completely different response, since it neglects the artificial magnetism introduced by high-permittivity cylinders, and it cannot be interpreted as an average power flux density. Its value is always positive for $k_x > 0$, incorrectly implying that no negative refraction and backward wave propagation could be possible in such metamaterial [24].

The theory described above establishes that Eq. (3.2) yields *exactly* the same result as the spatial average of $\mathbf{s}$ in the limit of vanishing loss, ensuring that indeed Eq. (3.2) represents the correct macroscopic definition of Poynting vector in an arbitrary metamaterial. In addition, it was proved that Eq. (3.4) is the correct definition for local metamaterials, as in the present example.

Next, the numerical discussion is extended to the energy relations described in Sec. III.2.3., namely the average stored energy and heating rate. Figure 3.3a shows the stored energy W_{av} in the metamaterial sample of Fig. 3.2, comparing the results based on Eqs. (3.6), (3.7) and (3.8), in analogy with Fig. 3.2b. It is seen that the exact averaged stored energy (3.6) (solid blue line), coincides with the stored energy computed from nonlocal effective parameters (3.7) (discrete circles), in agreement with [28]. Moreover, the results obtained from local effective parameters (3.8) (discrete diamonds) follow reasonably well the two curves, again confirming that the metamaterial response is local.

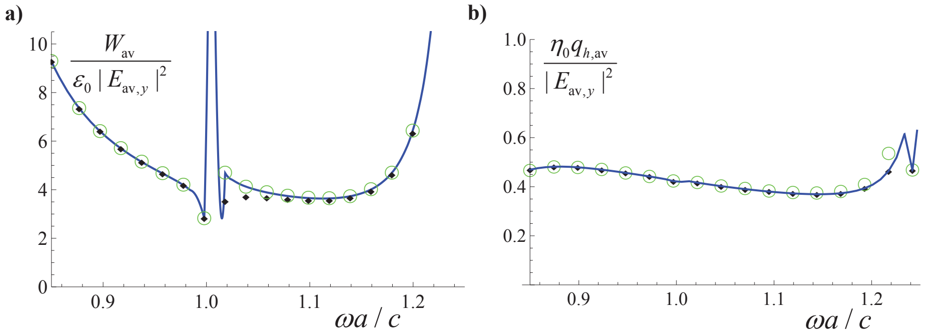

Fig. 3.3. (a) Stored energy calculated using: (i) Averaged microscopic stored energy (solid blue) [Eq. (3.6)]; (ii) Nonlocal homogenization model (circles) [Eq. (3.7)]; (iii) Local effective parameters (diamonds) [Eq. (3.8)]. (b) Heating rate calculated using: (i) Averaged microscopic heating rate (solid blue) [Eq. (3.9)]; (ii) Nonlocal homogenization model (circles) [Eq. (3.10)]; (iii) Local effective parameters (diamonds) [Eq. (3.11)].

Figure 3.3b shows the comparison among the three definitions of heating rate described above (3.9)-(3.11) for $\Gamma/\omega_p = 0.1$ and cylinder permittivity $\varepsilon_{\mathrm{r}} = 50.47 + 0.1i$ (for simplicity, frequency dispersion is ignored). The results obtained using Eq. (3.9) (solid blue line) and Eq. (3.10) (discrete circles) are virtually coincident, despite the presence of small loss. Similarly, the results computed using the local model (3.11) (discrete diamonds) agree extremely well.

As is well known, effects of loss are unavoidable in realistic metamaterials, and thus it is interesting to study how the energy flux vectors compare in a more realistic scenario, as in Fig. 3.4a and 3.4b, where we consider $\Gamma/\omega_p = 0.1$ and $\Gamma/\omega_p = 2.0$, respectively. Despite the presence of strong loss, the general agreement between Eqs.(3.1), (3.2) and (3.4) remains very good, confirming that even in lossy systems the macroscopic Poynting vector can be self-consistently defined (to a very good approximation) as the averaged microscopic Poynting vector. In fact, it can be theoretically shown that Eqs. (3.1) and (3.2) remain *exactly* equal despite the presence of loss.[2]

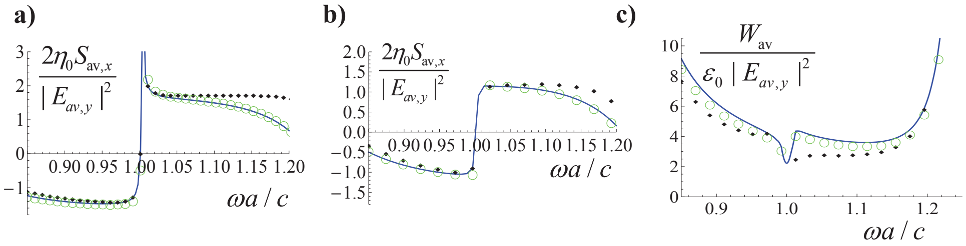

Fig. 3.4. (a,b) Similar to Fig. 3.2b, except that losses are taken into account: (a) $\Gamma / \omega_p = 0.1$, (b) $\Gamma / \omega_p = 2.0$. (c) Similar to Fig. 3.3a, except that losses are taken into account ($\Gamma / \omega_p = 0.5$).

It is also interesting to analyze what happens to the stored energy when the effect of loss is taken into account. In Fig. 3.4c the loss in the metamaterial is such that $\Gamma / \omega_p = 0.5$, and the results obtained using Eqs. (3.6)-(3.7) partially lose their close agreement, but this is not surprising, since the same definition of macroscopic stored energy density loses much of its physical meaning in the presence of losses [29, p.63]. Still, the different curves show good agreement in the limit of low losses.

III.3. Mimicking the Veselago-Pendry Superlens

III.3.1. Introduction

In Sec. III.1 it was briefly mentioned that building on Veselago's work, Pendry suggested that a lossless material slab with $n = -1$ (at a fixed frequency) makes a perfect lens with unlimited resolution. Such extraordinary phenomenon has its roots on two effects: on one hand the propagating plane waves are focused due to negative refraction; on the other hand the evanescent modes are restored due to resonant excitation of guided modes supported by the double-negative medium when $\varepsilon = \mu = -1$. Nevertheless, it soon became evident that this imaging mechanism is strongly sensitive

---

[2] M. G. Silveirinha, (unpublished).

to losses and material dispersion [30-32], besides the numerous practical difficulties related to the realization of double-negative media.

As discussed in the previous chapter (Sec. II.3.1.2), metamaterials based on periodic arrays of plasmonic particles may be used for achieving regimes of simultaneously negative ε and μ [33-35]. Moreover, in the previous Chapter, based on the findings of Ref. [33], it was confirmed using the FDFD nonlocal homogenization method that nanoparticles with negative permittivity can support multiple electric resonances [36] and such resonances can indeed be useful if one wishes to tailor the effective properties of a composite material (particularly the magnetic response in the optical regime). On the other hand, such inherently electrostatic resonances may also be a source of sharp singularities in the effective response ε_{eff} of a composite material, and in practice may imply strong spatial dispersion and also that the frequency range where the response of the effective medium is useful may be quite narrow. As shown in Sec. II.3.1.2, a periodic array of plasmonic cylindrical inclusions may support many high-multipole resonances in the vicinity of the frequency at which the real part of the permittivity of the inclusion satisfies $\varepsilon_r'(\omega) = -1$, and some of these resonances may be associated with a regime where the structure behaves as a DNG material. However, the frequency window where the effective permittivity ε_{eff} and effective permeability μ_{eff} are simultaneously negative is very narrow due to the sensitive behavior of ε_{eff} in the DNG regime. In other words, when the inclusions are operated near the plasmonic resonance the characteristic wavelength of a guided mode may be shorter than the lattice constant, and in such case the material cannot be regarded as an effective medium, and thus it cannot be homogenized.

Here, it is shown that by interchanging the roles of the dielectric host material and of the plasmonic inclusions (e.g., zero index metamaterial (Sec. II.3.1.3)), it may be possible to circumvent the above mentioned drawbacks and achieve a broadband DNG regime, where the response of the effective medium is to a good approximation local (already proven in this Chapter) and in part insensitive to loss effects. Moreover, it is shown that in case of sufficiently low loss such configuration enables mimicking to some extent the Veselago-Pendry's lens and imaging with super-resolution.

III.3.2. Limitations of DNG Metamaterials Based on Plasmonic-Type Inclusions

In order to further illustrate the inherent bandwidth design based on plasmonic-type inclusions, the effective parameters (ε_{eff} and μ_{eff}) are calculated for the metamaterial configuration described in Sec. II.3.1.2, i.e., a configuration formed by an array of plasmonic inclusions embedded in air and arranged in a square lattice with lattice constant a. It is assumed that the cylinders have a normalized radius $R/a = 0.44$, the plasma frequency is such that $\omega_p a/c = 1.0$ and the collision frequency is $\Gamma/\omega_p = 0.001$. The effective parameters, $\varepsilon_{\text{eff}} = \varepsilon_{\text{eff}}\left(\omega, \mathbf{k} = 0\right)$ and μ_{eff} (Eq. (2.9)) are computed using the FDFD formalism described in the previous chapter and are depicted in Fig. 3.5a as a function of the normalized frequency ω/ω_p. As shown, the frequency window where both ε_{eff} and μ_{eff} are simultaneously negative is extremely narrow $(0.625 < \omega/\omega_p < 0.626)$. It should be recalled that the computed results are qualitatively analogous to those reported in [33] for a similar geometrical structure. The inset of Fig. 3.5a illustrates the irregular behavior of the effective permittivity ε_{eff} in the vicinity of $\omega = 0.7\omega_p$ (where $\varepsilon_{\text{r}}' \approx -1$), caused by the excitation of multiple quasi-static resonances. In order to determine how the effective response of this configuration is affected by losses, in Fig 3.5b the effective permeability $\mu_{\text{eff}} = \mu_{\text{eff}}' + i\mu_{\text{eff}}''$ is depicted at the magnetic resonance for different values of absorption, i.e., for different values of Γ.

It is clear from Fig 3.5b that even for extremely low values of absorption ($\Gamma/\omega_p = 5\times10^{-4}$, blue curves) the magnetic resonance is tremendously damped and it almost disappears when a slightly higher value of loss is considered ($\Gamma/\omega_p = 1\times10^{-3}$, green curves), confirming that the DNG response of this configuration is not only extremely narrowband but also very sensitive to the effect of loss.

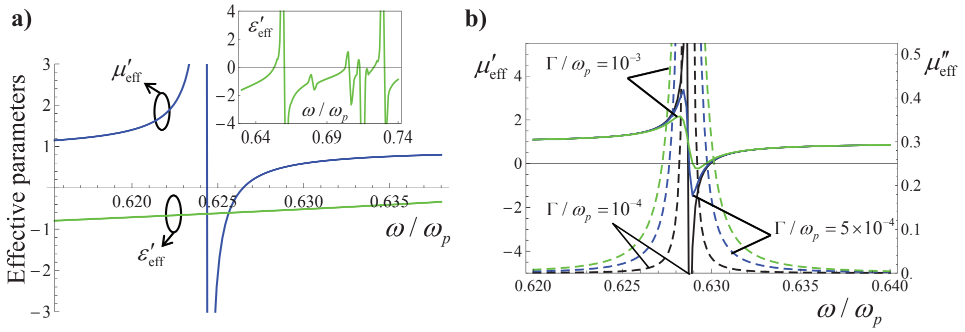

Fig. 3.5. (a) Real parts of the effective permittivity $\varepsilon_{\rm eff} = \varepsilon'_{\rm eff} + i\varepsilon''_{\rm eff}$ (green curves) and permeability $\mu_{\rm eff} = \mu'_{\rm eff} + i\mu''_{\rm eff}$ (blue curves) as a function of the normalized frequency ω/ω_p ($\Gamma/\omega_p = 10^{-4}$). The inset shows the real part of the effective permittivity ($\Gamma/\omega_p = 10^{-4}$) in the vicinity of the plasmonic resonance of the inclusions ($\omega/\omega_p = 0.7$). (b) Real and imaginary parts of the effective permeability $\mu_{\rm eff} = \mu'_{\rm eff} + i\mu''_{\rm eff}$ as a function of the normalized frequency ω/ω_p, for different values of the damping frequency: $\Gamma/\omega_p = 10^{-4}$ (black curves), $\Gamma/\omega_p = 5\times10^{-4}$ (blue curves) and $\Gamma/\omega_p = 10^{-3}$ (green curves). The solid lines correspond to the real part of $\mu_{\rm eff}$ while the dashed lines represent the imaginary part.

III.3.3. Broadband Matched DNG metamaterials

The example of the previous section illustrates the inherent bandwidth restrictions and high loss sensitivity of typical metamaterial designs based on materials with a plasmonic-type response. Surprisingly, as described next, there may be a simple strategy to overcome these apparently fundamental limitations and achieve a broadband low loss response. Notably, this may involve simply interchanging the roles of the inclusions and of the host material. In order that DNG materials can be used effectively as functional elements of novel electromagnetic devices it is essential that they can be efficiently coupled to conventional dielectrics. In practice, this requires that the impedance of the DNG material, η, is relatively close to the impedance of vacuum

$\eta_0 = \sqrt{\mu_0 / \varepsilon_0}$, or equivalently that $\mu \sim \varepsilon$, being ε and μ the relative permittivity and permeability of the DNG material, respectively. Hence, in an ideal scenario it would be desirable to have matched operation, $\mu = \varepsilon$, over a broad frequency region.

In Chapter II, based on the findings of Ref. [37], it was confirmed that embedding dielectric particles with suitable size and permittivity in a host background with near-zero permittivity, permits achieving a matched operation in the regime where the effective parameters are simultaneous near zero $\varepsilon_{\text{eff}}(\omega_p) \approx \mu_{\text{eff}}(\omega_p) \approx 0$ (Figs. 2.8 and 3.2a). The analysis of Ref. [37], was however focused in the regime $\varepsilon_{\text{eff}} \approx \mu_{\text{eff}} \approx 0$ (for geometries that are intrinsically two-dimensional), and the possibility of having matched operation over a broad frequency band or superlensing ($\varepsilon_{\text{eff}} \approx \mu_{\text{eff}} \approx -1$) was not investigated. However, it is evident that causality and passivity restrictions imply that for small absorption both $\varepsilon_{\text{eff}}(\omega)$ and $\mu_{\text{eff}}(\omega)$ must increase with frequency [26], and hence if $\varepsilon_{\text{eff}} \approx \mu_{\text{eff}} \approx 0$ at a given frequency ω_p, then for $\omega < \omega_p$ the effective permittivity and permeability are simultaneously negative. Next, based on these ideas it is demonstrated that the zero index metamaterial enables, indeed, a broadband DNG regime. Moreover, it is shown that the results derived for the 2D zero index metamaterial can be readily extended to a 3D configuration formed by high index dielectric spheres instead of cylinders. It is shown that contrarily to the 2D configuration, the 3D metamaterial permits achieving a broadband matched DNG response for two polarizations rather than for a single polarization, as in the 2D model.

III.3.3.1 2D Configuration

In Sec. III.2.4 it was shortly discussed the possibility of tuning the parameters of the zero index metamaterial in order to obtain a matched DNG regime and, more interestingly, to obtain an effective index of refraction $n_{\text{eff}} \approx -1$ at a given frequency of operation. As already mentioned, the configuration used to numerically analyze the Poynting vector was tuned in order to assure a matched DNG operation and that $\varepsilon_{\text{eff}}(\omega) \approx \mu_{\text{eff}}(\omega) \approx -1$ at $\omega a / c = 0.88$ i.e., $n_{\text{eff}}(\omega) \approx -1\big|_{\omega a/c=0.88}$, (Fig. 3.2a), and the same results (effective parameters as a function of frequency) are depicted in Fig. 3.6a in a narrower frequency band, to clearly show the broadband matched DNG regime achieved with this metamaterial. In fact, using the Clausius-Mossotti formulas it is possible to fine tune the geometry of the metamaterial in such a way that $\varepsilon_{\text{eff}}(\omega) \approx \mu_{\text{eff}}(\omega)$ in the DNG regime, ensuring a good matching with free-space in a wide frequency window. Notably, at $\omega a / c = 0.88$ the response of a planar metamaterial slab may mimic to some extent the Veselago-Pendry's lens [1, 2] as it will be demonstrated ahead. It is also seen in Fig. 3.6a that $\varepsilon_{\text{eff}}(\omega)$ and $\mu_{\text{eff}}(\omega)$ are simultaneously negative for $0.79 < \omega / \omega_p < 1.0$, being the bandwidth of the DNG regime several orders of magnitude wider than what is achievable when the roles of the inclusions and host are interchanged, as discussed in Sec. III.3.2 (e.g. in one of the examples of Sec. III.3.2 the DNG bandwidth was less than 0.2 %).

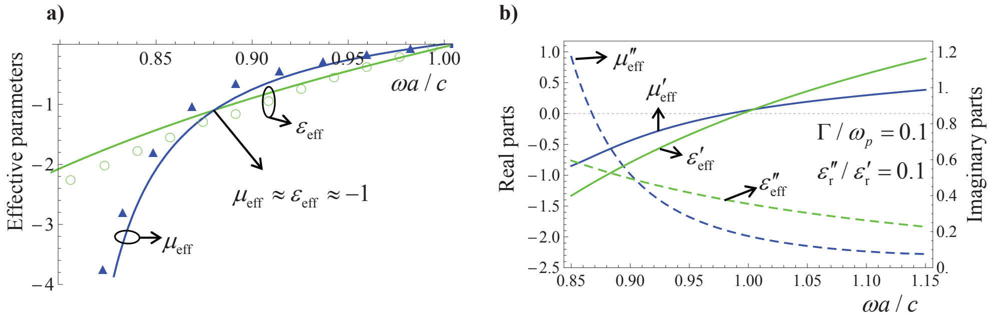

Fig. 3.6. (a) Same as Fig. 3.2a but the effective parameters are depicted in a narrower frequency band. (b) Real and imaginary parts of the effective permittivity $\varepsilon_{\text{eff}} = \varepsilon'_{\text{eff}} + i\varepsilon''_{\text{eff}}$ (green curves) and permeability $\mu_{\text{eff}} = \mu'_{\text{eff}} + i\mu''_{\text{eff}}$ (blue curves) as a function of the normalized frequency ω / ω_p, for the same configuration as in (a), except that losses are taken into account: $\Gamma / \omega_p = 0.1$ and $\varepsilon''_r / \varepsilon'_r = 0.1$. The solid lines correspond to the real parts of ε_{eff} and μ_{eff} while the dashed lines represent the imaginary parts.

It is interesting to analyze the robustness with respect to loss of the proposed configuration by calculating the effective parameters $\varepsilon_{\text{eff}} = \varepsilon'_{\text{eff}} + i\varepsilon''_{\text{eff}}$ and

$\mu_{\text{eff}} = \mu'_{\text{eff}} + i\mu''_{\text{eff}}$ using the FDFD numerical method described in Chapter II, when losses are taken into account. Figure 3.6b reports the combined effect of loss in the plasmonic host and loss in the dielectric inclusions ($\varepsilon_{\text{r}} = \varepsilon'_{\text{r}} + i\varepsilon''_{\text{r}}$), and it is seen that the two mechanisms of loss add up resulting in moderate loss in both the effective permittivity and permeability. It can also be seen in Fig. 3.6b that for $\varepsilon''_{\text{r}} / \varepsilon'_{\text{r}} = 0.1$ and $\Gamma / \omega_p = 0.1$ it is still possible to achieve a broadband DNG regime of operation, however, as expected, it is not possible to provide that $\varepsilon_{\text{eff}}(\omega) \approx \mu_{\text{eff}}(\omega) \approx -1$. This contrasts sharply with the response of the complementary structure described in Sec. III.3.2, which is strongly affected by loss, and indicates that the present configuration is far more robust in this regard. In Ref. [J.3] a more extensive study was performed regarding the effect of loss in this metamaterial and it was concluded that interestingly, the loss in the host medium affects mainly the imaginary part of ε_{eff} whereas the loss in the dielectric inclusions affects mainly the imaginary part of μ_{eff} (see [J.3] for further details).

In Fig. 3.7a the dispersion diagram obtained by solving $k^2 = (\omega / c)^2 \varepsilon_{\text{eff}} \mu_{\text{eff}}$ is depicted around the plasma frequency, for the case $\Gamma / \omega_p = 0$. The blue circles were obtained using the FDFD nonlocal homogenization method (Chapter II) whereas the green diamonds were calculated using the Clausius-Mossotti theory [37]. The band structure is formed by two nearly twin bands that have reflection symmetry with respect to $\omega = \omega_p$, and are associated with transverse electromagnetic waves. The two bands touch at the $k = 0$ point, because the condition $\varepsilon_{\text{eff}} \approx \mu_{\text{eff}} \approx 0$ excludes the possibility of a photonic band-gap and ensures a continuous linear dispersion close to the plasma frequency. In Fig. 3.7a the lower band corresponds to the frequency window where the material behaves as a left-handed material, which in this case happens for $0.81 < \omega / \omega_p < 1.0$. The negative slope of this band shows that the group velocity

$v_g = \dfrac{\partial \omega}{\partial k}$ is negative for $0.81 < \omega / \omega_p < 1.0$, confirming the emergence of backward wave propagation in this regime. On the other hand, the upper band corresponds to a frequency window where both $\varepsilon_{\text{eff}}(\omega)$ and $\mu_{\text{eff}}(\omega)$ are positive (right-handed material), which happens for $1.0 < \omega / \omega_p < 1.23$.

Besides the two bands associated with the transverse modes, there are also two flat bands at $\omega = \omega_p$ (not shown in Fig. 3.7a) which are associated with longitudinal modes. The emergence of such "bulk" Plasmon modes is made possible by the condition $\varepsilon_{\text{eff}} \approx \mu_{\text{eff}} \approx 0$. The electric plasmon modes are such that $\mathbf{E}$ is parallel to the wave vector, and $\mathbf{H} = 0$, and occur when $\varepsilon_{\text{eff}} = 0$. Similarly, the magnetic plasmon modes are such that $\mathbf{H}$ is parallel to the wave vector, and $\mathbf{E} = 0$, and occur when $\mu_{\text{eff}} = 0$.

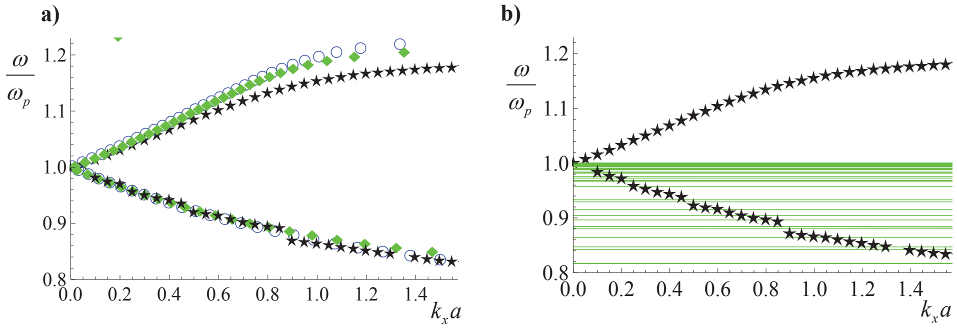

Fig. 3.7. (a) Band structure (only the bands associated with transverse electromagnetic waves are shown) calculated from: FDFD nonlocal homogeniztion method (blue circles); Clausius-Mossotti formula (green diamonds); plane wave method (black stars). (b) The complete band structure calculated using the plane wave method, showing also the dispersionless bands associated with the longitudinal modes (the dispersion of the transverse modes is plotted with black-stars so that it can be distinguished from the dispersion of the longitudinal modes).

To further validate the extracted effective parameters, the exact band structure of the periodic medium was calculated using the plane wave method [38]. Since the host material is dispersive the plane wave method must be implemented as described in Refs. [39-42]. To ensure the convergence of the plane wave method the (in-plane) electric field was expanded into 2148 plane waves. The computed results (along a segment of the Brillouin zone with $\mathbf{k}=\left(k_x,0\right)$) are depicted in Fig 3.7b. This panel shows that the band structure is formed by a very large number of nearly dispersionless (flat) bands with accumulation point at $\omega=\omega_p$. Such bands correspond to the longitudinal plasmon modes discussed previously. For an ideal continuous medium they should all be concentrated at $\omega=\omega_p$, but due to the granularity of the structure this is not strictly observed in the metamaterial implementation as they become more scattered. It is worth noting that there is an infinite number of flat bands because due to the periodicity of the structure, the plasmon band is folded into many branches.

Besides the dispersionless bands, it is possible to identify in Fig 3.7b two nearly twin bands (black stars in Fig 3.7b, also depicted in Fig 3.7a), whose dispersion matches well the dispersion of the transverse electromagnetic waves computed with homogenization theory (Fig 3.7a). Therefore, the band structure calculations support the effective medium theory.

III.3.3.2 3D Configuration

The ideas derived in the previous section can be readily generalized to the three-dimensional case. To illustrate this, let us consider an array of spheres with permittivity ε_r, embedded in a near-zero permittivity host, and arranged in a cubic lattice with lattice constant a (inset of Fig. 3.8). It has been shown in previous works that arrays of magneto-dielectric spheres standing in air enable a DNG response [6], however the difference in the proposed design is that the spheres have no intrinsic magnetic response and are embedded in a plasmonic material.

It was shown recently with full-wave homogenization simulations that the metamaterial response can be accurately modeled using the Lewin’s formulas when the inclusions are embedded in a low permittivity host [43]. For the case of inclusions with trivial permeability, the Lewin's formulas read [44]:

$$\varepsilon_{\mathrm{L}} = \varepsilon_{\mathrm{h}}\left(1+\frac{1}{a^3\alpha_{\mathrm{e}}^{-1}-1/3}\right), \qquad \mu_{\mathrm{L}} = 1+\frac{1}{a^3\alpha_{\mathrm{m}}^{-1}-1/3}, \tag{3.12}$$

where

$$\alpha_{\mathrm{e}}^{-1} = \frac{1}{4\pi R^3}\frac{F(\theta)+2\varepsilon_{\mathrm{h}}/\varepsilon_{\mathrm{r}}}{F(\theta)-\varepsilon_{\mathrm{h}}/\varepsilon_{\mathrm{r}}}, \qquad \alpha_{\mathrm{m}}^{-1} = \frac{1}{4\pi R^3}\frac{F(\theta)+2}{F(\theta)-1}. \tag{3.13}$$

with $F(\theta)=\dfrac{2(\sin\theta-\theta\cos\theta)}{(\theta^2-1)\sin\theta+\theta\cos\theta}$ and $\theta=(\omega R/c)\sqrt{\varepsilon_{\mathrm{r}}}$.

To investigate the potentials of this fully three-dimensional (3D) configuration, it is considered first that the plasma frequency is such that $\omega_p a/c=1.0$ and that $\Gamma/\omega_p=0$ (lossless case). The normalized radius of the spheres is $R/a=0.482$ and the dielectric permittivity $\varepsilon_{\mathrm{r}}\approx 58.4$. These parameters ensure a matched DNG operation $\varepsilon_{\mathrm{eff}}(\omega)\approx\mu_{\mathrm{eff}}(\omega)$. The effective parameters calculated with Lewin's theory [Eq. 3.12] are depicted in Fig. 3.8, showing a very wideband DNG response in the range $0.8<\omega/\omega_p<1.0$ and that $\varepsilon_{\mathrm{eff}}(\omega)\approx\mu_{\mathrm{eff}}(\omega)\approx-1$ at $\omega a/c=0.88$, in qualitative agreement with the results for the 2D configuration. In Ref. [J.3] it was further shown that the robustness with respect to the effect of loss of the 3D model, is qualitatively consistent with that of the 2D configuration described in the previous section.

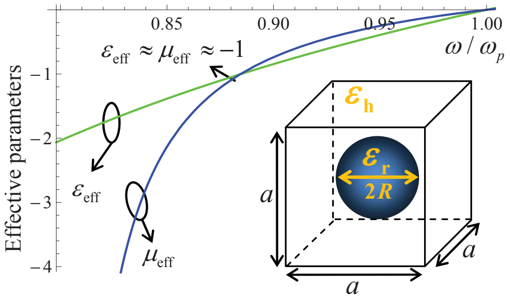

Fig. 3.8. Effective permittivity ε_{eff} (green curves) and permeability μ_{eff} (blue curves) ($\Gamma/\omega_p = 0$) as a function of the normalized frequency ω/ω_p. Both curves were calculated using Lewin's formulas. The geometry of the unit cell is shown in the inset: it consists of a spherical inclusion with normalized radius R/a and permittivity ε_{r} embedded in a host medium with permittivity ε_{h} described by a Drude-type dispersion model.

To conclude this section, possible combinations of realistic materials that may enable realizing the described metamaterial are discussed. At infrared and optical frequencies the role of the plasmonic material may be played (at very specific frequency bands) either by noble metals (e.g. silver in the optical regime) or polar dielectrics (e.g. SiC at the far-IR [45]). However, in these regimes materials with large permittivities are difficult to find, even though that they may be possibly synthesized as metamaterials [46]. Yet, the most promising possibility is perhaps the terahertz regime, where several materials with high index and relatively low loss are readily available (e.g. TiO_2, $MgO{:}LiNbO_3$ [47, 48]). In this regime, either materials with a terahertz polariton resonance such as CsI [49], or semiconductors (e.g. InSb [50]) are characterized by a negative permittivity in some frequency band and thus may be used as the host material. As an example, here, a 3D setup based on TiO_2 (titanium dioxide) spheres embedded in a HgTe (mercurium telluride) host is considered. HgTe is a high mobility (degenerate) semiconductor, whose electrical response may be modeled by a Drude model of the form $\varepsilon(\omega) = \varepsilon_\infty \left(1 - \frac{\omega_p^2}{\omega(\omega + i\Gamma)}\right)$, with plasma frequency $\omega_p = \sqrt{\frac{Ne^2}{m^* \varepsilon_\infty \varepsilon_0}}$ and collision frequency $\Gamma = \frac{e}{m^* \mu_n}$ (within the same level of approximation as that considered in Ref.

[50] for InSb), where $-e$ is the electron charge and ε_0 is the permittivity of vacuum. With the data available in the literature it is possible to estimate that $\varepsilon_\infty = 14.4$ [51], and that the effective electron mass is $m^* = 0.03 m_0$ [52]. On the other hand, the mobility of the electrons μ_n and the electron concentration *N*, depend significantly on the temperature, and can be calculated using the data of Refs. [53, 54]. As a consequence, the plasma and collision frequencies of HgTe are tunable with the temperature. At room temperature, we have $\mu_n \approx 3.5\times 10^3 cm^2 V/s$ and $N \approx 4.3\times 10^{17} cm^{-3}$ and thus the plasma frequency should be about $\omega_p / 2\pi = 9.0[\mathrm{THz}]$ and the collision frequency $\Gamma / 2\pi = 0.27[\mathrm{THz}]$. Unfortunately, this value of ω_p is far too high to enable the combination of HgTe and TiO$_2$ at room temperature in the proposed design. In fact, the permittivity of TiO$_2$ drops sharply after the polaritonic resonance at 5.7[THz] [47]. To circumvent this problem, an operation at lower temperatures is considered to effectively decrease the plasma frequency of HgTe. The permittivity of TiO$_2$ is almost insensitive to temperature [47].

In the first example (Fig. 3.9a), an operation at $T = 30K$ is considered, for which the plasma frequency of HgTe can be estimated as $f_p \approx 1.012 THz$. The permittivity of TiO2 at this frequency is $\varepsilon_{\mathrm{TiO_2}} \approx 95.2 + i2.0$ [47]. Equations (3.12)-(3.13) are used to determine the radius of the spheres in order to ensure $\varepsilon_{\mathrm{eff}} \approx \mu_{\mathrm{eff}} \approx 0$ at $f_p \approx 1.012 THz$, and this yields $R/a = 0.35$ ($a = 47.2 \mu m$). Nevertheless, it should be mentioned that in the example of Fig. 3.9a the radius of the spheres was slightly adjusted to $R/a = 0.33$ in order to have simultaneously $\varepsilon'_{\mathrm{eff}} \approx \mu'_{\mathrm{eff}} \approx -1$ at $f \approx 0.989 THz$ [Fig. 3.9a]. In the same figure the effective parameters are calculated using a time-domain full-wave homogenization simulator [43] are also depicted, confirming the accuracy of the Lewin's formulas [44]. Moreover, the results shown in Fig. 3.9a confirm that the effective response of the 3D configuration formed by realistic materials may provide a fairly matched and fairly broadband DNG response, i.e., the real part of the effective permittivity $\varepsilon'_{\text{eff}}$ (solid green curve) is reasonably identical to the real part of the effective magnetic permeability μ'_{eff} (solid blue curve) in a relatively wide range of frequencies. The bandwidth of DNG operation is about 8%, which should be contrasted with the results of Sec. III.3.3.1. It is relevant to mention that it is possible to achieve a bandwidth of DNG operation of nearly 10% with metamaterials formed by split ring resonators and metallic wires [3], a bandwidth of nearly 20% with metamaterials formed by several layers of fishnets [7], or even larger values using transmission line based metamaterials [8]. Nevertheless, these structures do not provide an isotropic matched response, unlike the zero-index metamaterial, or may require electronic lumped components not available at optics.

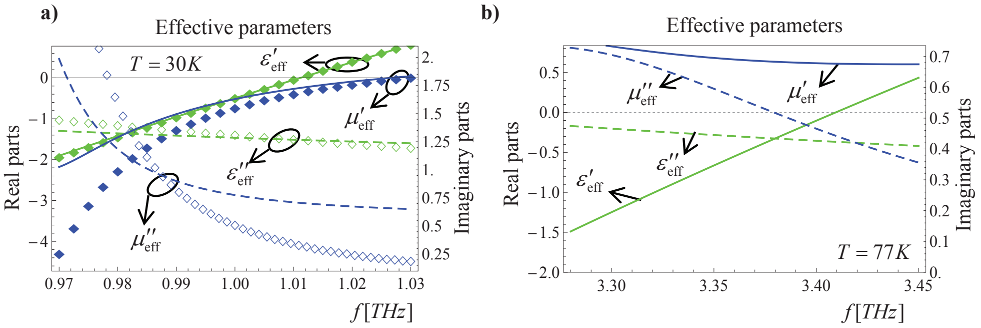

Fig. 3.9. Real and imaginary parts of the effective permittivity $\varepsilon_{\text{eff}} = \varepsilon'_{\text{eff}} + i\varepsilon''_{\text{eff}}$ (green curves) and permeability $\mu_{\text{eff}} = \mu'_{\text{eff}} + i\mu''_{\text{eff}}$ (blue curves) as a function of frequency in the infrared domain, for the scenario wherein the plasmonic host is HgTe and the spherical inclusions are made of TiO_2. (a) T=30K. The radius of the TiO_2 was tuned to ensure that $\varepsilon'_{\text{eff}} \approx \mu'_{\text{eff}} \approx -1$ at $f = 0.989 THz$. The discrete symbols were calculated using the full-wave homogenization simulator [43] and the solid curves were determined using Eqs. (3.12)-(3.13). (b) T=77K.

In Fig. 3.9b the effective response of the 3D configuration is depicted at $T = 77K$. For this temperature, $f_p \approx 3.411 THz$ and $\varepsilon_{\text{TiO}_2} \approx 136.5 + i14.7$. The normalized radius of the spheres is chosen $R/a = 0.276$ ($a = 78.2\mu m$). It can be seen (Fig. 3.9b) that at 77K it is not possible anymore to ensure a DNG response. In fact, the effective magnetic response is strongly damped by the increased loss of TiO_2 (due to operation closer to the resonance of TiO_2) because as mentioned previously, the effective magnetic response is mainly affected by the loss in the dielectric inclusions.

III.3.4. Negative Refraction

To further characterize the potentials of the proposed metamaterials, the refraction of a Gaussian cylindrical beam by a planar metamaterial slab is analyzed using a commercial full-wave electromagnetic simulator [55]. In the first example, the 2D configuration reported in section III.3.3.1 is considered, where the inclusions are high-index cylinders and the magnetic field is parallel to the axes of the cylinders (*z*-direction). The metamaterial slab is finite along the x and y directions, with dimensions $L_x = 17.8a$ and $L_y = 60.4a$, respectively. In the simulation the effect of loss was taken into account by considering that the collision frequency satisfies $\Gamma / \omega_p = 0.05$. The Gaussian beam illuminates the slab along the direction $\theta_i = 33^\circ$. Figure 3.10a shows a snapshot in time of the *z*-component of the magnetic field at $\omega a / c = 0.88$, i.e. at the frequency where according to the results of Figs. 3.2a and 3.6a the effective parameters are $\varepsilon_{\text{eff}} \approx \mu_{\text{eff}} \approx -1$. The negative refraction is evident from Fig. 3.10a, which shows that the beam is bent in an unusual way at the interfaces.

While in the 2D configuration, the DNG response is polarization sensitive and is revealed only when the magnetic field is parallel to the cylindrical inclusions, it is possible to overcome this limitation by considering the 3D metamaterial formed by spherical inclusions. In such a scenario, it is possible to obtain a magnetic response for the two polarizations, i.e., both when the magnetic field is parallel to the *z*-direction (*P*-polarized waves) and, also when the electric field is parallel the *z*-direction (*S*-polarized waves).

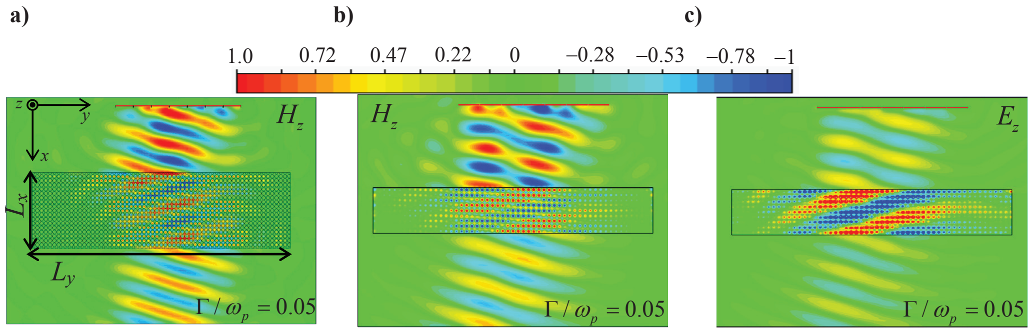

Fig. 3.10. Snapshots of H_z (*P*-polarized waves) and E_z (*S*-polarized waves) when a cylindrical Gaussian beam illuminates ($\theta_i = 33°$) a metamaterial slab: (a) 2D-configuration (cylindrical inclusions) and slab with dimensions $L_x = 17.8a$ and $L_y = 60.4a$ and plasmonic host with collision frequency $\Gamma / \omega_p = 0.05$. (b) and (c) 3D-configuration (spherical inclusions) and a slab with dimensions $L_x = 8.87a$ and $L_y = 54.3a$ and plasmonic host with collision frequency $\Gamma / \omega_p = 0.05$.

To illustrate this, let us consider a metamaterial formed by spherical dielectric inclusions with dimensions $L_x = 8.87a$ and $L_y = 54.3a$ along the x and y directions, respectively. The metamaterial has the same parameters as in Fig. 3.8, except that losses in the host material were also taken into account assuming $\Gamma / \omega_p = 0.05$. Figures 3.10b and 3.10c show a snapshot in time of the *z*-component of the magnetic field (for a *P*-polarized incident wave) and of the electric field (for an *S*-polarized incident wave), respectively, when the metamaterial is illuminated by a cylindrical Gaussian beam. These two snapshots are calculated at $\omega a / c = 0.88$, the frequency at which the effective parameters satisfy $\varepsilon_{\text{eff}} \approx \mu_{\text{eff}} \approx -1$, and at a $z = const.$ plane that cuts the spheres into two equal parts (i.e. at half-height of the unit cell). It can be checked (not shown here) that the results obtained for other cuts are very similar. The results of Figs. 3.10b and Fig. 3.10c confirm a strong negative refraction effect for both polarizations, and that the level of reflections is very low, demonstrating that the metamaterial is well matched with free-space. It should be noticed that the transmission and incident angles satisfy $\theta_t \approx -\theta_i$, consistent with the fact that $n_{\text{eff}} \approx -1$.

In Ref. [J.3] it was also proven that the response of the 2D metamaterial and the negative refraction are little affected by disorder in the structure. Such property stems from the fact that at the plasma frequency (and possibly at nearby frequencies), the electromagnetic fields are unable to sense the granularity of the slab, and an external observer is unable to tell if the inclusions of the metamaterial slab are periodically or randomly arranged [37, 56, 57].

To conclude this section, next the possibility of achieving negative refraction in a 3D-configuration wherein the host medium is HgTe and the spherical inclusions are made of TiO_2 is investigated. The parameters for this configuration are the same as in the example of Fig. 3.9a. The dimensions of the slab are $L_x = 3.84a$ and $L_y = 44.3a$ along the x and y directions, respectively ($a = 47.2\mu m$). Figs. 3.11a and 3.11b show a snapshot in time of the z-component of the electric field (for an S-polarized incident wave) and of the magnetic field (for a P-polarized incident wave), respectively, at $f = 0.989THz$, the frequency at which $\varepsilon'_{\rm eff} \approx \mu'_{\rm eff} \approx -1$. Despite the presence of loss both in the host medium and dielectric, the negative refraction is well evident in both Figs. 3.11a and 3.11b.

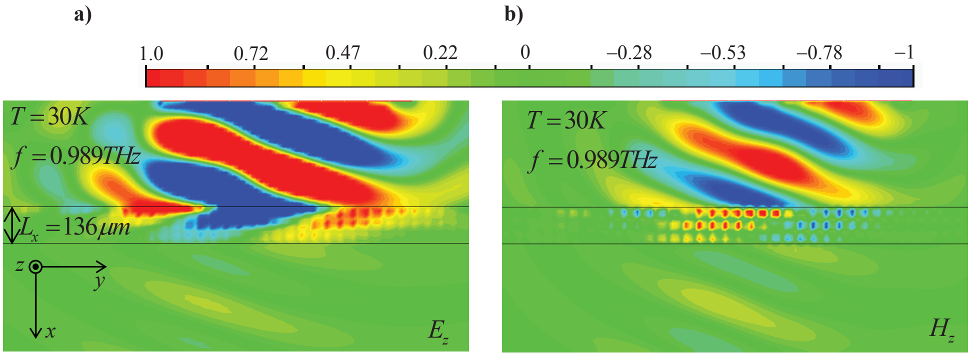

Fig. 3.11. Snapshots of the electromagnetic fields when a Gaussian beam ($\theta_i = 22^{\circ}$) illuminates a metamaterial slab formed by TiO_2 spherical inclusions embedded in a HgTe host ($T = 30K$), with dimensions $L_x = 3.84a$ and $L_y = 44.3a$. (a) P-polarized waves. (b) S-polarized waves.

III.3.5. Superlensing

One of the most exciting potentials of DNG materials is the fact that a metamaterial slab with $\varepsilon_{\rm eff} \approx \mu_{\rm eff} \approx -1$ is able to avoid the effects of diffraction and focus electromagnetic radiation with no resolution limit [2]. Unlike conventional optical lenses which can only process the propagating waves, a DNG slab permits as well restoring the evanescent waves. In the near-field, the condition $\varepsilon_{\text{eff}} \approx \mu_{\text{eff}} \approx -1$ can be relaxed, and there are simpler solutions to achieve superlensing [11-14]. Indeed, to obtain superlensing for a specific polarization, it is sufficient to guarantee that only one of the effective parameters (ε_{eff} or μ_{eff}) is negative, because the magnetic and electric responses are decoupled in the near field.

It is natural to wonder if the metamaterial structures investigated in the previous sections, may mimic to some extent the response of the perfect lens. To this end, first let us consider the configuration where the metamaterial is formed by cylindrical inclusions, and has the same parameters as in Figs. 3.2a and 3.6a. Using a full-wave electromagnetic simulator [55], the transfer function T of a metamaterial slab was determined as a function of the transverse wave number of the impinging wave, k_y. The frequency of operation is $\omega a / c = 0.88$ i.e., the frequency at which the effective parameters of the metamaterial satisfy $\varepsilon_{\text{eff}} \approx \mu_{\text{eff}} \approx -1$. The slab has dimensions $L_x = a$ and it is infinite along the *y*- and *z*- directions, and the effect of loss was taken into account supposing that the collision frequency of the plasmonic host is such that $\Gamma / \omega_p = 0.01$. The obtained results are depicted in Fig. 3.12 (blue solid curve), and are compared with the transfer function of an ideal Pendry's lens (black dashed curve) with $\varepsilon = \mu = -1$ ($T = e^{\gamma_0 L_x}$, with $\gamma_0 = \sqrt{k_y^2 - (\omega / c)^2}$). As seen, the results are qualitatively similar, and support, undoubtedly, that the metamaterial indeed amplifies the evanescent waves (i.e. waves with $k_y c / \omega > 1$). It should be pointed out that the edge of the Brillouin zone ($k_y a = \pi$) corresponds in Fig. 3.12 to $k_y / k_0 = \pi / 0.88 = 3.57$, i.e. to the range of the horizontal axis. Thus, as expected, the resolution of the system is ultimately limited by the granularity of the material.

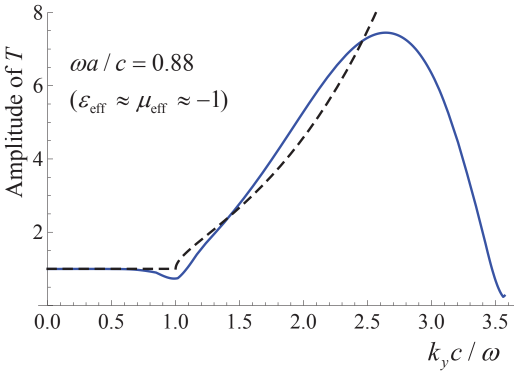

Fig. 3.12. Amplitude of the transfer function T of the metamaterial slab as a function of the transverse wave vector, k_y, for a fixed frequency of operation ω. The slab has dimensions $L_x = a \approx 0.14\lambda_0$ and is infinite along the y- and z- directions. The blue solid line was obtained with a full-wave simulation using CST Microwave Studio [55], whereas the black dashed line represents the transfer function of an ideal Pendry's lens with $\varepsilon \approx \mu \approx -1$.

Using a full-wave electromagnetic simulator [55], the case wherein a magnetic line source (infinitely extended along the z direction) (inset of Fig. 3.13a) is placed at a distance d_1 above the 2D metamaterial slab was studied. The slab has the same parameters as in Fig. 3.12, but it is finite along the y-direction, with $L_y = 30.55a$. The magnetic field profile was calculated at a plane located at a distance d_2 below the slab. It was assumed that $d_1 = d_2 = 0.5L_x = 0.07\lambda_0$. Notice that the slab thickness corresponds to a single period of the bulk metamaterial. In principle, unlike in other configurations reported in the literature, this will not create significant problems, because when the permittivity of the host material is near zero, the electromagnetic wave that illuminates the material slab may "see" the material as a continuous material, independent of the exact thickness of the material in the direction of propagation [37] (however this property may not hold when the excitation is placed in the very near-field of the slab due to the excitation of higher-order diffraction modes). The normalized magnetic field at the image plane is depicted in Fig. 3.13a as a function of y / λ_0 (solid green curve), where λ_0 is the wavelength associated with the frequency of operation that provides $\varepsilon_{\text{eff}} \approx \mu_{\text{eff}} \approx -1$. The half-power beamwidth (HPBW) is equal to $0.2\lambda_0$.

In Fig. 3.13a the imaging performance of the 3D metamaterial configuration (Sec. III.3.3.2) is also analyzed, based on a setup analogue to that considered in the 2D case. The 3D metamaterial parameters are as in Fig. 3.8. The dimensions of the slab in the x and y directions are exactly the same as those considered for the 2D slab. Similarly, it was assumed that $d_1 = d_2 = 0.5L_x = 0.07\lambda_0$. In Fig. 3.13a the profile of the magnetic field at the image plane obtained using the 3D-metamaterial (solid blue line) is shown at the frequency where the effective parameters of both configurations are $\varepsilon_{\text{eff}} \approx \mu_{\text{eff}} \approx -1$. Notice that the wave is *P*-polarized. Interestingly, the HPBW obtained using the spherical inclusions is precisely the same as the one obtained using cylindrical inclusions and it is equal to $0.2\lambda_0$. The squared normalized magnetic field at the image plane, when the slab is absent and the distance between the source and the image plane is $d_1 + d_2$ is also reported in Fig. 3.13a (dashed blue curve). It should be noticed that when the lens is present the total distance between the source and the image plane is $d_1 + d_2 + L_x = 0.28\lambda_0$, whereas when the lens is absent the distance is reduced to $d_1 + d_2 = 0.14\lambda_0$. Thus, notwithstanding the greater proximity between the source and the image plane, in the latter case the HPBW increases to $0.3\lambda_0$. For the propagating distance $d_1 + d_2 + L_x$ in free-space, the HPBW is $0.48\lambda_0$. It is clear that the metamaterial lenses enable, indeed, a superlensing effect and compensate the effects of propagation of free-space.

The imaging properties of the 2D lens were also studied when the frequency of operation is detuned from the value $\omega a / c = 0.88$ (frequency where the effective parameters are $\varepsilon_{\text{eff}} \approx \mu_{\text{eff}} \approx -1$) (Fig. 3.13c). As seen in Fig. 3.13c, at a lower frequency of operation $\omega a / c = 0.78$ (solid blue curve), despite the presence of some side lobes may be present, the beam is still sharply focused with the same HPBW as that obtained at $\omega a / c = 0.88$, indicating a reasonable tolerance to the effects of frequency dispersion. However, at $\omega a / c = 0.98$ (solid green line) the lens completely loses its focusing ability.

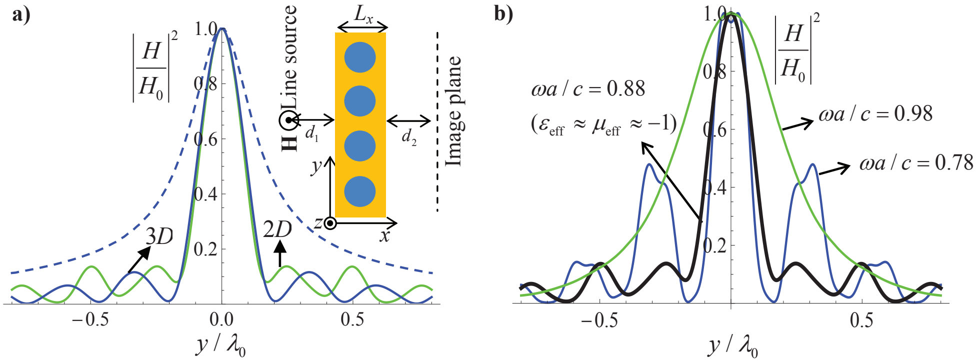

Fig. 3.13. Profiles of the fields for a magnetic line source placed at a distance $d_1 = 0.5L_x$ above the 2D and 3D superlenses. The image plane is located at a distance $d_2 = d_1$ from the lower interface of the lenses. (a) Profile of the square normalized magnetic field for (i) 2D-configuration (solid green curve), (ii) 3D-configuration (solid blue curve) and (iii) without lens (dashed blue curve). The effective parameters at the frequency of operation are such that $\varepsilon_{\text{eff}} \approx \mu_{\text{eff}} \approx -1$. The inset represents the geometry of either the 2D and 3D problems. (c) similar to the result depicted in (a) for the 2D-configuration, but for different frequencies of operation.

The possibility of achieving a superlensing effect for *S*-polarized waves (electric field parallel to the *z*-direction) using the 3D-configuration was studied as well. In order to check this, a simulation was performed in the scenario wherein an electric source (infinitely extended along the *z*-direction) is placed at a distance d_1 above the 3D metamaterial. The slab has dimensions $L_x = a$ and $L_y = 30.55a$ (the inset of Fig. 3.14). The normalized electric field at the image plane is depicted in Fig. 3.14 as a function of y/λ_0 (solid blue line), where λ_0 is the wavelength associated with the frequency of operation where $\varepsilon_{\text{eff}} \approx \mu_{\text{eff}} \approx -1$. The half-power beamwidth (HPBW) is equal to $0.19\lambda_0$, which is slightly narrower than in the case of *P*-polarized waves. This is only possible because of the strong magnetic response of the metamaterial, since it is well known that the near-field imaging of *P*-polarized waves requires $\varepsilon \approx -1$, whereas the near-field imaging of *S*-polarized waves requires $\mu \approx -1$. The square normalized electric field at the image plane when the slab is absent and the distance between the source and the image plane is $d_1 + d_2$ is also shown in Fig. 3.14 (dashed blue curve). Again, notwithstanding the greater proximity between the source and the image plane, in the latter case the HPBW increases to $0.25\lambda_0$.

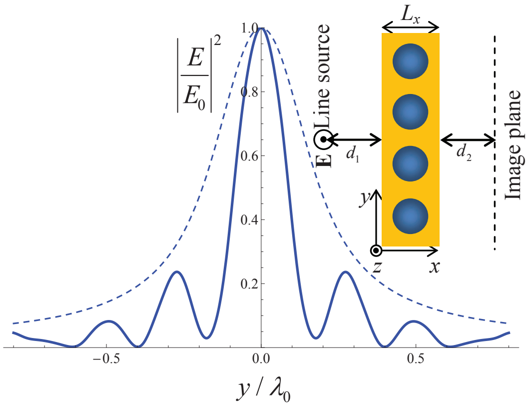

Fig. 3.14. Profiles of the electric field for an electric line source placed at a distance $d_1 = 0.5L_x$ above the superlens (3D-configuration). The solid blue curve is the profile of the field when the lens is present and at a distance $d_1 + d_2 + L_x = 0.28\lambda_0$ of the electric line source, whereas the dashed blue curve is the profile of the field when the lens is absent and at a distance $d_1 + d_2 = 0.14\lambda_0$ of the electric source.

To conclude, let us consider a fully 3D scenario wherein both the metamaterial slab and the source are finite along all the directions of space. To this end, an electrically small horizontal dipole antenna with dimensions $L_{dp} = 0.075\lambda_0$ oriented along the z-direction is considered. The dipole antenna is located at a distance d_1 above the metamaterial slab with dimensions $L_x = a$, and $L_y = L_z = 30.55a$ (Fig. 3.15a). The microstructure of the metamaterial is the same as in the example of Fig. 3.14. In Fig. 3.15b (at the plane *xoy*) the square normalized amplitude of the magnetic field is depicted at a distance $d_1 + d_2 + L_x = 0.28\lambda_0$ from the dipole antenna (solid blue curve) in the presence of the lens, and at a distance $d_1 + d_2 = 0.14\lambda_0$ (dashed blue curve) when the lens absent. The HPBW when the lens is present is equal to $0.09\lambda_0$, while when the lens is absent the HPBW increases to $0.148\lambda_0$. This demonstrates that even in this demanding scenario the lens still provides a remarkable focusing effect, even more exciting than in the previous cases. However, it must be mentioned that the response of the lens may depend on the specific position of the source with respect to the inclusions. In fact, the imaging properties described previously correspond to the case wherein the dipole is placed exactly above a dielectric sphere (center of the unity cell). If the dipole is shifted along the *xoy* plane into an interstitial place, the magnetic field profile at the image plane is significantly changed (discrete black stars in Fig. 3.14b; the HPBW is equal to $0.26\lambda_0$). Clearly, when placed at an interstitial site the source excites all the neighboring spheres with the same strength, which broadens the beam profile. This happens due to the excitation of higher-order diffraction modes (due to the proximity of the dipole and the metamaterial slab), whose description is beyond the validity of effective medium theory. These results reveal that the granularity of the metamaterial may not be negligible in the near-field, and show that when the source is placed in the very-near field the metamaterial cannot be regarded as a truly continuous medium.

Figure 3.14c shows a snapshot in time of the magnetic field at the *xoy* plane when the lens is present, whereas Fig. 3.14d shows a similar plot but for the case where the lens is absent. These results suggest interesting applications for metamaterials formed by a plasmonic host and high index inclusions in imaging. However, in practice, the realization of such systems with passive natural materials may be difficult. Indeed, it can be checked (not shown here) that the loss of the metamaterial formed by HgTe and TiO_2 considered in sections III.3.3.2 and III.3.4 is slightly too large to enable a superlensing effect, even though it may permit focusing (based uniquely on the negative index of refraction) limited by diffraction.

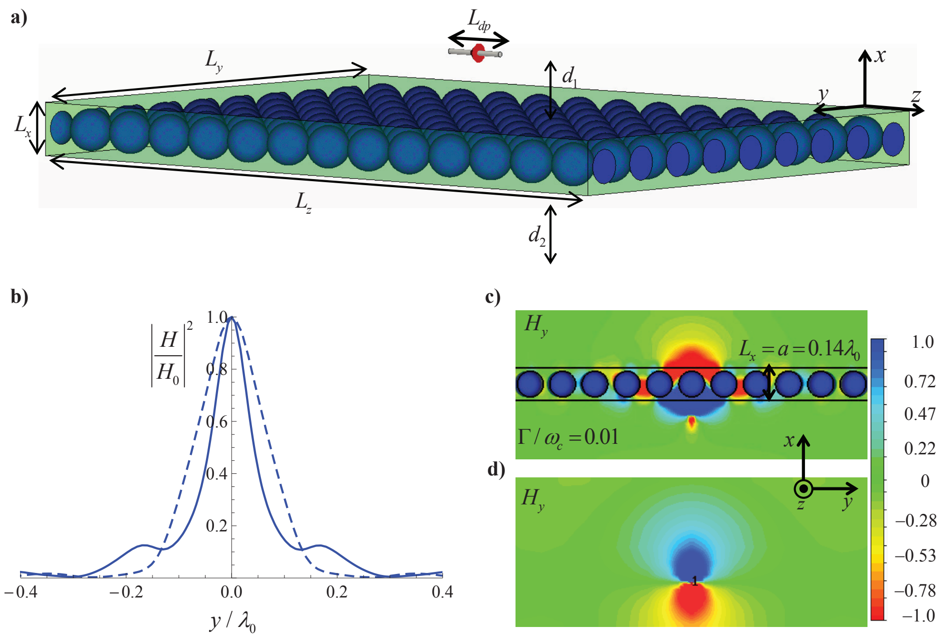

Fig. 3.15. a) Geometry of the finite-sized plasmonic slab with high-index spherical inclusions. The dipole antenna is located at a distance $d_1 = 0.5L_x$ above the slab with dimensions $L_x = a$, and $L_y = L_z = 30.55a$. (b) Profile of the square normalized magnetic field at a distance $d_2 = 0.5L_x$ below the superlens. (c) Snapshot of the magnetic field radiated by the dipole antenna at the *xoy* plane (d) similar to (c) but in a scenario wherein the lens is absent.

III.4. Summary

In this Chapter (Sec. III.2), it was shown how it is possible to self-consistently define the Poynting vector and energy relations in metamaterials with local constitutive parameters, even when negative index of refraction or anomalous values of effective constitutive parameters are considered. It was proven from first-principles considerations based on the general theory derived in [28] that the correct definitions of Poynting vector, stored energy and heating rate in NIMs coincide with those in natural materials after properly defining macroscopic averaged fields and effective constitutive parameters, and that other proposed definitions are not physically meaningful. The results described were also validated with full-wave numerical simulations considering a 2D NIM (the zero index metamaterial described in Chapter I), which indeed supports backward propagation and power flow anti-parallel to phase velocity, showing excellent quantitative agreement with Eq. (3.4) and the theory based on an effective medium approach. Thus, independent of whether one considers one or two levels of homogenization (over an atomic scale in natural media, and over an additional mesoscopic scale in metamaterials), the macroscopic Poynting vector can always be defined self-consistently with its form in vacuum, maintaining its physical meaning of a power flux density vector.

In the second part of the Chapter (Sec. III.3), it was shown that metamaterials formed by spherical or cylindrical dielectric inclusions embedded in a plasmonic host medium, may imitate an ideal continuous DNG material in a frequency window notably wider than conventional designs where the role of the inclusions and the host is interchanged. It was demonstrated using full-wave simulations that the proposed configurations are less affected by loss than conventional designs, and may mimic to some extent the Veselago-Pendry's superlens enabling a strong broadband negative refraction effect and superlensing. Thus, the proposed design may be an exciting route to obtain a DNG response in different frequency regimes.

References

[1] V. G. Veselago, "The electrodynamics of substances with simultaneously negative values of ε and μ," *Sov. Phys. Usp.* **10**, 509, 1968.

[2] J. B. Pendry, "Negative refraction makes a perfect lens," *Phys. Rev. Lett.* **85**, 3966, 2000.

[3] D. R. Smith, W. J. Padilla, D. C. Vier, S. C. Nemat-Nasser, and S. Schultz, "Composite medium with simultaneously negative permeability and permittivity," *Phys. Rev. Lett.* **84**, 4184, 2000.

[4] D. R. Smith and N. Kroll, "Negative refractive index in left-handed materials," *Phys. Rev. Lett.* **85**, 2933, 2000.

[5] C. G. Parazzoli, R. B. Greegor, K. Li, B. E. C. Koltenbah, and M. Tanielian, "Experimental verification and simulation of negative index of refraction using Snell's law," *Phys. Rev. Lett.* **90**, 107401, 2003.

[6] C. L. Holloway, E. F. Kuester, J. Baker-Jarvis, and P. Kabos, "A double negative (DNG) composite medium composed of magnetodielectric spherical particles embedded in a matrix," *IEEE Trans. Antennas and Propag.* **51**, 2596, 2003.

[7] J. Zhou, T. Koschny, M. Kafesaki, and C. M. Soukoulis, "Negative refractive index response of weakly and strongly coupled optical metamaterials," *Phys. Rev. B* **80**, 035109, 2009.

[8] S. F. Rudolph, and A. Grbic, "The design of broadband, volumetric nri media using multiconductor transmission-line analysis," *IEEE Trans. Antennas and Propag.* **58**, 1144, 2010.

[9] V. M. Shalaev, W. Cai, U. K. Chettiar, Hsiao-Kuan Yuan, A. K. Sarychev, V. P. Drachev, and A. V. Kildishev, "Negative index of refraction in optical metamaterials," *Optics Lett.* **30**, 3356, 2005.

[10] A. Shelby, D. R. Smith, and S. Schultz, "Experimental verification of a negative index of refraction," Science **292**, 77, 2001.

[11] N. Fang, H. Lee, C. Sun and X. Zhang, "Sub–diffraction-limited optical imaging with a silver superlens," Science **308,** 534, 2005.

[12] T. Taubner, D.Korobkin, Y.Urzhumov, G.Shvets, and R.Hillenbrand, "Near-field microscopy through a SiC superlens," *Science* **313**, 1595, 2006.

[13] M. J. Freire, R. Marques, and L. Jelinek, "Experimental demonstration of a μ=−1 metamaterial lens for magnetic resonance imaging," *Appl. Phys. Lett.* **93**, 231108, 2008.

[14] S.C. Kehr, Y.M. Liu, L.W. Martin, P. Yu, M. Gajek, S.-Y. Yang, C.-H. Yang, M. T. Wenzel, R. Jacob, H.-G. von Ribbeck, M. Helm, X. Zhang, L.M. Eng, and R. Ramesh, "Near-field examination of perovskite-based superlenses and superlens-enhanced probe-object coupling," *Nat. Commun.* **2**, 249, 2011.

[15] I. I. Smolyaninov, Yu-Ju Hung and C. C. Davis, "Sub-diffraction-limited optical imaging with a silver superlens," Science **315,** 1699, 2007.

[16] E. Cubukcu, K. Aydin, and E. Ozbay, "Subwavelength resolution in a two-dimensional photonic-crystal-based superlens," *Phys. Rev. Lett.* **91**, 207401, 2003.

[17] A. Alù and N. Engheta, "Pairing an epsilon-negative slab with a mu-negative slab: Resonance, tunneling and transparency," *IEEE Trans. Antennas Propag*. **51**, 2558, 2003.

[18] R. Marques, F. Medina, and R. Rafii-El-Idrissi, "Role of bianisotropy in negative permeability and left-handed metamaterials," *Phys. Rev. B* **65**, 144440, 2002.

[19] J. Lu, T. M. Grzegorczyk, Y. Zhang, J. Pacheco, Jr., B.-I. Wu, J. A. Kong, and M. Chen, “Cherenkov radiation in materials with negative permittivity and permeability,” *Opt. Express* **11**, 723, 2003.

[20] R. W. Ziolkowski and A. Kipple, “Application of double negative metamaterials to increase the power radiated by electrically small antennas,” *IEEE Trans. Antennas Propag.* **51**, 2626, 2003.

[21] S. A. Cummer, “Dynamics of causal beam refraction in negative refractive index materials,” *Appl. Phys. Lett.* **82**, 2008, 2003.

[22] C. Caloz, C.-C. Chang, and T. Itoh, “Full-wave verification of the fundamental properties of left-handed materials in waveguide configurations,” *J. Appl. Phys*. **90**, 5483, 2001.

[23] P. Kinsler, A. Favaro, “Four Poynting theorems,” and M. W. McCall, *Eur. J. Phys.* **30**, 983 (2009).

[24] V. A. Markel, “Correct definition of the Poynting vector in electrically and magnetically polarizable medium reveals that negative refraction is impossible,” *Opt. Express*, **16**, 19152 (2008).

[25] J. D. Jackson, *Classical Electrodynamics*, Wiley, 1998.

[26] L. Landau and E. Lifschitz, *Electrodynamics of Continuous Media*, Butterworth-Heinemann, 1984.

[27] W. Gough, “Poynting in the wrong direction?,” *Eur. J. Phys.* **3**, 83 1982.

[28] M. G. Silveirinha, “Poynting vector, heating rate, and stored energy in structured materials: A first-principles derivation,” *Phys. Rev. B* **80**, 235120, 2009.

[29] V. Agranovich and V. Ginzburg, *Spatial Dispersion in Crystal Optics and the Theory of Excitons*, Willey-Interscience, New York, 1966.

[30] N. Garcia, and M. Nieto-Vesperinas, “Left-handed materials do not make a perfect lens,” *Phys. Rev. Lett.* **88**, 207403, 2002.

[31] D. R. Smith, W. J. Padilla, D. C. Vier, S. C. Nemat-Nasser, and S. Schultz, “Limitations on subdiffraction imaging with a negative refractive index slab,” *App. Phys. Lett.* **82**, 1506, 2003.

[32] V. A. Podolskiy, and E. E. Narimanov, “Near-sighted superlens,” *Opt. Lett.* **30**, 75, 2005.

[33] G. Shvets, and Y. A. Urzhumov, “Engineering the electromagnetic properties of periodic nanostructures using electrostatic resonances,” *Phys. Rev. Lett.* **93**, 243902, 2004.

[34] A. Alù, A. Salandrino, and N. Engheta, “Negative effective permeability and left-handed materials at optical frequencies,” *Opt. Express* **14**, 1557, 2006.

[35] A. Alù, and N. Engheta, “Three-dimensional nanotransmission lines at optical frequencies: A recipe for broadband negative-refraction optical metamaterials,” *Phys. Rev. B* **75**, 024304, 2007.

[36] D. R. Fredkin, and I. D. Mayergoyz, “Resonant behavior of dielectric objects (electrostatic resonances),” *Phys. Rev. Lett.* **91**, 253902, 2003.

[37] M. Silveirinha and N. Engheta, “Design of matched zero-index metamaterials using nonmagnetic inclusions in epsilon-near-zero media,” *Phys. Rev. B* **75**, 075119, 2007.

[38] J. D. Joannopoulos, S. G. Johnson, J. N. Winn, and R. D. Meade, *Photonic Crystals: Molding the Flow of Light*, Princeton University Press, 2nd ed, 2008.

[39] A.R. McGurn, and A. A. Maradudin, “Photonic band structures of two- and three-dimensional periodic metal or semiconductor arrays,” *Phys. Rev. B* **48**, 17576, 1993.

[40] V. Kuzmiak, A. A. Maradudin, and F. Pincemin, “Photonic band structures of two-dimensional systems containing metallic components,” *Phys. Rev. B* **50**, 16835, 1994.

[41] V. Kuzmiak, and A.A. Marudin, “Photonic band structures of one- and two-dimensional periodic systems with metallic components in the presence of dissipation,” *Phys. Rev. B* **55**, 7427, 1997.

[42] A. Raman, and S. Fan, “Photonic band structure of dispersive metamaterials formulated as a hermitian eigenvalue problem,” *Phys. Rev. Lett.* **104***,* 087401, 2010.

[43] M. G. Silveirinha, “Time domain homogenization of metamaterials,” *Phys. Rev. B* **83**, 165104, 2011.

[44] L. Lewin, “The electrical constants of a material loaded with spherical particles,” *Proc. Inst. Elec. Eng.* **94**, 65, 1947.

[45] W. G. Spitzer, D. Kleinman, and D.Walsh, “Infrared properties of hexagonal silicon carbide” *Phys. Re*v. **117**, 113, 1959.

[46] M. Choi, S. H. Lee, Y. Kim, S. B. Kang, J. Shin, M. H. Kwak, Kwang-Young Kang, Yong-Hee Lee, N. Park, and B. Min, “A terahertz metamaterial with unnaturally high refractive index,” *Nature* **470**, 369, 2011.

[47] N. Matsumoto, T. Hosokura, K. Kageyama, H. Tagaki, Y. Sakabe, and M. Hangyo, “Analysis of dielectric response of TiO_2 in terahertz frequency region by general harmonic oscillator model,” *Jpn. J. Appl. Phys.* **47,** 7725, 2008.

[48] H. C. Guo, W. M. Liu, and S. H. Tang, “Terahertz time-domain studies of far-infrared dielectric response in 5 mol % MgO:$LiNbO_3$ ferroelectric single crystal,” *J. Appl. Phys.* **102**, 033105, 2007.

[49] T. Okada, M. Nagai, and K. Tanaka, “Resonant phase jump with enhanced electric field caused by surface phonon polariton in terahertz region,” *Opt. Express* **16**, 5633, 2008.

[50] J. G. Rivas, C. Janke, P. Bolivar, and H. Kurz, “Transmission of THz radiation through InSb gratings of subwavelength apertures,” *Opt. Express* **13**, 847, 2005.

[51] A. Rogalski, “HgCdTe infrared detector material: history, status and outlook,” *Rep. Prog. Phys*. **68**, 2267, 2005.

[52] O. Madelung, U. Rössler, M. Schulz (Editors), *Landolt-Börnstein - Group III Condensed Matter Numerical Data and Functional Relationships in Science and Technology* - New Series, Springer, Subvolume 41B: II-VI and I-VII Compounds; Semimagnetic Compounds, 1999.

[53] R. R. Galazka, “Temperature dependence of intrinsic concentration in HgTe,” *Phys. Lett.* **32**A, 101, 1970.

[54] J. J. Dubowski, T. Dietl, W. Szymanska, and R. R. Galazka, “Electron scattering in $Cd_xHg_{1-x}Te$,” *J. Phys. Chem. Solids* **42**, 351, 1981.

[55] CST Microwave Studio Suite^{TM} 2010, (http://www.cst.com).

[56] V. C. Nguyen, L. Chen, and K. Halterman, “Total Transmission and Total Reflection by Zero Index Metamaterials with Defects,” *Phys. Rev. Lett.* **105**, 233908, 2010.

[57] Y. Xu, and H. Chena, “Total reflection and transmission by epsilon-near-zero metamaterials with defects,” *Appl. Phys. Lett.* **98**, 113501, 2011.

IV. Macroscopic Electromagnetic Response of Complex Shaped Spatially Dispersive Bodies Formed by Metallic Wires

IV.1. Introduction

As discussed in the second Chapter of this thesis (Sec. II.2.2), the effective response of metamaterials formed by inclusions with characteristic sizes comparable to the wavelength of operation is typically characterized by spatial dispersion. This is equivalent to say that in such spatially dispersive metamaterials the polarization vector depends not only on the macroscopic electric field, but also on its spatial derivatives [1]. As is well known, this implies that in the bulk metamaterial region the electric displacement vector **D** is related to the electric field **E** through a constitutive relation of the form $\mathbf{D} = \overline{\overline{\varepsilon}}(\omega, -i\nabla)\cdot\mathbf{E}$, which for the case of fields with a plane wave type spatial dependence of the form $e^{i\mathbf{k}\cdot\mathbf{r}}$ reduces simply to $\mathbf{D} = \overline{\overline{\varepsilon}}(\omega, \mathbf{k})\cdot\mathbf{E}$.

One of the anomalous properties of materials characterized by spatial dispersion is that when illuminated by electromagnetic waves, “additional waves” can be excited and hence the classical boundary conditions that impose the continuity of the tangential fields at the interfaces are insufficient to solve a scattering problem based on mode matching. The usual way to fix this problem is to impose additional boundary conditions (ABC’s) [1-4], but generally this analytical approach is restricted to very specific geometries of the involved materials. In fact, things get much more complicated when one desires to describe the interaction of electromagnetic waves with complex shaped geometries of spatially dispersive bodies, since in such scenarios it is not possible to solve the scattering problem using mode matching techniques. One option to overcome this drawback is the numerical modeling of the spatially dispersive response of the metamaterial. The most straightforward solution is based on obtaining a spatial relation between **E** and **D** by applying an inverse Fourier transform $(k_l \leftrightarrow -i\frac{\partial}{\partial l},\, l = x, y, z)$ to the bulk constitutive relation [5-12]. However, even though this solution is apparently valid, it is not necessarily the correct one. In fact, the constitutive relation $\mathbf{D} = \overline{\overline{\varepsilon}}(\omega, \mathbf{k}) \cdot \mathbf{E}$ is only valid in the bulk metamaterial region and it does not hold exactly at the boundary between the metamaterial and a given dielectric/metallic region. This, of course, can create ambiguities in the solution of electromagnetic problems involving bodies formed by spatially dispersive materials. Hence, it is logical to ask what is the correct way of linking the **E** and **D** fields at the interface between a spatially dispersive metamaterial and a metallic/dielectric region.

In this Chapter, it is shown that the correct manner of linking the **D** and **E** fields across the interface does not reduce to a simple Fourier inversion of the bulk constitutive relations, but rather requires the knowledge of internal (microscopic) degrees of freedom of the involved materials at the boundary. Furthermore, it is discussed how the Maxwell's equations can be solved using numerical methods in the presence of arbitrarily shaped bodies with a spatially dispersive response. To this end, the electromagnetic response of arbitrarily shaped bodies of metamaterials formed by "wire media" is investigated. It is well known that such microstructured material is characterized by a strong spatially dispersive response [13-16], and that such a property may be the root of interesting applications in the emerging fields of nanophotonics and plasmonics [17-25, J.2]. Even though the uniaxial wire medium [13] is the most well-known metamaterial with a nonlocal response, such a property is also inherent to other wire media topologies, including arrays of long helices and arrays of both connected and nonconnected crossed wires [4, 16]. Here, the double wire medium – a double array of nonconnected metallic wires – is chosen for illustration purposes, but the theory can be trivially extended to other wire medium topologies. It is demonstrated that a naive numerical discretization of the spatially dispersive response of the double wire medium based on an inverse Fourier transform of $\mathbf{D} = \overline{\overline{\varepsilon}}(\omega, \mathbf{k}) \cdot \mathbf{E}$ may drastically fail at the interface, even for geometries of the metamaterial where mode matching techniques can be used. On the other hand, it is shown that a discretization based on an effective medium framework wherein the metamaterial response is expressed in terms of additional variables with known physical meaning [26] is a correct solution to link the **E** and **D** fields at the boundary.

IV.2. Model Based on the Bulk Electromagnetic Response

IV.2.1. The Interface Problem

With the objective of highlighting that a discretization of the spatially dispersive response of a metamaterial based on an inverse Fourier transform is ambiguous at the interfaces, let us first consider a specific example.

Without loss of generality, suppose that both the electric field and electric displacement field are oriented along the z-direction, and are linked in the bulk region as follows:

$$D_z = \varepsilon(\omega, -i\nabla) E_z . \tag{4.1}$$

Furthermore, for the purpose of illustration it is assumed that the material is non-magnetic and that the dielectric function is a rational function of the wave vector, so that

$$\varepsilon(\omega, \mathbf{k}) = \varepsilon_h + \frac{b_0}{a_0 - a_2 k_x^2 + \dots}, \tag{4.2}$$

where ε_h, b_0, a_0, a_2,..., are independent of the wave vector, but in general may depend on frequency. It is supposed that the material has a center of symmetry at the microscopic level so that the dielectric function is an even function of $\mathbf{k}$. Moreover, it is assumed without loss of generality that $\varepsilon(\omega,\mathbf{k})$ depends exclusively on $k_x \leftrightarrow -i\frac{\partial}{\partial x}$.

In case the only nonzero coefficients are a_0, a_2, it is clear from Eqs. (4.1) and (4.2), that the D_z and E_z fields satisfy the following partial differential equation in the bulk region:

$$a_0 P_{c,z} + \partial_x^2\left(a_2 P_{c,z}\right) = b_0 E_z\,, \tag{4.3}$$

where $P_{c,z} = D_z - \varepsilon_h E_z$ is here defined as the polarization of the medium with respect to a background with permittivity ε_h. Notice that if the material has a local response the coefficient a_2 vanishes.

Let us now suppose that the plane $x = 0$ corresponds to an interface between two different materials, so that one of the materials occupies the semispace $x > 0$, whereas the second material occupies the region $x < 0$, and that the constitutive relation in both bulk materials is of the generic form of Eq. (4.2). Evidently, the coefficients a_0, a_2, and b_0 in general differ in the two materials. Therefore, it is tempting to consider that the $P_{c,z}$ and E_z fields are related in all space by:

$$a_0\left(x\right) P_{c,z} + \partial_x^2\left(a_2\left(x\right) P_{c,z}\right) = b_0\left(x\right) E_z\,. \tag{4.4}$$

The spatial relation between the D_z and E_z fields (Eq. (4.4)) together with the standard macroscopic Maxwell's Equations $\nabla\times\mathbf{E} = i\omega\mu_0\mathbf{H}$ and $\nabla\times\mathbf{H} = \mathbf{j}_{ext} - i\omega\mathbf{D}$ and the

Sommerfeld radiation completely determine, for a given excitation $\mathbf{j}_{ext}$, the electromagnetic fields $(\mathbf{E},\mathbf{H})$ in all space.

The outlined approach based on an inverse Fourier transform of the constitutive relation $\mathbf{D}=\overline{\overline{\varepsilon}}(\omega,\mathbf{k})\cdot\mathbf{E}$ and other variants are the basis of several studies which aim to characterize the electromagnetic response of either nanoparticles or macroscopic bodies made of either natural media or metamaterials with spatial dispersion [5-12]. However, it is important to underscore that even if the bulk constitutive relation (4.3) holds exactly up to the boundary, in general the form of Eq. (4.4) remains unjustified at $x=0$, i.e., at the boundary. The reason is that there are many inequivalent ways of relating $P_{c,z}$ and E_z through a differential equation, but which reduce to Eq. (4.3) in the bulk regions. In fact, since for an abrupt interface the coefficients a_0, a_2, and b_0 are discontinuous at $x=0$, *a priori* nothing forbids that $P_{c,z}$ and E_z are linked by, for example,

$$a_0(x)P_{c,z}+\partial_x\left[a_2(x)\partial_x P_{c,z}\right]=b_0(x)E_z, \tag{4.5}$$

rather than by Eq. (4.4). Notice that the above equation is equivalent to Eq. (4.4) in the bulk regions (i.e. for $x\neq 0$ where $a_2(x)=const.$) but not at $x=0$. Indeed, the form of Eq. (4.4) suggests that $\partial_x\left(a_2 P_{c,z}\right)$ is continuous at the interface, whereas differently Eq. (4.5) implies that $a_2\partial_x P_{c,z}$ is continuous at the interface. Hence, the two formulations imply different boundary conditions at the interfaces, even though they are equivalent in the bulk regions.

In fact, there are infinitely many possibilities of linking $P_{c,z}$ and E_z at the boundary, and some of them cannot even be formulated in terms of the coefficients a_0, a_2, and b_0

of the effective medium model! For example, if one replaces the term $\partial_x\left(a_2 P_{c,z}\right)$ in Eq. (4.4) by the term $A(x)\partial_x\left[A^{-1}(x)\partial_x\left(a_2 P_{c,z}\right)\right]$ where $A(x)$ is an *arbitrary* piecewise constant function of x discontinuous at $x=0$, one obtains other inequivalent ways of linking $P_{c,z}$ and E_z in all space, involving an extra parameter ($A(x)$) which is unrelated to the bulk material dielectric function.

IV.2.2. Double Wire Medium

As mentioned in the Introduction, without loss of generality this work is focused in the electromagnetic response of the double wire medium. This material is formed by two arrays of metallic wires with radius r_w, such that each array of parallel wires is arranged in a square lattice with lattice constant a and tilted by $\pm 45^\circ$ with respect to the interfaces. One set of wires is oriented along the direction $\hat{\mathbf{u}}_1=(1,0,1)/\sqrt{2}$ while the complementary set of wires is oriented along the direction $\hat{\mathbf{u}}_2=(-1,0,1)/\sqrt{2}$. Both sets of wires lie in planes parallel to the *xoz* plane and the distance between adjacent perpendicular wires is $a/2$ [Figs. 4.1a and 4.1b].

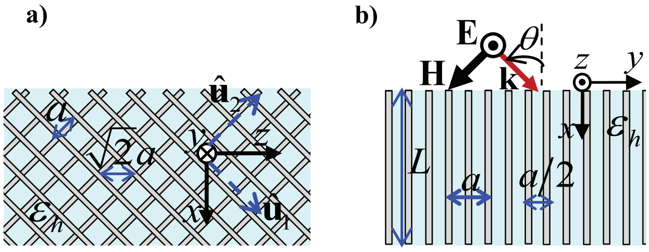

Fig. 4.1. (a) and (b): Cuts of a “double wire medium” along the *xoy* and *xoz* planes, respectively. The slab has thickness L.

The wires stand in a host material with relative permittivity ε_h. The effective response of the “double wire medium” is characterized by a dielectric function $\overline{\overline{\varepsilon}}(\omega,\mathbf{k})$ such that [3, 15, 27]:

$$\frac{\overline{\overline{\varepsilon}}}{\varepsilon_0} = \varepsilon_h \hat{\mathbf{u}}_y \hat{\mathbf{u}}_y + \varepsilon_{11} \hat{\mathbf{u}}_1 \hat{\mathbf{u}}_1 + \varepsilon_{22} \hat{\mathbf{u}}_2 \hat{\mathbf{u}}_2$$

$$\varepsilon_{ii}(\omega, k_i) = \varepsilon_h \left(1 + \frac{1}{\frac{1}{(\varepsilon_m / \varepsilon_h - 1) f_V} - \frac{\varepsilon_h (\omega / c)^2 - k_i^2}{\beta_p^2}} \right), \tag{4.6}$$

where $\varepsilon_0 \varepsilon_m$ is the permittivity of the metal, $f_V = \pi (r_w / a)^2$ is the volume fraction of each set of wires, $\beta_p = \{2\pi / [\ln(a / 2\pi r_w) + 0.5275]\}^{1/2} / a$ is the plasma wave number and c is the speed of light in vacuum. For simplicity, in this Chapter it is considered that the propagation is along the *xoy* plane with $k_z = 0$ (or equivalently $\partial_z = 0$), and it is also assumed that the only nontrivial electromagnetic field components are E_z, D_z, H_x and H_y. In this scenario, the dielectric function reduces to a scalar in the *xoy* plane, $\varepsilon(\omega, k_x) = \varepsilon_{ii}(\omega, k_i)$, $i = 1, 2$, because for $k_z = 0$ we have $k_1 = k_x / \sqrt{2} = -k_2$, and hence Eq. (4.6) becomes:

$$\varepsilon(\omega, k_x) = \varepsilon_h \left(1 + \frac{1}{\frac{1}{(\varepsilon_m / \varepsilon_h - 1) f_V} - \frac{\varepsilon_h (\omega / c)^2 - k_x^2 / 2}{\beta_p^2}} \right), \tag{4.7}$$

which is clearly of the same form as in Eq. (4.2), i.e., it is a rational function of the wave vector.

Since the only non-zero field components are the E_z, D_z, H_x and H_y fields, it is easily found that the Maxwell's equations, $\nabla \times \mathbf{E} = i\omega\mu_0 \mathbf{H}$ and $\nabla \times \mathbf{H} = \mathbf{j}_{ext} - i\omega \mathbf{D}$, reduce to the scalar equation:

$$\frac{\partial^2}{\partial x^2} E_z + \frac{\partial^2}{\partial y^2} E_z + \left(\frac{\omega}{c} \right)^2 \frac{D_z}{\varepsilon_0} = -i\omega\mu_0 j_{s,z}, \tag{4.8}$$

where $\mathbf{j}_{ext} = j_{s,z}\hat{\mathbf{z}}$ represents an external current density, i.e. an external excitation.

Therefore, provided one is able to link E_z and D_z in all space, the Maxwell's Equations can be solved univocally. Next, it is discussed how this can be done based on Eq. (4.7).

IV.2.2.1 Constitutive Relations in the Bulk Region

Similar to what was outlined in Sec. IV.2.1, substituting Eq. (4.7) into Eq. (4.1) and calculating the inverse Fourier transform ($i\,k_x \leftrightarrow \partial_x$) of the resulting expression, permits obtaining a spatial relation between the electric field E_z and the electric displacement D_z that makes manifest the spatially dispersive nature of the response of the metamaterial:

$$\left[\frac{1}{2}\frac{\partial^2}{\partial x^2} + \varepsilon_h\left(\frac{\omega}{c}\right)^2 + \beta_c^2\right]\frac{P_{c,z}}{\varepsilon_0} + \varepsilon_h\beta_p^2 E_z = 0\,, \tag{4.9}$$

where $\beta_c^2 = -\beta_p^2 \big/ \left[\left(\varepsilon_m/\varepsilon_h - 1\right) f_V\right]$ and $P_{c,z} = D_z - \varepsilon_0\varepsilon_h E_z$. This is analogous to Eq. (4.3) for the particular case of the double wire medium. It should be noted that $P_{c,z}$ is the contribution to the polarization vector due to the conduction currents in the nanowires. Thus, Eq. (4.9) effectively determines the response of the conduction polarization current to the "applied" macroscopic electric field.

Apparently, Eq. (4.9) is only valid in the bulk region of the metamaterial. However, it can be trivially extended to scenarios wherein a metamaterial body is surrounded by a standard dielectric (e.g. air). Indeed, if one regards $\varepsilon_h \equiv \varepsilon_h(x,y)$ as a position dependent function that represents the relative permittivity of the background dielectric regions, and similarly $\beta_p \equiv \beta_p(x,y)$ and $\beta_c \equiv \beta_c(x,y)$ as functions that vanish outside the metamaterial, it is clear that in a standard dielectric Eq. (4.9) reduces to:

$$\left[\varepsilon_h\left(\frac{\omega}{c}\right)^2+\frac{1}{2}\frac{\partial^2}{\partial x^2}\right]P_{c,z}=0. \tag{4.10}$$

This relation is correct because in a standard dielectric $D_z=\varepsilon_0\varepsilon_h E_z$, or equivalently $P_{c,z}=0$. Thus, if one lets $\varepsilon_h\equiv\varepsilon_h(x,y)$, $\beta_p\equiv\beta_p(x,y)$ and $\beta_c\equiv\beta_c(x,y)$ be space dependent, Eq. (4.9) yields the correct constitutive relations both in the bulk metamaterial and in the bulk dielectric region (i.e in the region that surrounds the metamaterial body). If in addition one assumes that Eq. (4.9) also holds across the boundary – which as discussed in Sec. IV.2.1 in general may be a "leap of faith" – then it is possible to calculate the electromagnetic fields in all space by combining and solving Eq. (4.8) and Eq. (4.9). Next, it is briefly described how this can be done numerically using the FDFD method.

IV.2.2.2 FDFD Discretization

The unknown fields [solution of Eqs. (4.8) and (4.9)] can be obtained using the well-known FDFD method already described in Chapter II (Sec. II.2.2.3). Here, Eqs. (2.15a) and (2.15c) are rewritten as follows:

$$\frac{\partial^2}{\partial x^2}F(i,j)=\left[F(i+1,j)-2F(i,j)+F(i-1,j)\right]/\Delta x^2 \tag{4.11a}$$

$$\frac{\partial^2}{\partial y^2}F(i,j)=\left[F(i,j+1)-2F(i,j)+F(i,j-1)\right]/\Delta y^2, \tag{4.11b}$$

where $F=P_{c,z}=D_z-\varepsilon_0\varepsilon_h E_z$. To discretize Eq. (4.9), two FDFD solutions are considered. *(i)* In the first approach Eq. (4.9) is used in all the regions of space to link E_z and D_z. From now on this solution will be referred as the direct inverse transform (DIT1) solution. *(ii)* In the second approach, Eq. (4.9) is used to link E_z and D_z inside the metamaterial as well as for all the nodes that are over the boundary. For nodes that are completely outside the metamaterial (and such that all the neighboring nodes are also outside the metamaterial) it is used simply $D_z = \varepsilon_0 \varepsilon_h E_z$ rather than Eq. (4.9). From now on this implementation will be referred as DIT2. The perfectly matched layer (PML) described in [28] is used to truncate the computation domain in both implementations.

IV.3. Model based on Internal Degrees of Freedom of the Medium

Recent works [4, 26, 29] have shown that the spatial dispersion inherent to wire media may be described by a quasi-static homogenization model that applies in a wide range of scenarios, including the case where the wires are periodically loaded with conducting metallic bodies. In this homogenization framework a current I and an additional potential φ, are associated with each set of wires. The current I may be identified with the current that flows along the metallic wires, whereas the additional potential is the average quasi-static potential drop from a given wire to the boundary of the respective unit cell (both the current and the additional potential are interpolated in a suitable manner, so that they become continuous functions of the spatial coordinates) [26].

IV.3.1. Double Wire Medium

In this Section, based on the quasi-static homogenization model mentioned above, a spatial relation between the **E** and **D** fields will be obtained for the double wire medium case. Later, it will be proved that this solution produces results consistent with the true physical response of the material.

IV.3.1.1 Constitutive relations based on the internal degrees of freedom

For the case of the double wire medium the electrodynamics of the metamaterial is described by the following set of equations [4, 26]:

$$\nabla \times \mathbf{E} = i\omega\mu_0 \mathbf{H} \tag{4.12}$$

$$\nabla \times \mathbf{H} = \mathbf{j}_{ext} - i\omega \mathbf{D} \tag{4.13}$$

$$\frac{\partial}{\partial x_\alpha}\varphi_\alpha = -(Z_w - i\omega L_w) I_\alpha + E_\alpha \tag{4.14}$$

$$\frac{\partial}{\partial x_\alpha} I_\alpha = i\omega C_w \varphi_\alpha , \tag{4.15}$$

$$\mathbf{D} = \varepsilon_0 \varepsilon_h \mathbf{E} + \frac{1}{-i\omega}\sum_\alpha \frac{I_\alpha}{A_{cell}} \hat{\mathbf{u}}_\alpha \tag{4.16}$$

where $A_{cell} = a^2$, $\hat{\mathbf{u}}_\alpha$ is a unit vector that defines the orientation of the α-th set of wires (α=1,2), C_w, L_w and Z_w are the effective capacitance, inductance and self-impedance of the wires per unit length of a wire, respectively [4, 26], $\mathbf{j}_{ext}$ represents an external excitation, and the second term in the right-hand side of Eq. (4.16) is the macroscopic density of current associated with flow of charges along the metallic wires, $\mathbf{J}_w = \sum_\alpha \frac{I_\alpha}{A_{cell}} \hat{\mathbf{u}}_\alpha$. In the above, I_α and φ_α are the current and additional potential associated with the α-th set of wires, and $E_\alpha = \hat{\mathbf{u}}_\alpha \cdot \mathbf{E}$ ($x_\alpha = \hat{\mathbf{u}}_\alpha \cdot \mathbf{r}$ with $\mathbf{r} = (x, y, z)$). Thus, substituting Eq. (4.14) into Eq. (4.15) it is found that:

$$C_w \frac{\partial}{\partial x_\alpha}\left(\frac{1}{C_w}\frac{\partial I_\alpha}{\partial x_\alpha}\right) + \left(\frac{\omega}{c}\right)^2 \varepsilon_h I_\alpha + i\omega C_w Z_w I_\alpha = i\omega C_w E_\alpha \tag{4.17}$$

where it was used the fact that $C_w L_w = \varepsilon_0 \varepsilon_h \mu_0$ for the case of straight wires [26]. For the configuration of interest in this work, it is known that both the electric displacement vector and the electric field only have a *z*-component. Therefore, for propagation in the *xoy* plane it may written:

$$E_\alpha = \mathbf{E}\cdot\hat{\mathbf{u}}_\alpha = E_z\hat{\mathbf{z}}\cdot\hat{\mathbf{u}}_\alpha = E_z\frac{1}{\sqrt{2}} \qquad (\alpha = 1,2) \qquad (4.18)$$

$$\frac{I_\alpha}{A_{cell}} = \mathbf{J}_w\cdot\hat{\mathbf{u}}_\alpha = J_{w,z}\hat{\mathbf{z}}\cdot\hat{\mathbf{u}}_\alpha = J_{w,z}\frac{1}{\sqrt{2}} \qquad (\alpha = 1,2), \qquad (4.19)$$

and by substituting Eqs. (4.18) and (4.19) into Eq. (4.17) it is obtained:

$$C_w\frac{\partial}{\partial x_\alpha}\left(\frac{1}{C_w}\frac{\partial J_{w,z}}{\partial x_\alpha}\right)+\left(\frac{\omega}{c}\right)^2\varepsilon_h J_{w,z}+i\omega C_w Z_w J_{w,z}=\frac{1}{A_{cell}}i\omega C_w E_z\,. \qquad (4.20)$$

On the other hand, $\frac{\partial}{\partial x_\alpha}=\hat{\mathbf{u}}_\alpha\cdot\nabla$ and since here it is assumed $\frac{\partial}{\partial z}=0$, this implies that $\frac{\partial}{\partial x_\alpha}=\pm\frac{1}{\sqrt{2}}\frac{\partial}{\partial x}$. Hence, the final result is obtained:

$$\frac{1}{2}C_w\frac{\partial}{\partial x}\left(\frac{1}{C_w}\frac{\partial J_{w,z}}{\partial x}\right)+\left(\frac{\omega}{c}\right)^2\varepsilon_h J_{w,z}+i\omega C_w Z_w J_{w,z}=\frac{1}{A_{cell}}i\omega C_w E_z\,. \qquad (4.21)$$

Using now Eq. (4.16) and the definition of $\mathbf{J}_w$, it follows that $D_z=\varepsilon_0\varepsilon_h E_z-\frac{J_{w,z}}{i\omega}$ and hence:

$$\begin{aligned}&\frac{C_w}{2}\frac{\partial}{\partial x}\left[\frac{1}{C_w}\frac{\partial}{\partial x}\left(\varepsilon_h E_z-\frac{D_z}{\varepsilon_0}\right)\right]+\varepsilon_h\left(\frac{\omega}{c}\right)^2\left(\varepsilon_h E_z-\frac{D_z}{\varepsilon_0}\right)+\\&i\omega C_w Z_w\left(\varepsilon_h E_z-\frac{D_z}{\varepsilon_0}\right)=\frac{C_w}{A_{cell}\varepsilon_0}E_z\end{aligned}\,. \qquad (4.22)$$

Since $\beta_p^2=C_w/\left[\varepsilon_0\varepsilon_h A_{cell}\right]$ and $Z_w=-\left[i\omega\pi r_w^2\varepsilon_0\varepsilon_h(\varepsilon_m/\varepsilon_h-1)\right]^{-1}=\beta_c^2/\left[i\omega C_w\right]$ where $\beta_c^2=-\beta_p^2/\left[\left(\varepsilon_m/\varepsilon_h-1\right)f_V\right]$ [4, 26] it is possible to write Eq. (4.22) as follows:

$$\frac{\varepsilon_h\beta_p^2}{2}\frac{\partial}{\partial x}\left[\frac{1}{\varepsilon_h\beta_p^2}\frac{\partial}{\partial x}\frac{P_{c,z}}{\varepsilon_0}\right]+\left[\varepsilon_h\left(\frac{\omega}{c}\right)^2+\beta_c^2\right]\frac{P_{c,z}}{\varepsilon_0}+\varepsilon_h\beta_p^2 E_z=0\,. \qquad (4.23)$$

As already mentioned in Sec. IV.2.2, the solution of Eqs. (4.8) and (4.9) allows determining the unknown electromagnetic fields. Similarly, Eq. (4.23) together with Eq. (4.8) (which can also be obtained from Eqs. (4.12) and (4.13)) form a linear system that permits calculating the electromagnetic fields in all space.

The parameters C_w, L_w and Z_w associated with the quasi-static model are all independent of spatial derivatives. More specifically, C_w, L_w and Z_w depend on the geometry of the material and on the properties of the host/metal. For this reason, this formalism is based on a framework wherein the response of the wire medium is "local" (even though its electrodynamics is nonlocal). Hence, it is reasonable to assume that Eq. (4.23) holds even across a boundary between two materials with different structural parameters, in the same sense that the Maxwell's equations can hold at the interface between two dielectrics. Notice that as already mentioned, a standard dielectric can also be described with this formalism since it can be considered as the limit of a nanowire material with vanishingly thin wires.

Clearly, the effective medium formalism associated with the set of Eqs. (4.12) - (4.16) is based on the knowledge of the dynamics of the additional variables I and φ , which have known physical meaning, and thus is based on the knowledge of internal degrees of freedom of the material.

It should be noted that Eq. (4.23) is precisely the same as Eq. (4.9) in the bulk region, i.e., when β_p and ε_h are constant and independent of the position. However, the two equations are completely different at the interfaces, since the parameters β_p, β_c and ε_h may vary with space. This happens if for example the permittivity of the host medium or the radii of the wires vary in space.

In the same manner as in Sec. IV.2.2, in the quasi-static model it is assumed that $\varepsilon_h = \varepsilon_h(x,y)$, $\beta_p = \beta_p(x,y)$ and $\beta_c = \beta_c(x,y)$. In a standard dielectric, the limit

$\beta_p \to 0$ is taken and also $\beta_c(x,y)=0$. Note that in this case β_p cannot be chosen exactly equal to zero, otherwise Eq. (4.23) becomes singular.

IV.3.1.2 FDFD Discretization

The FDFD discretization of the linear system formed by Eqs. (4.23) and (4.8) is analogous to that already described in Sec. IV.2.2. The only relevant difference is that the second order derivatives of Eqs. (4.23) are of the generic form $\frac{\partial}{\partial x}G(x,y)\frac{\partial}{\partial x}U(x,y)$, where $G(x,y)=\varepsilon_h^{-1}(x,y)\beta_p^{-2}(x,y)$ and $U(x,y)=P_{c,z}/\varepsilon_0$. The derivative $\frac{\partial}{\partial x}G(x,y)\frac{\partial}{\partial x}U(x,y)$ is discretized in the following manner:

$$\left[\frac{\partial}{\partial x}G\frac{\partial}{\partial x}U\right](i,j)=\frac{A(i,j)U(i+1,j)}{\Delta x^2}-\frac{B(i,j)U(i,j)}{\Delta x^2}+\frac{C(i,j)U(i-1,j)}{\Delta x^2}, \tag{24}$$

where $A(i,j)=\left[G(i,j)+G(i+1,j)\right]/2$, $B(i,j)=G(i,j)+\left[G(i+1,j)+G(i-1,j)\right]/2$ and $C(i,j)=\left[G(i,j)+G(i-1,j)\right]/2$. Again, the computation domain is truncated with a PML [28]. In this implementation, (4.23) is used in all space (both in the metamaterial and in standard dielectrics or metals). This solution based on the internal degrees of freedom of the metamaterial will be referred as the “IDF solution”.

IV.4. Numerical Results and Discussion

Here, the results obtained with the formulations of Secs. IV.2 and IV.3 are compared, and it is confirmed that the form of the constitutive relations at the interfaces is of crucial importance.

IV.4.1. Scattering Problem: Double Wire Medium – Air Interface

In the first example, a double wire medium slab formed by PEC wires is considered, i.e, $\varepsilon_m=-\infty$. The metamaterial has thickness L and is surrounded by air (Fig. 4.1b). The permittivity of the host region in the double wire medium is taken equal to $\varepsilon_h = 10$, and the lattice constant a is such that $a = L/20$ and $r_w = 0.05a$. Figure 4.2 shows the reflection and transmission coefficients ρ and τ as a function of the normalized frequency $\omega L/c$ for a plane wave that illuminates the slab with an angle of incidence $\theta_i = 15^{\mathrm{o}}$.

The green triangles and the blue circles represent the results computed with the FDFD-SD methods DIT1 and DIT2, respectively (Sec. IV.2.2.2). These two approaches are based on Eq. (4.9). On the other hand, the orange stars were obtained using the FDFD-SD method IDF (Sec. IV.3.1.2) based on the knowledge of the internal structure of the metamaterial [Eq. (4.23)]. Note that in the implementations DIT1 and IDF the parameter β_p^2 is taken as vanishingly small outside the metamaterial. Finally, the black solid curves in Fig. 4.2 were computed using an analytical approach derived in Ref. [3], based on mode matching and additional boundary conditions. It was demonstrated in Ref. [3] that this analytical method compares very well with full-wave simulations that take into account all the minute details of the microstructure of the metamaterial. Therefore, the solid curves can be regarded here as the "exact solution" of the problem.

Figure 4.2 shows that the DIT1 method can be quite inaccurate, as the green curve for the amplitude of the transmission coefficient τ (Fig. 4.2c) largely mismatches the curve obtained with the analytical model (solid black curve). This confirms that a proper discretization of the electromagnetic fields at the interfaces between the spatially dispersive metamaterial and the air region is of crucial importance. On the other hand, the blue curves (DIT2) concur better with the analytical model. The results obtained with the IDF implementation (orange symbols) yield a nearly perfect agreement with the analytical formalism. This supports that to model correctly the electromagnetic response of spatially dispersive bodies it may be necessary to know some of the internal degrees of freedom of the metamaterial, which cannot be accessed simply from the knowledge of the bulk electromagnetic response. Moreover, in Ref. [J.1] it was also shown that in this scenario, the results obtained with the IDF implementation concur extremely well with those predicted by the full-wave simulator [30], further validating the IDF solution.

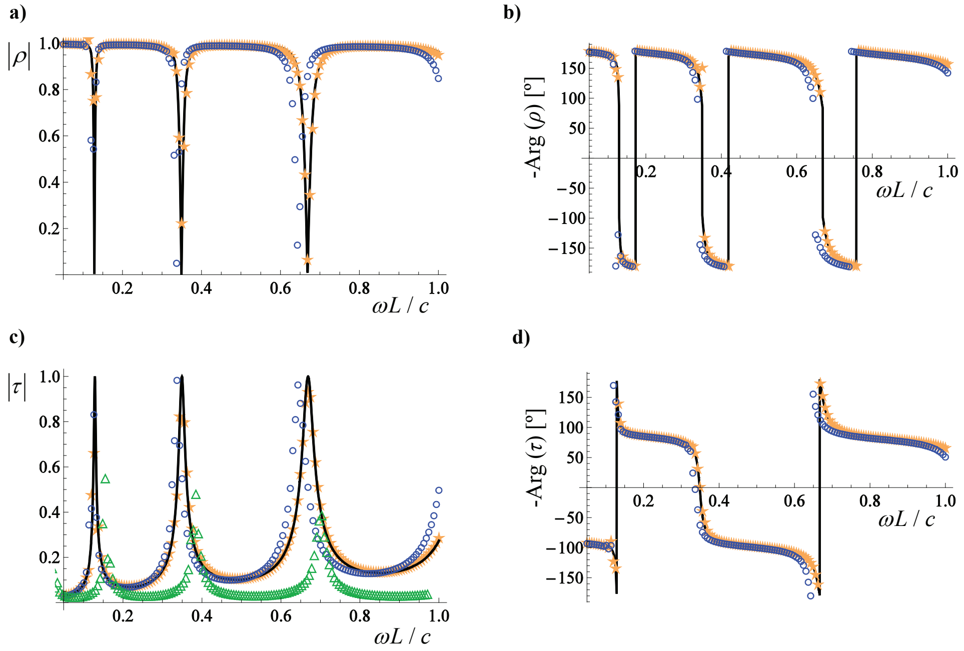

Fig. 4.2. Reflection and transmission coefficients as a function of the normalized frequency for a double wire medium slab with thickness $L = 20a$ illuminated by a plane wave with angle of incidence $\theta_i = 15^\circ$. Solid (black) curves: mode-matching approach based on additional boundary conditions [3]. Star shaped (orange) symbols: IDF approach (Sec. IV.3.1.2); Triangle shaped (green) symbols: DIT1 approach (Sec. IV.2.2.2); Circle shaped (blue) symbols: DIT2 approach (Sec. IV.2.2.2); (a) and (b): amplitude and phase of the reflection coefficient ρ, respectively. (c) and (d): amplitude and phase of the transmission coefficient τ, respectively.

The several dips in the reflection characteristic in Fig. 4.2 are associated with Fabry-Pérot resonances. These resonances are ultra-subwavelength (e.g. the first dip of the reflection coefficient occurs at $\omega L / c \approx 0.13$, which corresponds to the metallic wires with length $L_{wm} = \sqrt{2} L = 0.03\lambda_0$) because the "double wire medium" can be characterized by a very large positive index of refraction with anomalous frequency dispersion in the low frequency limit [20, 25].

To illustrate the application of the method in case of metallic loss, next it is assumed that the metal permittivity $\varepsilon_0\varepsilon_m$ has a Drude-type dispersion (Sec. II.3.1.2). It is assumed that the plasma frequency is such that $\omega_p a / c = 0.125$ and that the collision frequency is $\Gamma / \omega_p = 0.05$. The remaining structural parameters, as well as the incoming wave, are as in Fig. 4.2. The reflection and transmission coefficients calculated with the IDF approach and with the analytical (ABC based) approach [3] are plotted in Fig. 4.3. As seen, the agreement between the FDFD-SD results and the analytical model is excellent, confirming that the constitutive relation (4.23) is valid across the interfaces between different media even in case of metal loss.

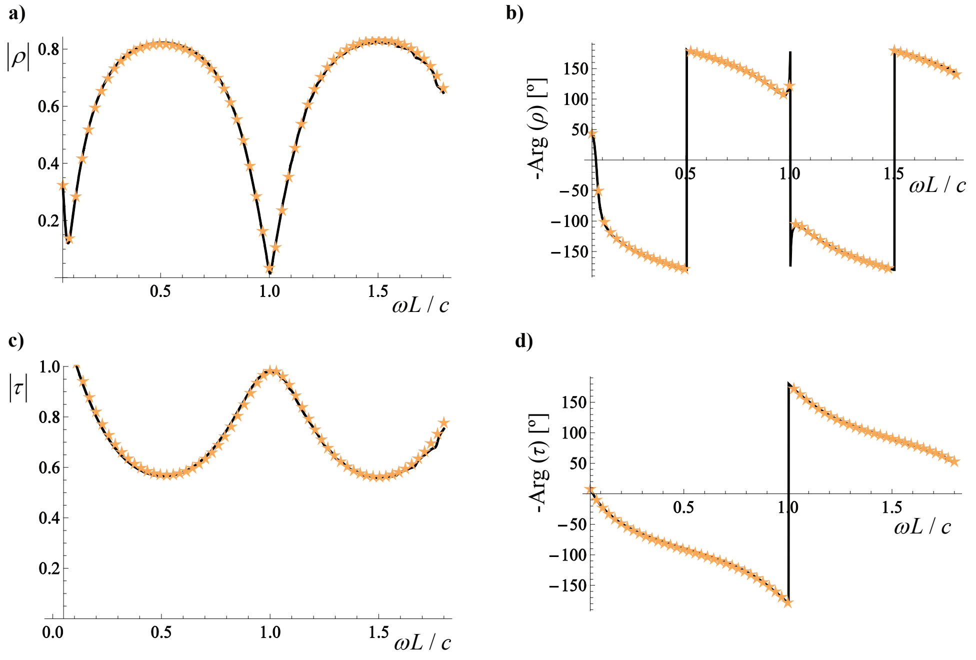

Fig. 4.3. Similar to Fig. 4.2 but the permittivity of the wires is described by the Drude model $\varepsilon_m = 1 - \omega_p^2 \big/ \omega(\omega + i\Gamma)$. The parameters of the Drude Model are $\omega_p a / c = 0.125$ and $\Gamma / \omega_p = 0.05$. Solid (black) curves: mode-matching approach based on additional boundary conditions [3]. Star shaped (orange) symbols: IDF approach (Sec. IV.3.1.2).

IV.4.2. Scattering Problem: Double Wire Medium – PEC Interface

In this Section, the case where the metamaterial slab is backed by a metallic region (a good conductor, which we will refer to as the "ground plane"; the permittivity of the ground plane is taken as $\varepsilon_h \to -\infty$) is considered. The incoming wave propagates in air as in the examples of Sec. IV.4.1, and the angle of incidence is taken equal to $\theta_i = 70^{\mathrm{o}}$. The thickness of the slab is $L = 20a$, the radius of the wires is $r_w = 0.05a$, and the relative permittivity of the host region is $\varepsilon_h = 30$. The metallic wires are assumed PEC.

It is assumed that the metallic wires are in ohmic contact with the ground plane. In the formalism DIT2 (Sect. IV.2.2) there is no way of specifying that the metallic wires are in contact with the "ground plane". On the other hand, in the models DIT1 and IDF this can be taken into account by imagining that the wires are slightly prolonged into the metal, so that they penetrate into a thin transition layer inside the metal. Thus, in the transition layer the parameter β_p (which depends on the radius of the wires) is taken the same as in the metamaterial region. Farther inside the metal, similar to the previous examples, the limit $\beta_p \to 0$ is taken to model the fact that the wires are severed past the transition layer. In the numerical implementation, the thickness of the metal transition layer was taken equal to $0.04L$.

Figure 4.4 shows the phase of the reflection coefficient ρ as a function of frequency. Similar to the previous examples (Fig. 4.2) it is seen in Fig. 4.4a that the agreement between the analytical method based on ABCs (solid black curve) and the IDF approach is nearly perfect. The results also concur well with full-wave simulations that take into account the granularity of the metamaterial (dashed blue curve). On the other hand, both the DIT1 and the DIT2 approaches yield totally wrong results (Fig. 4.4b), because they are unable to capture the dynamics of the current along the wires in the vicinity of the ground plane, and are also unable to capture the fact that the wires are in ohmic contact with the adjacent region. This not only confirms that a proper discretization is of vital importance at the interfaces, but also shows that the methods DIT1 and DIT2 are very inaccurate in a scenario where the double wire medium is attached to a metallic surface.

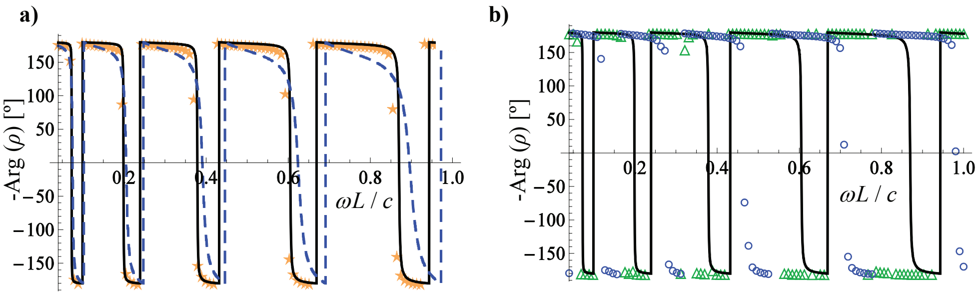

Fig. 4.4. Phase of the reflection coefficient ρ as a function of the normalized frequency for a double wire medium slab with thickness L, backed by a PEC surface. Solid (black) curves: mode-matching approach based on additional boundary conditions [2]. (a) Star shaped (orange) symbols: IDF approach (Sec. IV.3.1.2); Dashed blue curve: CST Microwave Studio [30]. (b) Triangle shaped (green) symbols: DIT1 approach (Sec. IV.2.2.2); Circle shaped (blue) symbols: DIT2 approach (Sec. IV.2.2.2);

It should be underlined that the FDFD implementations do not require any additional boundary conditions, because they assume that Eq. (4.9) or Eq. (4.23), depending on the implementation, are valid across the interface. In some sense, in the FDFD implementations the ABCs are indirectly enforced by the adopted form of the constitutive relation across the interface. For example, the IDF approach, Eq. (4.23) implicitly imposes that both $P_{c,z}$ and $\frac{1}{\varepsilon_h \beta_p^2} \frac{\partial P_{c,z}}{\partial x}$, with $P_{c,z} = D_z - \varepsilon_0 \varepsilon_h E_z$, are continuous across the interfaces. In case of a wire medium adjacent to a dielectric (e.g. air region) this implies (because we take $\beta_p^2 \to 0$ in the dielectric) that $\partial_x P_{c,z}\big|_{diel} = 0$ at the dielectric side of the boundary. This homogeneous boundary condition will effectively ensure (together with the PML boundary conditions) that $P_{c,z} = 0$ in the dielectric region and thus, because $P_{c,z}$ is continuous at the boundary, that the conduction current vanishes at the wire medium side of the interface, $P_{c,z}\big|_{WM} = 0$, which is equivalent to the ABC used in [2]. On the other hand, if the wire medium is adjacent to a metal transition layer (such that the wires are prolonged into the metal), the continuity of $\frac{1}{\varepsilon_h \beta_p^2}\frac{\partial P_{c,z}}{\partial x}$ enforces that $\partial_x P_{c,z}\big|_{WM} = 0$ at the wire medium side of the boundary, because $\varepsilon_h \to -\infty$ at the metal side. This boundary condition is also equivalent to that considered in Ref. [2]. Thus, it follows that the IDF approach is compatible with the ABC formalism described in [2]. It is also interesting to mention that the ABCs implicitly enforced by the DIT1 method are the continuity of $P_{c,z}$ and $\partial_x P_{c,z}$ at the interfaces. These in general are inconsistent with the microstructure of the material because one should have $\partial_x P_{c,z}\big|_{diel} = 0$ and $P_{c,z}\big|_{diel} = 0$ at the dielectric side of the boundary rather than the continuity of $P_{c,z}$ and $\partial_x P_{c,z}$.

IV.5. Concluding Remarks

In this Chapter, it was argued that the knowledge of the bulk electromagnetic response of a spatially dispersive material is insufficient to characterize the response to a macroscopic external excitation in presence of interfaces, even in simple scenarios where the geometry of the interfaces is trivial. It was highlighted that the partial differential equations that link $\mathbf{D}$ and $\mathbf{E}$, obtained by inverse Fourier transforming the constitutive relations in the spectral domain, may not hold across a boundary between two different materials, and that it is possible to link $\mathbf{D}$ and $\mathbf{E}$ through inequivalent differential equations over the interfaces, but which are totally consistent in the bulk regions. The correct form of the differential equations across the boundary can only be determined based on the knowledge of the internal structure of the metamaterial. It was illustrated how this can be done in practice for the particular case of a double wire medium, and a general FDFD-SD approach was developed to accurately characterize the electromagnetic response of spatially dispersive wire medium bodies with arbitrary geometries.

References

[1] V. Agranovich and V. Ginzburg, *Spatial Dispersion in Crystal Optics and the Theory of Excitons*, Willey-Interscience, New York, 1966.

[2] M. G. Silveirinha, C. A. Fernandes, and J. R. Costa, “Additional boundary condition for a wire medium connected to a metallic surface,” *New J. Phys.* **10**, 053011, 2008.

[3] M. G. Silveirinha, “Additional boundary conditions for nonconnected wire media,” *New J. Phys.* **11**, 113016, 2009.

[4] S. I. Maslovski, T. A. Morgado, M. G. Silveirinha, C. S. R. Kaipa, and A. B. Yakovlev, “Generalized additional boundary conditions for wire media,” *New J. Phys.* **12**, 113047, 2010.

[5] Y. Zhao, P. A. Belov, and Y. Hao, “Spatially dispersive finite-difference time-domain analysis of sub-wavelength imaging by the wire medium slabs,” *Opt. Express* **14**, 5154, 2006.

[6] Y. Zhao, P. A. Belov, and Y. Hao, “Modelling of wave propagation in wire media using spatially dispersive finite-difference time-domain method: numerical aspects,” *IEEE Trans. Antennas and Propag.* **55**, 1506, 2007.

[7] Y. Zhao, P. A. Belov, and Y. Hao, “Subwavelength internal imaging by means of a wire medium,” *J. Opt. A: Pure Appl. Opt.* **11** 075101, 2009.

[8] S. Raza, G. Toscano, Antti-Pekka Jauho, M. Wubs, and N. A. Mortensen, “Unusual resonances in nanoplasmonic structures due to nonlocal response,” *Phys. Rev. B* **84***,* 121412(R), 2011.

[9] G. Toscano, S. Raza, Antti-Pekka Jauho, N. A. Mortensen, and M. Wubs, “Modified field enhancement and extinction by plasmonic nanowire dimers due to nonlocal response,” *Opt. Express* **20**, 4176, 2012.

[10] J. M. McMahon, S. K. Gray, and G. C. Schatz, “Nonlocal optical response of metal nanostructures with arbitrary shape,” *Phys. Rev. Lett.* **103**, 097403, 2009.

[11] M. McMahon, S. K. Gray, and G. C. Schatz, “Calculating nonlocal optical properties of structures with arbitrary shape,”*Phys. Rev. B* **82**, 035423, 2010.

[12] C. David and F. J. G. de Abajo, "Spatial nonlocality in the optical response of metal nanoparticles," *J. Phys. Chem. C* **115**, 19470, 2011.

[13] P. A. Belov, R. Marqués, S. I. Maslovski, I. S. Nefedov, M. G. Silveirinha, C. R. Simovski, and S. A. Tretyakov, "Strong spatial dispersion in wire media in the very large wavelength limit," *Phys. Rev. B* **67**, 113103, 2003.

[14] G. Shvets, A. K. Sarychev, and V. M. Shalaev," Electromagnetic properties of three-dimensional wire arrays: photons, plasmons, and equivalent circuits," *Proc. SPIE* **5218**, 156, 2003.

[15] C. R. Simovski and P. A. Belov, "Low-frequency spatial dispersion in wire media," *Phys. Rev. E* **70**, 046616, 2004.

[16] M. G. Silveirinha, "Design of linear-to-circular polarization transformers made of long densely packed metallic helices," *IEEE Trans. Antennas Propag.* **56**, 390, 2008.

[17] M. G. Silveirinha, C. A. Fernandes, and J. R. Costa, "Superlens made of a metamaterial with extreme effective parameters," *Phys. Rev. B* **78**, 195121, 2008.

[18] M. G. Silveirinha, C. R. Medeiros, C. A. Fernandes, and J. R. Costa, "Experimental verification of broadband superlensing using a metamaterial with an extreme index of refraction," *Phys. Rev. B* **81**, 033101, 2010.

[19] R. A. Shelby, D. R. Smith, and S. Schultz, "Experimental verification of a negative index of refraction," *Science* **292**, 77, 2001.

[20] M. G. Silveirinha and C. A. Fernandes, "Nonresonant structured material with extreme effective parameters," *Phys. Rev. B* **78**, 033108, 2008.

[21] J. Yao, Z- Liu, Y. Liu, Y. Wang, C. Sun, G. Bartal, A. M. Stacy, and X. Zhang, "Optical negative refraction in bulk metamaterials of nanowires," *Science* **321**, 930, 2008.

[22] Y. Liu, G. Bartal, and X. Zhang, "All-angle negative refraction and imaging in a bulk medium made of metallic nanowires in the visible region," *Opt. Express* **16**, 15439, 2008.

[23] G. Shvets, S. Trendafilov, J. B. Pendry, and A. Sarychev, "Guiding, focusing, and sensing on the subwavelength scale using metallic wire arrays" *Phys. Rev. Lett.* **99**, 053903, 2007.

[24] T. A. Morgado, J. S. Marcos, M. G. Silveirinha, and S. I. Maslovski, "Ultraconfined interlaced plasmons," *Phys. Rev. Lett.* **107**, 063903, 2011.

[25] M. G. Silveirinha, “Anomalous dispersion of light colors by a metamaterial prism,” *Phys. Rev. Lett*. **102**, 193903, 2009.

[26] S. I. Maslovski and M. G. Silveirinha, “Nonlocal permittivity from a quasistatic model for a class of wire media” *Phys. Rev. B* **80**, 245101, 2009.

[27] M. G. Silveirinha and C. A. Fernandes, ” Homogenization of 3d- connected and non- connected wire metamaterials,” *IEEE Trans. on Microw. Theory and Tech.* **53**, 1418, 2005.

[28] S. D. Gedney, “An anisotropic perfectly matched layer-absorbing medium for the truncation of FDTD lattices,” *IEEE Trans. Antennas Propagat.* **44**, 1630, 1996.

[29] M. G. Silveirinha and S. I. Maslovski, “Radiation from elementary sources in a uniaxial wire medium,” *Phys. Rev. B* **85**, 155125, 2012.

[30] CST Microwave Studio Suite$^{\mathrm{TM}}$ 2010, (http://www.cst.com).

V. Applications of Double Wire Media

V.1. Introduction

The discussion of Chapter IV was mainly focused on the correct manner of discretizing the constitutive relations at a boundary and therefore, the geometries considered in the examples of Secs. IV4.1 and IV4.2 were quite elementary. Due to this reason, the considered problems also admit an analytical solution based on mode matching and additional boundary conditions. However, one of the key features of the FDFD-SD (IDF) approach developed in Chapter IV is that it also enables to obtain the solution of scattering and waveguiding problems in scenarios wherein electromagnetic waves interact with complex arbitrary shapes of spatially dispersive bodies. Typically, such problems cannot be solved using analytical methods.

In this Chapter, the FDFD-SD (IDF) implementation derived in Chapter IV will be used in order to investigate some interesting applications of double wire media bodies with complex arbitrary geometries.

First, in order to further validate the FDFD-SD (IDF) implementation, the imaging of a superlens formed by an ultradense array of crossed metallic wires is studied.

Next, the possibility of concentrating the electromagnetic field in a narrow spot by tapering a double wire medium waveguide is discussed.

Finally, based on the fact that the effective response of the double wire medium can be characterized by a low-loss anomalous refractive index in the visible domain, the design of an achromatic lens is proposed. It is theoretically and numerically shown that the proposed lens nearly eliminates the chromatic aberrations inherent to single-material glass lenses, and that such a metamaterial based lens may be an interesting alternative to the conventional achromatic doublets.

As in Chapter IV, in all the examples reported here, the propagation is assumed to be in the *xoy* plane with $\partial_z = 0$ $(k_z = 0)$, and that the electric field is polarized along the *z*-direction.

V.2. Superlensing with a Double Wire Medium Slab

In what follows, the imaging of a source by a metamaterial slab with finite width is investigated (inset of Fig. 5.1a). Previous works [1-3] have shown that a high-index dielectric material can be used as a lens that enhances the near field and the subwavelength details, and thus enables a superlensing effect. In Refs. [1, 2] it was theoretically suggested and experimentally verified that an ultradense array of crossed metallic wires may have a large index of refraction, and that it may support highly confined modes with very short propagation wavelengths, which when excited by a source permit restoring the subwavelength spatial spectrum of the source. Next, the imaging properties of the double wire medium are studied based on the FDFD-SD (IDF) discretization.

A double wire medium with thickness $L = 10a$ is considered in the near field of an electric line source placed at a distance $d_1 = 0.04\lambda_0$ above the metamaterial (inset of Fig. 5.1a). The radius of the wires is $r_w = 0.05a$ and the normalized frequency of operation is $\omega L / c = 0.3$. It is assumed that the wires are PEC and stand in air. The width of the slab along the y-direction is $w = 1.2\lambda_0$.

Figure 5.1a shows the normalized electric field profile at a distance $d_2 = d_1$ below the lens calculated using the FDFD-SD method (star shaped orange symbols), and Fig. 5.1b shows the associated electric field density plot. The predicted half power beamwidth (HPBW) is $0.13\lambda_0$, which is nearly four times smaller than the traditional diffraction limited value. In the absence of the metamaterial lens, and for the same propagation distance ($d_1 + d_2$) in the air region the HPBW would be $0.32\lambda_0$, which clearly confirms that the metamaterial lens can restore the subwavelength details of the source and compensate for the evanescent decay in the air regions. The electric field profile was also calculated using an analytical model (solid curve in Fig 5.1a) based on a Sommerfeld-type integral (see Ref. [1] for details). The analytical method assumes that the metamaterial slab has infinite width w along the y-direction. As seen in Fig. 5.1a, the results obtained with the analytical model concur well with the FDFD-SD simulations.

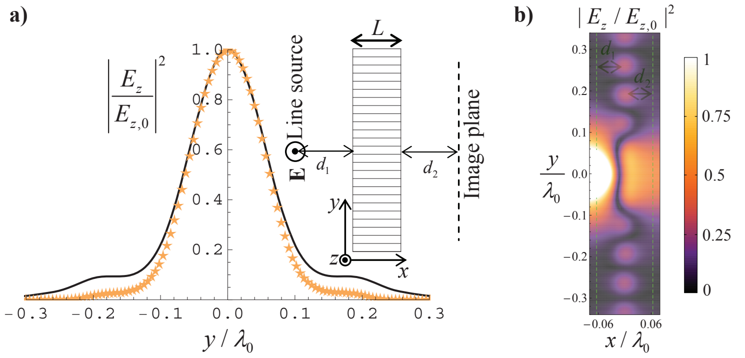

Fig. 5.1. (a) Amplitude of the normalized squared electric field imaged by a metamaterial lens with $L = 0.3\lambda_0 / 2\pi$, $a = L/10$ and $r_w = 0.05a$ (see the inset). Solid curve: analytical model (Ref. [1]). Star shaped orange symbols: FDFD-SD method. (b) Density plot of the normalized electric field for the scenario of panel (a).

In Ref. [J.1] it was also shown that this metamaterial lens can discriminate two sources separated by a distance nearly two times inferior to the diffraction limit.

V.3. Concentrating the Electromagnetic Field with a Tapered Waveguide

V.3.1. Introduction

It is known that by tapering plasmonic waveguides it may be possible to slow down and ultimately stop the light [4, 5, 6], and therefore concentrating the electromagnetic energy in the nanoscale [4, 7]. Next, it is shown that by tapering a double wire medium waveguide the magnetic field may be significantly enhanced toward the tip of the waveguide.

V.3.2. Guided Modes in a Subwavelength Waveguide

To begin with, the FDFD-SD (IDF) implementation is used to characterize the guided modes supported by an ultra dense array of metallic wires [8].

Figure 5.2a shows the dispersion characteristic of the transverse electric (TE) surface wave modes supported by a dense array of PEC wires for different lattice constants a. The discrete star-shaped symbols were calculated using the FDFD-SD method and the solid curves were obtained using an analytical method based on mode matching and additional boundary conditions [8]. Note that the analytical method assumes an infinite waveguide along the y-direction. The dispersion of the guided modes is determined with the FDFD-SD method as follows: For each wavelength of operation (λ_0) the metamaterial slab is excited by an electric line source placed within the waveguide. Then, the guided wavelength λ_g is determined by inspection of the real part of the electric field along the central line of the metamaterial slab (i.e. along the direction of propagation) at a distance sufficiently large (about $0.2\lambda_0$) from the source. The effective index of refraction seen by the guided mode is $n_{eff} = \lambda_0 / \lambda_g = k_y c / \omega$. Consistent with Ref. [8], Fig. 5.2a, shows that the metamaterial supports extremely subwavelength guided modes characterized by a large effective index of refraction $n_{eff} = k_y c / \omega$. Moreover, the index of refraction of a guided mode increases as the lattice constant a decreases, i.e., as the density of wires increases for a fixed metal volume fraction. The agreement between the results predicted by the numerical method and the analytical model of Ref. [8] is excellent. Figure 5.2b shows a time snapshot of the electric field in the *xoy* plane for a double wire medium waveguide with lattice constant $a = L/20$ at the normalized frequency of operation $\omega L/c = 0.1$. As seen, the guided mode is strongly confined to the waveguide, in agreement with the fact that the effective index of refraction is $n_{eff} = 6$ (Fig. 5.2a).

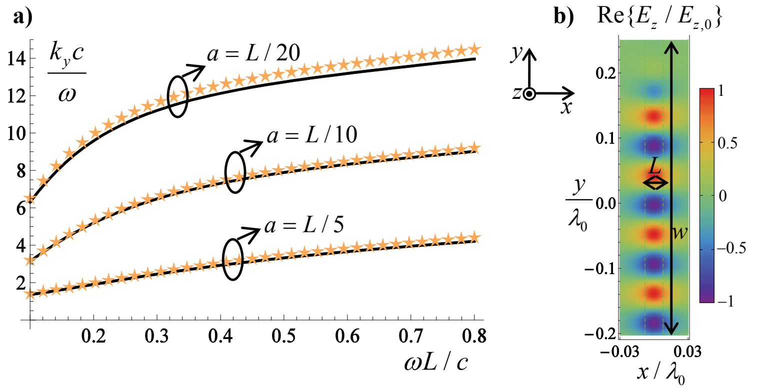

Fig. 5.2. Normalized propagation constant k_y of the TE-guided modes as a function of frequency, for a fixed thickness L of the metamaterial formed by PEC wires, and different lattice constants a. The radius of the wires is $r_w = 0.05a$ and the wires stand in a vacuum. Solid curve: analytical model (Ref. [8]). Star shaped (orange) symbols: FDFD-SD method. (b) Time snapshot of E_z (in arbitrary unities) at the frequency $\omega L/c = 0.1$ when a waveguide with $a = L/20$ is excited by an electric line source positioned at $(0, -0.2\lambda_0)$.

V.3.3. Cascaded Waveguides: Impedance Matching Condition

In this subsection, it is discussed how the waveguide analyzed in Sec. V.3.2 can be tapered so that the guided electromagnetic energy can be concentrated in an ultra-subwavelength region.

Let us start by considering two cascaded waveguides with thickness L and $L_2 = 0.6L$, respectively (Fig. 5.3a). Since there is an abrupt transition, a matching condition for the two waveguides must be derived, so that one can ensure a good transmission at the junction. To this end, a transmission line analogy is considered, so that each waveguide is associated with a voltage V_i, a current I_i and an impedance Z_i $(i = 1,2)$. To a first approximation, the field component H_y is proportional to the microscopic current flowing in the metallic wires, and thus it should vanish at the interfaces. Thus, from the point of view of the waves *inside* the waveguide, the interfaces with air may be regarded as magnetic walls (PMC). Hence, the guided mode is expected to be quasi-transverse electromagnetic (quasi-TEM) with respect to the direction of propagation (*y*-direction), and that the relevant field components are E_z and H_x. Moreover, the following correspondences can be established:

$$V \sim H_x L, \tag{5.1a}$$

$$I \sim E_z, \tag{5.1b}$$

$$Z \sim \frac{H_x}{E_z} L, \tag{5.1c}$$

where *L* is the thickness of the metamaterial slab along the *x*-direction. Notice that *V* is associated with H_x and *I* with E_z because a waveguide with PMC walls is the electromagnetic dual of a standard waveguide with PEC walls. On the other hand, for a TE mode, $H_x \sim \frac{\partial E_z}{\partial y}$ and hence the fields inside the waveguide also satisfy:

$$\frac{H_x}{E_z} \sim k_y. \tag{5.2}$$

From Eqs. (5.1c) and (5.2) it follows that to keep the impedance constant in the two waveguides, and thus ensure a good matching at the transition, one should guarantee that:

$$k_y L = const. \tag{5.3}$$

Figure 5.3a shows a density plot of the normalized electric field for a metamaterial waveguide similar to that of Fig. 5.2a ($a = L/20$) in cascade with another waveguide with thickness $L_2 = 0.6L$. The frequency of operation is $\omega L / c = 0.25$. The lattice constant a_2 of the second waveguide is determined so that Eq. (5.3) is satisfied, i.e, that $k_y L = k_{y,2} L_2$, where k_y and $k_{y,2}$ represent the wave numbers in the waveguide with thickness L and L_2, respectively. This can be done by using the analytical model of Ref. [8], provided $k_{y,2}$ and L_2 are known. The density plot of Fig. 5.3a shows that the electric field amplitude is kept nearly constant across the junction of the two waveguides, indicating a good matching. This result is confirmed in Fig. 5.3b, where the profile of the normalized electric field along the central line of the waveguide is depicted (solid blue curve). It can be seen that despite the abrupt transition, the wave is barely reflected. In contrast, the dashed green curve is obtained without ensuring the impedance match, (specifically the lattice constant a_2 is tuned so that $k_y = k_{y,2}$), and in this case a standing wave pattern with a much stronger modulation is obtained.

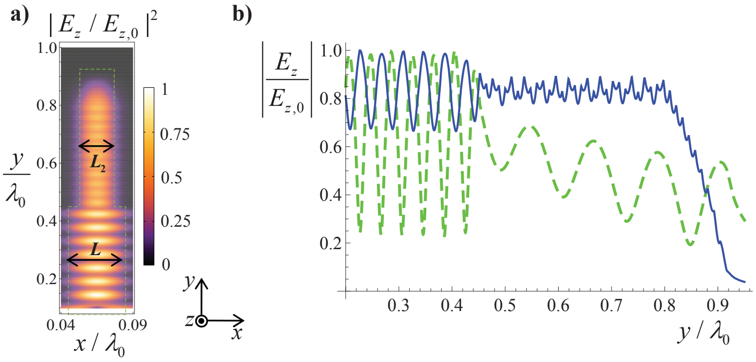

Fig. 5.3. (a) normalized $|E_z|^2$ in the vicinity of two cascaded double wire medium waveguides with thicknesses L and $L_2 = 0.6L$, at the frequency of operation $\omega L / c = 0.25$. The fields were obtained using the FDFD-SD full wave simulator. (b) Profile of the square normalized electric field along the central line of the waveguide. Solid blue curve: the lattice constant in the second waveguide region is tuned so that the impedance matching condition (Eq. (5.3)) is satisfied; Green dashed curve: the lattice constant in the second waveguide region is tuned so $k_y = k_{y,2}$.

V.3.4. Tapered Waveguide

In this subsection, the theory derived in Sec. V.3.3 is used to investigate the waveguiding by a tapered metamaterial slab formed by PEC wires with initial thickness L_i, that is first tapered toward a tip with thickness $L_f = 0.2L_i$, and then expanded towards its original thickness L_i (inset of Fig. 5.4a). The taper profile is linear and the distance between the points with thickness L_i and L_f is $0.45\lambda_0$. The thickness of the waveguide is defined as position-dependent function such that $L_{wg} \equiv L_{wg}(y)$. The frequency of operation is $\omega L_i / c = 0.25$ and the lattice constant at the beginning of the waveguide is $a_i = L_i/13$.

Figure 5.4a shows the effective index of refraction $n_{wg} \equiv k_{y,wg} c/\omega$ seen by the guided mode toward the tip of the waveguide, where $k_{y,wg} \equiv k_{y,wg}(L_{wg})$ is the wave number along the y-direction determined so that Eq. (5.3) is satisfied for each L_{wg}. As expected, n_{wg} increases significantly as the tip is approached. In Fig. 5.4b the lattice constant a_{wg} is depicted as a function of the thickness of the waveguide. In the same manner as in Fig. 5.3, for each L_{wg} the lattice constant a_{wg} is determined so that $k_{y,wg}$ satisfies the matching condition [Eq. (5.3)]. Figure 5.4c shows a density plot of the normalized electromagnetic fields along the waveguide. Consistent with the results reported in Fig. 5.3, the electric field remains essentially constant along the waveguide, despite the tapering. This is further supported by Fig. 5.4d, which shows the normalized electric field profile (solid blue curve) along the axis of the waveguide. The ripple observed in the electric field profile in the vicinity tip may be related to numerical imprecision, as near the tip the guided wavelength is extremely small, and thus a very refined mesh is required to obtain fully converged results. In contrast, both components of the magnetic field are strongly enhanced as the tip is approached, indicating that tapering the metamaterial waveguide permits concentrating the magnetic field into a subwavelength spot (Fig. 5.4c). This also shown in the inset of Fig. 5.4d, which depicts H_x / H_y (black curve) and $H_x / H_{x,1}$ (green curve) along the axis of the waveguide, where $H_{x,1}$ is the amplitude of the x-component of the magnetic field in a waveguide with constant thickness $L = L_i$. It is evident that H_y is nearly negligible as compared to H_x (black curve), indicating, indeed, quasi-TEM propagation, in agreement with the initial assumption. Moreover, H_x is enhanced about five times with respect to a waveguide with constant thickness $L = L_i$ (green curve), which is consistent with the fact that $L_f / L_i = 5$.

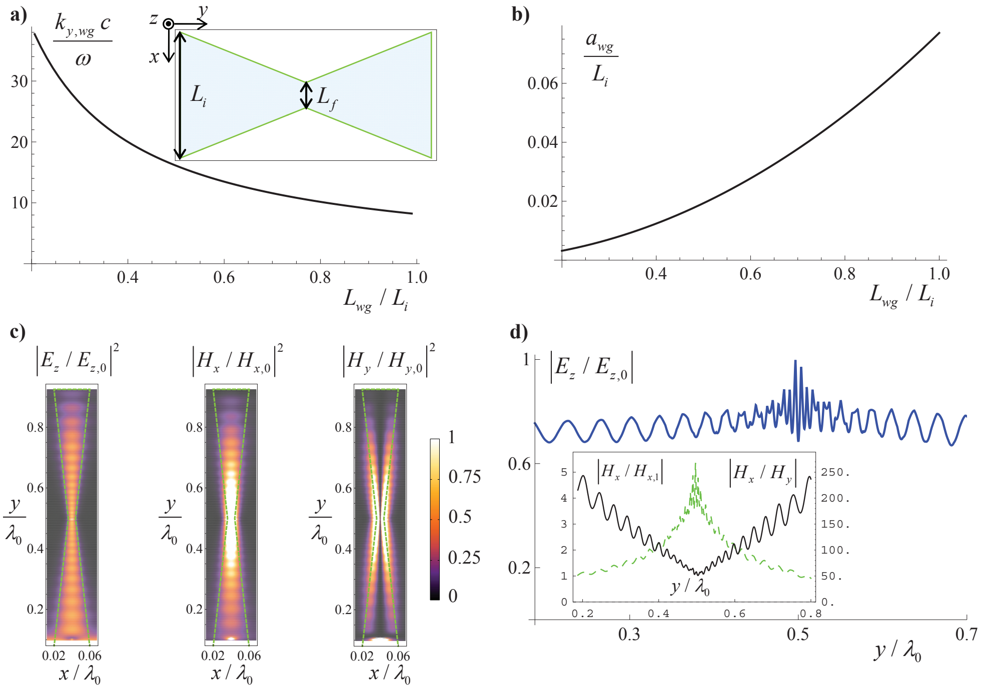

Fig. 5.4. (a) y-component of the guided wave number $k_{y,wg}$ (calculated using Eq. (5.3)) as a function of the normalized thickness of the tapered metamaterial waveguide. The geometry of the waveguide is shown in the inset. (b) Normalized lattice constant a_{wg} as a function of the thickness of the waveguide. (c) Normalized $|E_z|^2$, $|H_x|^2$ and $|H_y|^2$ in the vicinity of the tapered waveguide. (d) Profile of the normalized electric field along the central line of the waveguide. The inset shows the profile of H_x / H_y along the central line of the waveguide (solid blue curve) and H_x normalized to the amplitude of the x-component of the magnetic field in a waveguide with constant thickness $L = L_i$.

In Ref. [J.1] it was further shown that if a double wire medium waveguide is tapered and severed at the tip, the electric field is nearly constant along the waveguide and both components of the magnetic field are greatly enhanced. Also in this scenario, the enhancement of the magnetic field is roughly inversely proportional to the compression of the waveguide.

V.4. Suppression of Chromatic Aberrations

V.4.1. Introduction

Conventional optical single-material glass lenses are unable to focus all the spectral components of light into the same convergence point, even in ideal circumstances where the effects of diffraction are negligible. The reason for this limitation is the frequency dispersion of the glass refractive index, which causes wavelengths associated with different colors to be refracted differently [9]. Hence the image produced by a glass lens may be distorted, and in such a case the optical system is said to suffer from chromatic aberrations. The material dispersion is manifested in the form of beautiful rainbows when white light is separated into its spectral components by a glass prism [10], and is rooted in fundamental physical restrictions, stemming from the causality and passivity of the dielectric response. Causality and passivity determine that the index of refraction of any conventional low-loss dielectric material is a strictly increasing function of frequency [11].

Since the optical path length of a given ray in an optical system, $\Psi = n_1 l_1 + ... + n_N l_N$, is written in terms of the indices of refraction (n_i) of the involved materials, the correction of chromatic aberrations is a non-trivial problem. Indeed, the material dispersions are combined additively, and since $\dot{n}_i \equiv dn / d\omega > 0$, it follows that Ψ is a strictly increasing function of frequency. Nevertheless, several strategies to minimize the effect of chromatic aberrations are well documented in the literature and are typically based on the combination of materials with different positive dispersion (e.g. [12-15]). This is possible because the system can be designed so that the trajectories of the rays inside the lens change with frequency in such a manner that the profile of Ψ at the exit surface is invariant (apart from the sum of an irrelevant constant). Lenses with reduced aberrations are known as achromatic doublets.

The definition of Ψ suggests that the effects of material dispersion in glass ($\dot{n}_g > 0$) may be easier to suppress if a material with anomalous dispersion ($\dot{n}_{xw} < 0$) is available. However, the aforementioned restrictions stemming from Kramers-Kronig relations for causal and passive dielectric media [11], indicate that a regime of anomalous dispersion implies very significant loss, and hence this solution seems to be impractical. The question remains: is it possible to overcome this limitation?

In Chapter IV (Sec. IV.4.1) it was briefly mentioned that the double wire medium may enable the realization of a dielectric response with broadband anomalous dispersion [16, 17] in the visible domain, such that $\dot{n}_{xw} < 0$. Such a property stems from the strong spatially dispersive nature of the metamaterial, where the restrictions on the dispersion of the index of refraction for this class of media are less strict than for conventional dielectrics. Here, it is theoretically demonstrated that such a metamaterial may permit reducing significantly the chromatic aberration of a conventional thin glass lens.

V.4.2. Ray Optics in Thin Compound Lenses

To begin with, a thin compound lens formed by two materials is considered. The refracting surfaces at the air interfaces have radius of curvature R_1 and R_2. The adopted convention is that R_1 and R_2 are positive for convex surfaces (seen from the air region), and it is assumed that the *i-th* (*i=1,2*) refracting material is associated with a material with index $n_i(\omega)$ (Fig. 5.5a).

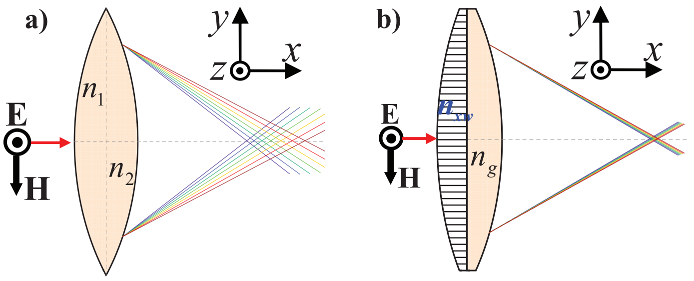

Fig. 5.5. (a) Illustration of the chromatic aberration of a conventional thin biconvex glass lens with parameters $n_1 = n_2 = n_g(\omega)$. (b) Biconvex optical metamaterial lens that corrects the chromatic aberration for all the colors of light; the compound lens is formed by a thin plano-convex glass lens coated with a thin plano-convex double wire medium.

Since the radii of conventional optical lenses have physical sizes that correspond to tens or even hundreds of wavelengths of the visible spectrum, geometrical optics may be used to describe how light propagates in such optical systems. For a thin compound lens standing in air, the focal length satisfies the well-known Lensmaker's equation [9]:

$$\frac{1}{f} = (n_1 - 1)\frac{1}{R_1} + (n_2 - 1)\frac{1}{R_2}. \tag{5.4}$$

For a thin lens, the distances S_1 and S_2, from the object and focal plane to the lens, respectively, satisfy $\frac{1}{f} = \frac{1}{S_1} + \frac{1}{S_2}$. Obviously, a lens formed by a single material (let's say glass), has focal length such that $\frac{1}{f} = (n_g - 1)\left(\frac{1}{R_1} + \frac{1}{R_2}\right)$, where $n_g = \sqrt{\varepsilon(\omega)}$ is the refractive index of the glass. Since the permittivity $\varepsilon(\omega)$ of glass is an increasing function of frequency in the optical domain [11], it is manifest from Eq. (5.4) that the focal length f of the lens is a decreasing function of frequency. Therefore, the focusing provided by the biconvex lens of Fig. 5.5a is imperfect, as the colors of light associated with longer wavelengths ("red" light) are less refracted by the optical system, converging to a longitudinal point farther than the components of light associated with shorter wavelengths ("violet" light). The change δf in the focal length caused by a change Δn_g in the refractive index of the glass is the chromatic aberration.

For a compound lens it can be assumed to a first approximation that both n_1 and n_2 vary linearly with frequency so that $n_1 \approx n_{10} + \dot{n}_1 (\Delta\omega)$ and $n_2 \approx n_{20} + \dot{n}_2 (\Delta\omega)$ where $\dot{n}_1 = dn_1 / d\omega$, $\dot{n}_2 = dn_2 / d\omega$, $\Delta\omega = \omega - \omega_0$, and that ω_0 is some reference frequency at which the lens is designed (and for which $n_1 = n_{10}$ and $n_2 = n_{20}$). Then, using Eq. (5.4), it is easily found that the optical power of the bi-layer lens can be made independent of frequency provided [12]:

$$\dot{n}_1 = -\frac{R_1}{R_2}\dot{n}_2. \tag{5.5}$$

From the above formula it is manifest that the correction of the chromatic aberrations can be achieved by considering two materials with positive dispersion (when $\dot{n}_1$ and $\dot{n}_2$ are both positive) and such that the radii of curvature of two refracting surfaces have opposite signs. This is the conventional solution that is the basis of achromatic doublets and that has been used for decades [12].

Let us now go the other way around and consider that the thin lens is instead formed by two convex refracting surfaces, i.e. R_1 and R_2 are positive. In such a scenario, in order to satisfy the condition (5.5) a material with anomalous dispersion is required, because $\dot{n}_1$ and $\dot{n}_2$ must have opposite signs. To the best of our knowledge, this solution has not been seriously considered before because regimes of anomalous dispersion in conventional materials imply very significant loss. Here, it is shown that the double wire medium takes that solution to the *realm* of reality. For this case it is assumed that $n_1 = n_{xw}(\omega)$ and $n_2 = n_g(\omega)$, being $n_{xw}(\omega)$ the effective index of refraction of the metamaterial. Hereafter, a lens that satisfies Eq. (5.5) with $\dot{n}_{xw} < 0$ will be referred to as *compensated* biconvex lens.

V.4.3. Low Loss Broadband Anomalous Dispersion

In the previous Chapter it was shown that in the considered scenario i.e., propagation in the *xoy* plane with $k_z = 0$ and $\mathbf{E} = E_z \hat{\mathbf{u}}_z$, the double wire medium is characterized by the dielectric function $\varepsilon(\omega, k_x)$ given by Eq. (4.7). Here it is assumed that the wires stand in air, i.e., $\varepsilon_h = 1$. The effective index of refraction, $n_{xw} = ck_x / \omega$ of the metamaterial is found by solving the dispersion equation $k_x^2 = (\omega / c)^2 \varepsilon(\omega, k_x)$ with respect to k_x. This yields:

$$n_{xw} = \sqrt{\frac{3}{2} - \left(\frac{\beta_p c}{\omega}\right)^2 \beta_m + \sqrt{\frac{1}{4} + (2 - \beta_m)\left(\frac{\beta_p c}{\omega}\right)^2 + \beta_m^2 \left(\frac{\beta_p c}{\omega}\right)^4}}, \tag{5.6}$$

where $\beta_m = 1 / [(\varepsilon_m - 1) f_V]$. In the particular case of perfectly conducting wires ($\varepsilon_m = -\infty$), the index of refraction reduces to $n_{xw} = \sqrt{\frac{3}{2} + \frac{1}{2}\sqrt{1 + 8\left(\frac{\beta_p c}{\omega}\right)^2}}$, which is clearly a decreasing function of frequency [17], since β_p is a parameter that depends merely on the geometry of the metamaterial. This property still holds for realistic metals at optical frequencies. This is illustrated in Fig. 5.6, where $n_{xw} = n'_{xw} + i n''_{xw}$ is ploted as a function of frequency for Al nanowires modeled by a Drude dispersion model with parameters consistent with experimental data reported in the literature [18]. It is seen that the metamaterial is characterized by low-loss broadband anomalous dispersion in the entire visible domain.

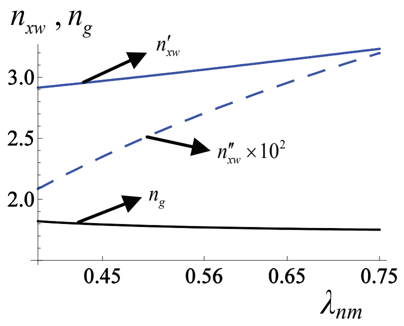

Fig. 5.6. Refractive indices of dense flint glass SF10 (black curve) and of the nanowire metamaterial (blue curves).

It is curious to mention that notwithstanding that at the "microscopic level" all the constituents (host and inclusions) of the metamaterial satisfy $\dot{n} > 0$, the effective medium is characterized by $\dot{n}_{xw} < 0$ due to the complex electromagnetic interactions between its different elements. In particular, the optical path length of a wave that transverses a metamaterial slab decreases with frequency, whereas a naïve application of the formula $\Psi = n_1 l_1 + ... + n_N l_N$ (with n_i standing either for the inclusions or for the host) would suggest the opposite. This apparent contradiction is explained by the fact that the formula $\Psi = n_1 l_1 + ... + n_N l_N$ is not valid when the distance between the different materials is small on the scale of the wavelength, because in such conditions the wave envelope is described by an effective index of refraction, which is not a simple average of those of the constituent materials. In some sense, in a nanowire metamaterial the sum of many positives ($\sum_i l_i \dot{n}_i > 0$) can yield a negative optical path length ($\dot{n}_{xw} \sum_i l_i < 0$).

V.4.3.1 Metamaterial Prism

In order to further confirm that the effective refractive index of the double wire medium is a decreasing function of frequency in the optical domain, the refraction of a cylindrical Gaussian beam by a metamaterial prism with $\alpha = 14^\circ$ and aperture $W = 6\lambda_{0.75\mu m}$ is investigated using the FDFD-SD implementation. The metamaterial has lattice constant $a = 100nm$ and the nanowires have radius $r_w = 0.14a$. The beam waist of the incoming wave was taken equal to $2w_0 = 3.5\lambda_{0.75\mu m}$. Figures 5.7a, b and c show density plots of $|E_z|^2$ in the vicinity of the prism at $\lambda = 0.38\,\mu m$, $\lambda = 0.56\,\mu m$ and $\lambda = 0.75\,\mu m$, respectively, and support that shorter wavelengths are less refracted than longer wavelengths, confirming that the effective refractive index n_{xw} of the metamaterial prism is a decreasing function of frequency in the optical domain. The spectral electromagnetic fields associated with $\lambda = 0.38\,\mu m$, $\lambda = 0.56\,\mu m$ and $\lambda = 0.75\,\mu m$ [Figs. 5.7-a,b,c] can be blended and represented in a RGB color scale – taking into account the relative intensity of the fields for each wavelength – and this results in a reversed rainbow [Fig. 5.7d]. In Fig. 5.7e the angle of transmission, θ_t, is depicted as a function of frequency calculated with *(i)* the FDFD-SD code (black solid curve) *(ii)* the theoretical formula $\theta_t = \arcsin\left(n'_{xw} \sin\alpha\right)$ (blue dashed curve) [17]. It is seen that the results concur very well.

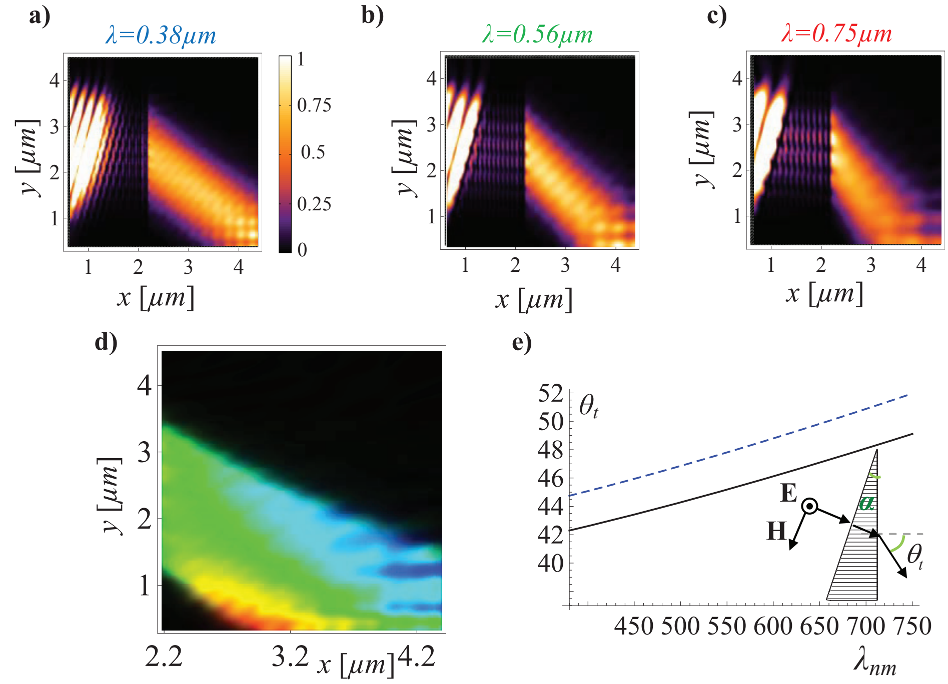

Fig. 5.7. Panels (a), (b) and (c): normalized $|E_z|^2$ in the vicinity of a metamaterial prism at: (a) $\lambda = 0.38\,\mu m$. (b) $\lambda = 0.56\,\mu m$. (c) $\lambda = 0.75\,\mu m$. (d) reversed rainbow obtained by blending the different light wavelengths [panels (a), (b) and (c)]. (e) transmission angle θ_t as a function of the wavelength $\lambda[\mu m]$ for a Gaussian beam that illuminates the prism along the normal direction. The blue dashed curve was obtained using the theoretical formula $\theta_t = \arcsin\left(n'_{xw} \sin\alpha\right)$ and the black solid curve was calculated using the full wave FDFD-SD implementation.

V.4.4. Achromatic Biconvex Metamaterial Lens

To illustrate how the considered metamaterial can, indeed, nearly eliminate the chromatic aberration of a single-material glass lens, the design of a compensated biconvex lens is considered, such that $f \sim 7.8\mu$m and $n_1 = n_{xw}$, $n_2 = n_g$. The nanowire material has the same parameters as in the previous example, except that the nanowires diameter is increased to $2r_w = 30nm$. It is assumed that the dielectric is a dense flint glass SF10. In the visible spectrum, the refractive index $n_g(\omega)$ of this glass is described to a first approximation by the so-called Cauchy's equation $n_g(\lambda_{\mu m}) = A + B/\lambda^2$ with $A = 1.7280$ and $B = 0.01342[\mu m^2]$ [19]. At the central frequency of the visible spectrum ($\omega_0/2\pi$=595[THz]), it is possible to estimate $\dot{n}_{xw} = -0.89\times10^{-3}\left[THz\right]^{-1}$, $\dot{n}_g = 0.18\times10^{-3}\left[THz\right]^{-1}$, $n_{xw0} = 3.01$, and $n_{g0} = 1.78$. Hence, from Eqs. 5.4 and 5.5 it follows that the radius of curvature of the first and second interfaces is $R_1 = 46.24\mu$m and $R_2 = 9.25\mu$m, respectively. The central thickness of the two layers is taken $d_1 = 0.26\mu m$ and $d_2 = 1.31\mu m$.

To have a reference against which the performance of the compensated biconvex lens can be compared, let us consider as well an ordinary single material plano-convex lens ($R_1 = \infty$) made exclusively of glass ($n_1 = n_2 = n_g$), and with the same optical power as the compensated lens (i.e. $1/f$ is invariant). This requires that the radius of curvature R_{2s} of the convex surface is taken equal to: $R_{2s} = R_2\left(\left|\frac{\dot{n}_g}{\dot{n}_{xw}}\right|\frac{n_{xw0}-1}{n_{g0}-1}+1\right)^{-1} = 6.09\mu m$. The central thickness of the single-material lens is $d_{2s} = 1.31\mu m$. Figure 5.8a shows the electric field profile calculated along the mid-plane perpendicular to the single-material lens under the illumination of a cylindrical Gaussian beam. The dashed and solid curves in Fig. 5.8a were obtained using a commercial full-wave electromagnetic simulator [20] and a FDFD code, respectively. The FDFD code predicts that the chromatic aberration δf (defined with respect to the central frequency ω_0) at $\lambda = 0.75 \mu m$ and $\lambda = 0.38 \mu m$, is $\delta f \approx 0.26[\mu m]$ and $\delta f \approx -0.37[\mu m]$ (Fig. 5.8a), respectively.

The achromatic biconvex metamaterial lens performs far better than the ordinary lens. Figure 5.8b shows a density plot of $|E_z|^2$ obtained with the FDFD-SD code at $\lambda = 0.75 \mu m$ in the vicinity of the biconvex lens. The focal spot created by the lens under the illumination of a cylindrical Gaussian beam is evident. Figure 5.8c shows the electric field profile calculated along the mid-plane perpendicular to the biconvex lens. For this case, the FDFD-SD code predicts that the chromatic aberration at the wavelength $\lambda = 0.38 \mu m$ is drastically reduced to $\delta f \approx 0.052[\mu m]$, whereas the chromatic aberration associated with the wavelength $\lambda = 0.75 \mu m$ is reduced to $\delta f \approx -0.039[\mu m]$. Thus, the chromatic aberrations associated with the wavelengths at the edges of the visible spectrum are practically eliminated. This property is actually valid in the entire visible spectrum, as supported by Fig. 5.8d that shows the focal curve, i.e., the chromatic aberration δf as a function of the wavelength. The yellow stars were calculated using the FDFD-SD simulations whereas the yellow circles were obtained using the full-wave simulator taking into account all the minute details of the metamaterial [20]. It can be seen that the compensated lens permits focusing all the colors into the same convergence point. The diamond symbols in Fig. 5.8d represent the focal curve of the ordinary single-material glass lens of Fig. 5.8a, showing a significant chromatic aberration.

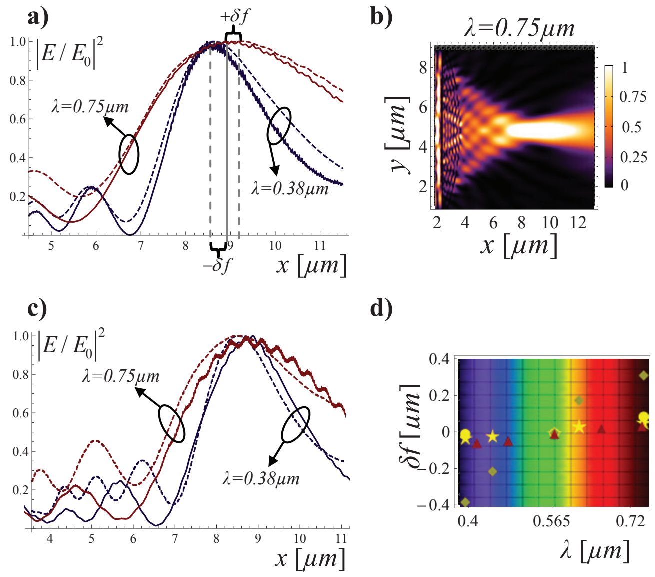

Fig. 5.8. Profile of the normalized squared electric field near the focal region of the single-material glass lens. Solid curves: obtained using Microwave Studio [20]. Dashed curves: obtained with the FDFD simulator. (b) normalized $|E_z|^2$ (obtained using the FDFD-SD full wave simulator) in the vicinity of the compensated biconvex metamaterial lens. (c) analogous to (a), but for the compensated biconvex metamaterial lens. (d) focal plane curve as a function of the wavelength. The yellow stars (FDFD-SD implementation and the yellow circles (Microwave Studio [20]) represent the position of the foci of the compensated metamaterial lens. The red triangles and the diamond symbols (FDFD) represent the focal curve of a conventional achromatic doublet and of the single-material lens, respectively.

It should be noted that Eq. (5.4) is based on the thin lens approximation, and thus even within the framework of geometrical optics it is not exact. To take this into account and provide a more robust correction of the chromatic aberrations, the parameters of the metamaterial in the FDFD-SD simulations of Fig. 5.8 were slightly adjusted so that $a \approx 94nm$ and $2r_w \approx 33nm$. Moreover, in the CST simulations of Fig. 5.8, the lattice constant of the nanowire material and the diameter of the wires were adjusted to $a \approx 123nm$ and $2r_w \approx 25nm$, in order to have a physical response more consistent with the homogenization model.

The performance of a standard doublet formed by a biconvex crown glass N-BK7 lens [21] and a concave-plane dense flint glass SF10 lens was also investigated. In this scenario, the doublet is formed by two materials with positive dispersion ($\dot{n}_1$ and $\dot{n}_2$ are both positive). Note that this achromat is not of the same type as that represented in

Fig. 5.5, wherein the middle interface is planar. Indeed, it was verified (not shown here) with both ray tracing and full wave simulations that the generic configuration of Fig. 5.5 is less effective in the correction of the aberrations when both materials have positive dispersion than the solution (based on biconvex and concave-plane layers) reported here (Fig. 5.9).

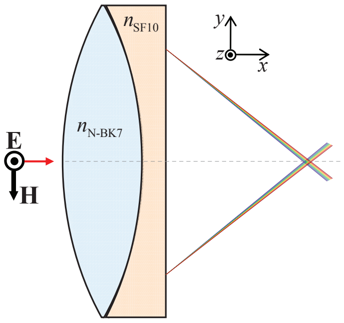

Fig. 5.9. Standard achromatic doublet based on biconvex and concave-plane layers.

In order that the optical power of the doublet is the same as that of the compensated lens, the radii of curvature of the first and second convex surfaces (N-BK7) were chosen $R_1 = 3.10\,\mu\text{m}$ and $R_2 = 9.25\,\mu\text{m}$, and the radius of curvature of the concave-plane surfaces (SF10) $R_3 = -8.11\,\mu\text{m}$ and $R_4 = \infty$. The central thicknesses of both glasses is $1\mu m$. The focal curve of this doublet is also represented in Fig. 5.8d (red triangles), showing a reduction of the chromatic aberration comparable to that of the compensated lens.

V.5. Concluding Remarks

The potentials of the FDFD-SD (ISD) implementation derived in Chapter IV were illustrated, and the simulator developed was used to analyze some interesting configurations of double wire media with complex shapes. Mainly for the sake of further validation of the FDFD-SD implementation, it was confirmed that a dense array of a double wire medium slab may behave as a near-field superlens.

The possibility of concentrating the electromagnetic fields at the tip of an ultra compact tapered waveguide formed by wire media was investigated, showing that this may be an exciting route for enhancing and focusing the magnetic field in a subwavelength spot.

Finally, and likely to be the most exciting application for the double wire medium proposed in this thesis, it was shown that based on the low-loss broadband anomalous material dispersion in the optical domain of the metamaterial, it is possible to design optical systems with performance nearly independent of the material dispersion. The level of aberrations obtained with the design reported in this work is of order of magnitude comparable to what is achievable with conventional achromats. Since by adjusting the composition and geometry of the metamaterial one can engineer the dispersion of n_{xw}, it is envisioned that despite the obvious technological challenges, an optimized structure may provide an exciting route for improved optical instruments insensitive to chromatic aberrations.

References

[1] M. G. Silveirinha, C. A. Fernandes, and J. R. Costa, “Superlens made of a metamaterial with extreme effective parameters,” *Phys. Rev. B* **78**, 195121, 2008.

[2] M. G. Silveirinha, C. R. Medeiros, C. A. Fernandes, and J. R. Costa, “Experimental verification of broadband superlensing using a metamaterial with an extreme index of refraction,” *Phys. Rev. B* **81**, 033101, 2010.

[3] J. Christensen and F. Javier García de Abajo, “Slow plasmonic slab waveguide as a superlens for visible light,” *Phys. Rev. B* **82**, 161103(R), 2010.

[4] M. I. Stockman, “Nanofocusing of optical energy in tapered plasmonic waveguides,” *Phys. Rev. Lett.* **93**, 137404, 2004.

[5] M. S. Jang and H. Atwater, “Plasmonic rainbow trapping structures for light localization and spectrum splitting,” *Phys. Rev. Lett.* **107**, 207401, 2011.

[6] K. L. Tsakmakidis, A. D. Boardman, and O. Hess, “'Trapped rainbow' storage of light in metamaterials,” *Nature (London)* **450**, 397, 2007.

[7] S. A. Maier, S. R. Andrews, L. Martín-Moreno, and F. J. García-Vidal, "Terahertz surface plasmon-polariton propagation and focusing on periodically corrugated metal wires," *Phys. Rev. Lett*. **97**, 176805, 2006.

[8] M. G. Silveirinha and C. A. Fernandes, "Nonresonant structured material with extreme effective parameters," *Phys. Rev. B* **78**, 033108, 2008.

[9] M. Born and M. Wolf, *Principles of Optics,* Cambridge University Press, 7th (expanded) ed, 1999.

[10] I. Newton, "A letter of Mr. Isaac Newton containing his new theory about light and colors," Phil. Trans R. S. **6**, 3075-3087, 1671.

[11] L. D. Landau, E. Lifshitz, and L. Pitaevskii, *Electrodynamics of Continuous Media* Elsevier Butterworth-Heinemann, Oxford, 2nd ed, 2004.

[12] T. T. Smith, "The color correction of an achromatic doublet," J. Opt. Soc. Am. & Review of Scientific Instruments **10**, 39-62, 1925.

[13] T. T. Smith, "The color correction of an achromatic doublet II," J. Opt. Soc. Am. & Review of Scientific Instruments **15**, 247-254, 1927.

[14] R. G. Treuting, "An achromatic doublet of silicon and germanium," J. Opt. Soc. Am. **41**, 454-455, 1951.

[15] M. Herzberger and N. R. McClure, "The design of superachromatic lenses," Appl. Opt. **2**, 553-560, 1963.

[16] M. G. Silveirinha and C. A. Fernandes, "Nonresonant structured material with extreme effective parameters," *Phys. Rev. B* **78**, 033108, 2008.

[17] M. G. Silveirinha, "Anomalous dispersion of light colors by a metamaterial prism," *Phys. Rev. Lett*. **102**, 193903, 2009.

[18] M. A. Ordal, R. J. Bell, R. W. Alexander, Jr., L. L. Long, and M.R. Querry, "Optical properties of fourteen metals in the infrared and far infrared: Al, Co, Cu, Au, Fe, Pb, Mo, Ni, Pd, Pt, Ag, Ti, V, and W," Appl. Opt. **24**, 4493-4499, 1985.

[19] F. A. Jenkins and H. E. White, *Fundamentals of Optics* McGraw-Hill, 4th ed, 1981.

[20] CST Microwave Studio Suite$^{\text{TM}}$ 2010, (http://www.cst.com).

[21] O. S. of America, *Handbook of Optics* McGraw-Hill Professional, vol. II, 2nd edition, 1994.

VI. Conclusions

VI.1. Main Results

This thesis was essentially devoted to the numerical modeling of nonlocal metamaterials based on effective medium theory. Relying on homogenization approaches, a metamaterial configuration characterized by a broadband DNG response was proposed, and the relation between microscopic and macroscopic quadratic forms like the Poynting vector was clarified. Furthermore, some exciting applications for the double wire medium were proposed.

In Chapter II, based on a previously proposed nonlocal homogenization formalism [1], an efficient and systematic FDFD numerical method that permits the extraction of the effective parameters of periodic arrangements of metallic/dielectric inclusions was suggested. In Sec. II.3.1, the effective parameters such as the nonlocal effective dielectric permittivity $\overline{\overline{\varepsilon_{\text{eff}}}}$ and the effective magnetic permeability $\overline{\overline{\mu_{\text{eff}}}}$ were extracted for several metamaterial configurations characterized by a quasi-local response. The proposed method was successfully compared against other homogenization techniques [2, 3]. In the second part of Chapter II (Sec. II.3.2), the effective response of a metamaterial configuration formed by horseshoe shaped plasmonic inclusions was analyzed. It was shown that due to the asymmetric shape of the inclusions, the bianisotropic effects must be taken into account to properly model the electromagnetic response of the metamaterial. Furthermore, it was demonstrated that this metamaterial is not only characterized by bianisotropy but by spatial dispersion as well.

In chapter III, a zero-index DNG metamaterial (Sec. II.3.1.3) was used to prove how it is possible to self-consistently define the Poynting vector and energy relations in metamaterials with local constitutive parameters, even when negative index of refraction or anomalous values of effective constitutive parameters are considered. It was proven from first-principles considerations based on the general theory derived in [4] that the correct definitions of Poynting vector, stored energy and heating rate in NIMs coincide with those in natural materials after properly defining macroscopic averaged fields and effective constitutive parameters. Moreover, it was shown that other proposed definitions for such energy relations are not physically meaningful [5]. Still in Chapter III, it was shown that the zero-index index material may be instrumental in achieving a broadband DNG regime. It was demonstrated that the DNG response is fairly robust to effect of loss and disorder, and that the DNG bandwidth of the metamaterial is indeed some orders of magnitude higher than that of its complementary configuration (Sec. III.3.2). Moreover, it was shown that in case of sufficiently low loss, this configuration may mimic to some extent the Veselago-Pendry's lens, enabling a superlensing effect in the near-field.

In Chapter IV, a general and efficient spatially dispersive finite-difference frequency-domain FDFD-SD based formalism was proposed to accurately calculate the electromagnetic fields in a general scenario involving complex shaped spatially dispersive bodies of the double wire medium. The main objective of this Chapter was to highlight that the constitutive relations in the bulk region cannot be extended in a trivial manner across an interface. It was shown by numerically solving several scattering problems that the most straightforward way of modelling the spatial dispersion [6, 7], which consists on Fourier inverting the bulk constitutive relation $\mathbf{D} = \overline{\overline{\varepsilon}}(\omega, \mathbf{k}) \cdot \mathbf{E}$, is only valid in some very specific scenarios and generally may drastically fail. Furthermore, it was demonstrated that **E** and **D** can be linked based on a quasi-static homogenization formalism that takes into account some internal (microscopic) details of the metamaterial [8]. Such a solution yields physically correct results in scenarios where the aforementioned approach fails.

In Chapter V some exciting applications of the double wire medium configuration were put forward. In the first part of the Chapter (Sec. V.2), using the FDFD-SD (IDF) formalism derived in Chapter IV, it was numerically confirmed that a superlens formed by an ultradense array of crossed metallic wires may restore the subwavelength details of an electric line source [9]. The possibility of concentrating the electromagnetic fields at the tip of a tapered double wire medium waveguide was analyzed (Sec. V.3). Finally, a novel approach to correct the chromatic aberrations inherent to single glass lenses was proposed. This solution is based on the fact that the double wire medium may be characterized by broadband anomalous material dispersion and very low loss in the optical domain [10]. It was theoretically and numerically shown with the FDFD-SD formalism that by coating a standard glass lens with the metamaterial it is possible to cancel out the effects of material dispersion, and design a compensated bi-layer lens with nearly no chromatic aberrations, in the whole visible range. The proposed theory was further supported by full-wave numerical simulations that take into account all the minute details of the nanostructure of the metamaterial [11], and it was demonstrated in a conclusive manner the suppression of the chromatic aberrations.

VI.2. Future Work

To conclude the thesis, some possible extensions for the presented studies are discussed as well as other research directions.

Future work on the suppression of the chromatic aberrations may include the design of a mono-layer lens that consists of a double wire medium biconvex surface embedded in a glass host. The key idea relies on *compensating* the positive dispersion of the glass with the negative dispersion determined by the metal inclusions, so that the resulting metamaterial is nearly dispersionless. Furthermore, one can also explore other degrees of freedom of the material (e.g., tilting the wires)[1] to further reduce the chromatic aberrations. It is envisioned that these solutions may not only be an alternative to the conventional achromatic lenses, but they may also be a better approach for the design of achromatic lenses because in principle a mono-layer lens is easier to fabricate than a doublet formed by two surfaces with symmetric curvature.

The effect of chromatic dispersion affects not only the performance of glass lenses, but also the performance of optical fibers. Chromatic dispersion occurs in optical fibers because the index of refraction of silica, the material used for fiber fabrication, changes with the optical frequency ω. This dispersive effect can add additional noise through phenomena such as intersymbol interference and mode-partition noise, and it is responsible for pulse broadening as well [12]. The solutions used to overcome this limitation consist on controlling the spectral width of the optical source [12]. It is believed that similar to the solution proposed here to suppress the chromatic aberrations of optical lenses, the double wire medium might be used to coat a silica optical fiber and reduce the effects of material dispersion. Since an optical fiber may be regarded as a waveguide, the initial step of the proposed study would consist on considering a double wire medium waveguide in cascade with a silica waveguide. In order to provide an impedance match between the two waveguides and ensure good transmission, a quarter-wave impedance transformer can be used.

It would also be very interesting to develop a full-wave 3D simulator to model the complete electromagnetic response of realistic (homogenized) double wire medium

---

[1] In the double wire medium configuration the wires are tilted $\pm 45^\circ$ with respect to the interfaces.

models. Contrarily to the 2D scenarios of propagation considered in this thesis, discretizing a fully 3D model of the double wire medium increases tremendously the computational resources required, and hence it is very challenging to develop such a 3D simulator.

Another possibility for a future work relies on the fact that for wave polarizations different from the one considered here, the double wire medium has several interesting applications such as focusing of the electromagnetic radiation using a flat metamaterial lens and ultraconfined waveguiding [13, 14]. For these problems, analytic methods based on mode matching can still only be used for very specific geometries of the metamaterial. Hence, it would also be desirable to have a full-wave simulator to investigate the electromagnetic macroscopic behavior of complex geometries of the metamaterial and for different wave polarizations.

References

[1] M. G. Silveirinha, "Metamaterial homogenization approach with application to the characterization of microstructured composites with negative parameters," *Phys. Rev. B* **75**, 115104, 2007.

[2] J. D. Jackson, *Classical Electrodynamics*, Sect. 6.6, Wiley, 1998.

[3] D. R. Smith and S. Schultz, "Determination of effective permittivity and permeability of metamaterials from reflection and transmission coefficients," *Phys. Rev. B* **65**, 195104, 2002.

[4] M. G. Silveirinha, "Poynting vector, heating rate, and stored energy in structured materials: A first-principles derivation," *Phys. Rev. B* **80**, 235120, 2009.

[5] V. A. Markel, "Correct definition of the Poynting vector in electrically and magnetically polarizable medium reveals that negative refraction is impossible," *Opt. Express*, **16**, 19152 (2008).

[6] Y. Zhao, P. A. Belov, and Y. Hao, "Modelling of wave propagation in wire media using spatially dispersive finite-difference time-domain method: numerical aspects," *IEEE Trans. Antennas and Propag.* **55**, 1506, 2007.

[7] J. M. McMahon, S. K. Gray, and G. C. Schatz, "Nonlocal optical response of metal nanostructures with arbitrary shape," *Phys. Rev. Lett.* **103**, 097403, 2009.

[8] S. I. Maslovski and M. G. Silveirinha, "Nonlocal permittivity from a quasistatic model for a class of wire media" *Phys. Rev. B* **80**, 245101, 2009.

[9] M. G. Silveirinha, C. A. Fernandes, and J. R. Costa, "Superlens made of a metamaterial with extreme effective parameters," *Phys. Rev. B* **78**, 195121, 2008.

[10] M. G. Silveirinha, "Anomalous dispersion of light colors by a metamaterial prism," *Phys. Rev. Lett.* **102**, 193903, 2009.

[11] CST Microwave Studio Suite$^{\mathrm{TM}}$ 2010, (http://www.cst.com).

[12] G. P. Agrawal, *Fiber-Optic Communication Systems*, John Wiley & Sons, Inc., New York, 2002.

[13] T. A. Morgado, J. S. Marcos, S. I. Maslovski,and M. G. Silveirinha, "Negative refraction and partial focusing with a crossed wire mesh: physical insights and experimental verification", *Appl. Phys. Lett.* **101**, 021104, 2012.

[14] M. G. Silveirinha, "Broadband negative refraction with a crossed wire mesh", *Phys. Rev. B (BR)* **79**, 153109, 2009.